SURFACE ANALYSIS OF ELECTRONIC MATERIALS FOR HIGH SPEED DEVICES

September 1984

Masaharu OSHIMA

CONTENTS

Chapter 1 Introduction

1.1 Historical Background

Surface analytical technologies have been developed for about 20 years to investigate surfaces of solids including metals and semiconductors. Among them Secondary Ion Mass Spectrometry (SIMS), Auger Electron Spectroscopy (AES) and X-ray Photoelectron Spectroscopy (XPS) are regarded as the most successful techniques and now widely utilized.

SIMS is a surface analytical technique to utilize the ion beam to sputter and ionize the surface area of solids, and detect secondary ions. This principle was thought out in 1949 by Herzog and Viehboeck (1.1). Mass spectrometry is very sensitive to trace impurities with especially low ionization potential in comparison to electron spectroscopy such as AES and XPS. Although SIMS is not used for chemical-state analysis, it has been widely employed for extreme trace analysis, in-depth analysis with high depth resolution, and surface analysis.

For quantification, the calibration curve method has been still used, while many attempts have been made to theoretically calculate the impurity concentration, among which the analytical procedure based on the Local Thermal Equilibrium (LTE) plasma model is reportedly the most successful method (1.2). However, this procedure had not been applied to semiconductors, in particular Si.

Auger spectra in the derivative form, that is dN/dE, were measured for the first time in 1968 by Harris (1.3), while Auger

effect in which two electron transition process takes place was discovered by Auger (1.4) in 1925. This technique has been widely employed to analyze surface composition of solids and obtain in-depth profiles in combination with sputtering, because Auger electrons come from only 20 to 30 A depth of solid surfaces as shown in Fig. 1.1.

AES itself can be said to be the well-established surface analytical technique. The recent trend of AES is to realize the micro AES with almost 1000 A spacial resolution in order to analyze extremely small region. The other trend is to analyze the chemical state of solid surfaces in the small area in terms of Auger chemical effect which is thought to be a promising technology in conjunction with XPS.

XPS was developed by Siegbahn (1.5) of Uppsala University to analyze gas and solids. This technique can be also utilized for surface analysis, because photoelectron's escape depth is comparable to Auger electrons. XPS can provide us with information about chemical bondings as well as surface composition, so it is employed to assign the chemical state of solid surfaces in terms of chemical shifts of core levels.

In order to realize extremely surface sensitive photoemission spectroscopy, synchrotron radiation (SR), which was regarded as the useless product of high energy physics using synchrotron and storage ring over 10 years ago, has been utilized for that purpose. Stanford Synchrotron Radiation Laboratory(1.6) is one of the most active centers from the viewpoint of SR use for surface physics in the world. Various kinds of solid surfaces

including Si, GaAs and metals have been studied using SR-PES. One of the most successful achievements is "Unified Defect Model" for 3-5 compound semiconductor surface and interface proposed by Spicer (1.7).

The recent trend for SR-PES is to develop high intensity photon beam using wiggler and undulator magnets to facilitate very sensitive analysis with extremely high energy resolution for assignment of new chemical states.

On the other hand, the progress in electronic materials and devices has been very rapid in these ten years. In Si LSI technologies, for example, the metal-oxide semiconductor(MOS) memory LSI can be said to lead the LSI technologies, and the integration scale is tripled every other year(1.8).

In order to realize the scale down theory including device dimensions, impurity doping control etc., fine pattern delineation, clean process technology free from contamination such as Na in gate oxides, impurity profile control technology such as ion implantation with high precision, and then impurity concentration analysis have to be developed.

In particular, reactive sputter etching technique (RSE) has been regarded as one of the most important processes for fine pattern delineation as well as electron beam lithography. However, there are many problems to be solved such as process control, namely monitoring,elucidation of etching mechanism, and surface damages like contamination and defects.

With regard to Na contamination in gate oxides which would

cause the fluctuation of C-V characteristics, SIMS analysis is considered to be the suitable method to analyze the depth profiles of trace amount of Na quantitatively.

As shown in Fig. 1.2 (1.9), the high speed electronic devices go towards lower left part of this figure, namely lower power dissipation and fast speed. Taking into account the physical limitation of Si LSI, GaAs has been given special attention because of its large electron mobility and easiness of using semi-insulating substrates. However, the impurity control is one of the most critical problems in this case, because at present GaAs substrates contain many kinds of impurities including C, O, Si etc.. Furthermore, impurities in GaAs are reportedly easy to be redistributed during annealing after ion implantation. Therefore, high accuracy impurity analysis using SIMS is one of the key technologies for development of high speed GaAs IC's.

Josephson junction devices are regarded as one of future devices because of their extremely small power dissipation and fast swithing speed. However, they need very thin oxide layer of about 50 A with high precision for tunneling barrier layer. Therefore, very surface sensitive analytical tools are necessary for the characterization of the thin films, especially from the viwpoint of chemical-state analysis.

For that purpose, XPS and AES have been employed. Although PbInAu alloy is used for JJ devices , harder materials such as Nb and Nb3X compounds(A-15 structure) will be utilized in near future because of their stability and high Tc(superconducting

transition temperature). In both cases, Josephson junction devices depend on the electronic properties of surfaces and interfaces for proper operation(1.10). Therefore, it is of great importance to elucidate the oxidation mechanism and oxide properties by means of surface analytical techniques.

1.2 Objectives and contents of this thesis

The objectives of this thesis are to study the fundamental problems involved with the surface analytical technologies of LSI materials, namely Si, GaAs and superconducting materials which are or will be utilized for very fast speed computers. Main themes include the development of new surface analytical methods and the application of them to characterization of new electronic devices and materials.

The results of these works are reported in this thesis in the following chapters, as shown in Table 1.1.

Chapter 2 presents plasma diagnostics of reactive sputter etching using mass spectrometry and optical emission spectroscopy. These are regarded as some kind of surface analytical techniques, because they probe the gas-solid reaction.

Chapter 3 describes the characterization of RSE silicon surfaces using SIMS, AES and XPS. Furthermore, the surface contamination was analyzed using an in situ AES system combined with a RSE apparatus in vacuum developed in the course of this study.

Chapter 4 reports the crystallographic analysis of surface damages caused by RSE. Transmission Electron Microscope (TEM) was used to analyze the defects with newly developed sample preparation methods for cross-sectional TEM observation. Furthermore, this TEM method combined with RSE was applied to the in-depth crystallographic analysis of oxygen-implanted silicon substrates with 1.2×10^{18} cm^{-2} for embedded SiO2 formation.

In chapter 5, is described quantitative analysis of

impurities in semiconductors with SIMS. Computer calculation technique for SIMS quantification was developed on the basis of the LTE plasma model, and applied to the characterization of impurities in GaAs, and Na in Si and SiO2 which is critical contamination for MOS devices.

Chapter 6 reports the characterization of thermal conversion layers in GaAs using a SIMS apparatus with high depth resolution.

Chapter 7 presents photoelectron spectroscopic results of a clean and oxidized Nb-Al alloy using synchrotron radiation. In addition, Auger electron spectroscopy was employed to analyze the oxidized surface in terms of Auger chemical effects. Chemical shifts in Auger spectra were explained by two electron transition process using core level shifts measured by XPS.

The concluding chapter contains a summary of the results and recommendations for future works.

References for chapter 1

1.1) R. F. K. Herzog and F. P. Viehboeck, Phys. Rev. 76(1949) 855.

1.2) C. A. Andersen and J. R. Hinthorne, Anal. Chem. 45(1973) 1421.

1.3) L. A. Harris, J. Appl. Phys. 39(1968) 1419.

1.4) M. P. Auger, J. Phys. Radium. 6 (1925) 205.

1.5) K. Siegbahn, C. Nordling, A. Fahlmen, B. Nordberg, K. Hamrin, J. Hedman, G. Johansson, T. Bergmark, S. Karlsson, I. Lindgrem, B. Lindberg, "ESCA Atomic, Molecular and Solid State Structure Studied by Means of Electron Spectroscopy", (Almgvist and Wiksells, Boktryckeri, A. B. Stockholm, Sweden 1967), Nov. Acta. R. Soc. Sci. Uppsala., Ser. 4, 20 (1967).

1.6) H. Winick and S. Doniach, "Synchrotron Radiation Research" Plenum Press, New York 1980.

1.7) W. E. Spicer, I. Lindau, P. Skeath, and C. Y. Su, J. Vac. Sci. and Technol. 17(1980) 1019.

1.8) G. R. Madland, Solid State Technol. 20 (1977) 91.

1.9) R. M. Asbeck, D. L. Miller, R. A. Milano, J. S. Harris, Jr., G. R. Kaelin and R. Zucca, Int. Electron Devices Meeting, 1981 Washington, D.C.,p. 629.

1.10) J. M. Baker, R. W. Johnson, and R. A. Pollak, J. Vac. Sci. and Technol. 16 (1979) 1534.

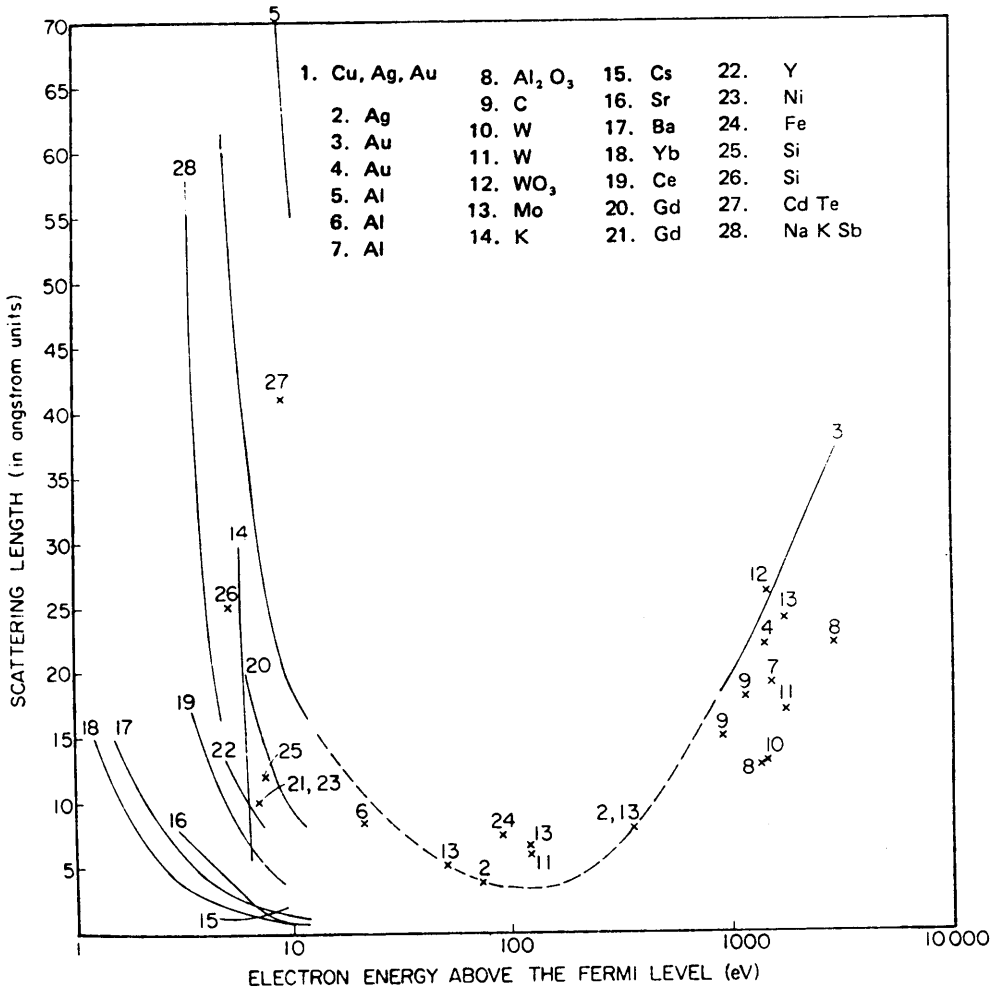

Fig. 1.1 Escape depth of electrons from solids as a function of their kinetic energy(1.6).

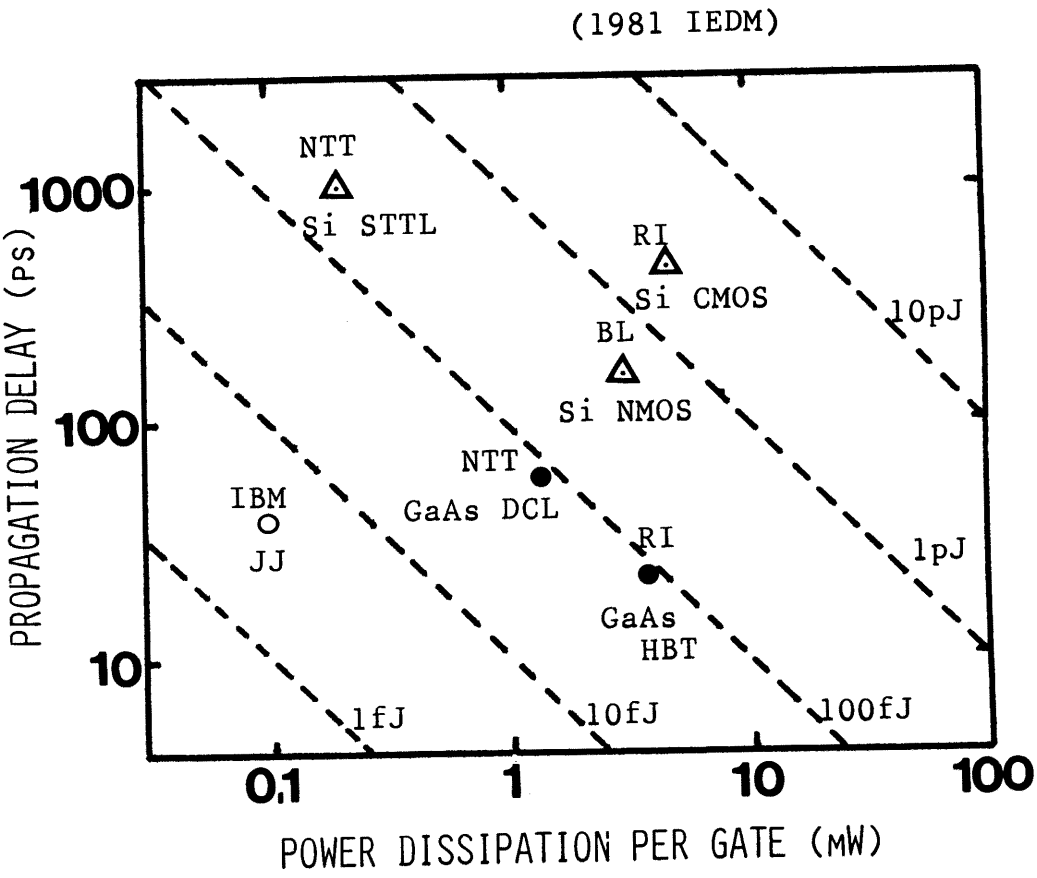

Fig. 1.2 Propagation delay and power dissipation per gate of high speed electronic devices, in particular Si LSI, GaAs IC and Josephson junction devices.

Table 1.1 Outline of this thesis.

Category	Subjects	Needs for Analysis	Methods	Chapter
LSI	Contamination and damage of RSE silicon	Plasma diagnostics	Mass spectrometry Emission Spectroscopy	2
		Surface analysis	AES, XPS	3
		Crystallographic analysis	TEM	4
	Na in SiO_2 gate oxides	Quantitative analysis	SIMS	5
GaAs	Impurity in substrates	Quantitative analysis	SIMS	5
	Thermal conversion	In-depth analysis	SIMS	6
Super-conductors	Initial oxidation for tunnel oxides	Chemical-state analysis	XPS, AES	7

Chapter 2 Plasma Diagnostics of Reactive Sputter Etching using Mass Spectrometer and Emission Spectroscopy *

2.1 Introduction

Recently, dry etching processes have been developed to satisfy the need for fine pattern delineation in LSI fabrication. Dry etching can be classified into three categories; ion etching including RF sputter etching (2.1), plasma etching (2.2) and reactive sputter etching (2.3). These techniques are dry and clean, and offer process simplification compared with conventional chemical etching.

Plasma etching is a process in which the materials of the films and substrates are removed as volatile compounds such as SiF4 produced by chemical reaction with F radical species generated from an RF glow discharge of gases such as CF4. Since this technique is essentially a dry-chemical-etching technique, undercut phenomena are inevitable. Furthermore, it has a drawback that it is unable to etch SiO2 and Al films selectively. On the other hand, reactive sputter etching, proposed by Hosokawa(2.4) and Bonder(2.5) is an effective technique for etching these films selectively with less undercut than conventional plasma etching.

Many studies of the etching mechanism in RSE as well as plasma etching have been reported. The analytical methods available to the elucidation of the etching mechanism can be classified mainly into three groups; (1) the etching characteristics, such as etching selectivity and pattern

*Most of this part has been reported in ref. (A.1) and (A.2).

delineation characteristics, (2) the surface chemistry such as surface contaminations(2.6) and defects which might affect the device characteristics, and (3) the plasma diagnostics such as mass spectra(2.7) , optical spectra (visible(2.8), infrared etc.) and probe methods. Among these methods, the optical spectra are useful because they reflect the plasma directly without disturbing it. Furthermore, this method is superior to the mass spectrometric technique from the viewpoint of cost and availability (or applicability). On the other hand, it is difficult with this method to obtain information about ionic species such as CFx ions, where the mass spectrometric technique is advantageous.

In this chapter, a mass spectrometer has been employed to investigate the plasma in RSE and elucidate the selective etching mechanism of SiO2 on Si substrates. An optical emission spectrometer was used with a focusing lens system, and atomic and molecular spectral line intensities of reaction active species and products were discussed relative to etching rates. Furthermore, the plasma gas temperature which is an important parameter in plasma reaction(2.9) was also investigated relative to the etching characteristics. Based on these results, the applicability of mass spectra and optical spectra to end point detection in etching SiO2 and Si3N4 films on Si substrates was examined.

2.2 Experimental procedures

Experiments were carried out using a diode RF sputter etching apparatus (electrode diameter;100 mm) with a quadrupole mass filter as shown in Fig.2.1. The RF of this apparatus was fixed at 13.56 MHz. To obtain preferential SiO2 etching, a teflon or carbon plate was used as the target,and CF4 gas mixed with C2H4, or C2F6 gas, was used as the etching gas, as proposed by Matsuo(2.3). SiO2 film samples of 5000 to 6000 A thickness were grown thermally on single crystalline Si (100) substrates with wet O2. The etching characteristics of SiO2 and Si is shown in ig.2.2, where C2F6 gas was used with the carbon target. Thus the etching selectivity of about 5 was obtained.

Mass analysis was performed as follows. After sample (SiO2 or Si) had been placed on a target, the apparatus was evacuated to below 5×10^{-6} Torr and the etching gas was introduced through a mass flow meter at a certain flowrate (below 10cc/min). The pressure in the etching chamber was set, for example, at 4×10^{-2} Torr by controling the main valve, and then the pressure in the mass analyzer which had been evacuated below 1×10^{-7} Torr beforehand was set, for example, at 8×10^{-7} Torr by adjusting a variable leak valve. Since the pressure in the etching chamber increased slightly at the beginning of glow discharge, the adjustment of the main valve was needed in order to keep the etching conditions constant.

After reactive sputter etching, samples were analyzed by XPS in order to evaluate the etched surfaces and check whether the SiO2-Si interface was detected correctly.

A spectrometric system consisting of a collimating system(F/5.2 quartz lens and mirrors), a 60 cm grating spectrometer and Optical Multichannel Analyzer have been used with a personal computer to investigate the plasma emission. A schematic diagram of this system is shown in Fig. 2.3. In this study, two types of gratings were employed , one(1200 lines/mm) for the measurement of overall emission spectra and the other (2400lines/mm) for determination of gas temperature. The computer was used for simulation of the CO molecular spectral synthesis.

2.3 Results and discussion

(1) Mass spectra analysis

Mass spectra were observed under four conditions. In case No. 1, the variable leak valve was closed. This case corresponds to residual gas analysis (pressure; 1×10^{-7} Torr). In case No.2, $CF_4+C_2H_4$ etching gas was introduced into the mass analyzing chamber (pressure; 7×10^{-7} Torr). When RF power was applied to the lower electrode without an Si sample, the spectrum of case No.3 was obtained. Then, the pressure in the mass analyzing chamber was kept constant (7×10^{-7} Torr) by adjusting the variable leak valve. The difference between cases No.2 and No. 3 indicates the discharge effect of the etching gas. In case No. 4, an Si wafer of diameter 1.25 inches was etched using a teflon target. The results are summarized in Table 2.1. In case No. 2, an increase in C, CO, O_2 and C-F was observed . In case No. 3, the peak heights of CF, CF_2, CF_3 and CmFn increased by etching or sputtering the teflon target. The decrease in the peak heights of H_2O and O_2 and the increase in those of CO and CO_2 was caused by reaction between $CF_4+C_2H_4$ and the background residual gas in the etching chamber. In etching the Si wafer, the peak heights of Si-F compounds increased, and the amount of $^{85}SiF_3^+$ became about 3 times as large as that without the Si wafer (No. 3), as shown in No.4. Thus the $^{85}SiF_3^+$ spectrum proved to be useful for monitoring the etching process of Si and Si compounds.

In reactive sputter etching, the target plays an important role in the selective etching of SiO_2. Table 2.2 shows the mass spectral intensities in etching single crystalline Si and SiO_2

substrates using CF4 gas with an A1203 and a teflon target. The etching rates of Si and Si02 with the A1203 target differed considerably from those with the teflon target, a large amount of CmFn gas being generated by the latter. Since the intensities of both peaks M/e=47 and 66 were mostly independent of the etching rates of Si and Si02, these peaks are presumably due to COF^+ and COF2. On the other hand, the contribution of unstable $COF3^+$ to the M/e=85 peak was found to be small compared with $SiF3^+$.

It should be noted that these analyses do not reflect the plasma reaction exactly, because the reaction products can change to other molecules by decomposition and recombination in the path from the etching chamber to the detector and, furthermore, the molecules are decomposed into some fragments by electron bombardment in the ionization space within the mass analyzer. However, from the results in Tables 2.1 and 2.2, CmFn gases generated from teflon are thought to enhance the etching of Si02.

(2) Emission spectra in etching Si3N4

Emission spectra in etching Si3N4 were measured with the 1200 lines/mm grating from a point immediately above the sample. The spectra consist of molecular spectra (CO, N2 and CO_2^+) and atomic spectra (F, H and Si), as shown in Fig. 2.4. There are, however, some unassigned lines which are probably due to the C-F molecular system. The Si line could be detected only near the sample surface, namely in the ion sheath region. The intensity profiles of these lines in the RF plasma were measured to investigate the reaction in RSE. Figure 2.5 shows the intensity profiles above the sample in etching Si3N4 at a C2F6 pressure of 0.04 Torr and an applied power of 60W. It should be noted that F and Si lines are strong near the sample surface and decrease away from the surface, while CN and N2 ejected from the sample have maximum intensity at a point about 20 mm away from the sample on the lower electrode.

This result indicates two possibilities:one is that Si3N4 is etched in the form of atomic Si by the physical sputtering effect, and the other is that it is etched in the form of SiF4 by chemical sputtering and decomposed into Si and F in the ion sheath region where several hundred volts (self-bias potential) are applied. From the former case, the exponential profile of the Si line intensity would be attributable to a diffusion profile of ejected Si atoms. On the contrary, from the latter model, the intensity profile is considered to be due to the profile of self-bias potential by which SiF4 is decomposed. Taking into account that reaction products such as CN and N2 molecules are

dissolved in the ion sheath region by the high self-bias potential, the Si line is thought to be due to the Si atoms decomposed from the ejected reaction products, that is, SiF_4. Furthermore the validity of the latter model can be also confirmed from the result that only weak Si lines were detected when Ar gas instead of C_2F_6 gas was fed into the chamber and discharged.

Next, the dependence of these line intensities on the RF power applied to the lower electrode was investigated. As shown in Fig. 2.6, there are two types of dependence. While CO and H which are independent on the etching reaction are almost proportional to the power, CN, N2, Si and F lines which presumably reflect the reaction products are proportional to $(\text{power})^n$, with n from 1.3 to 1.7. Taking into account the fact that the etching rate of Si_3N_4 has the dependence of $(\text{power})^{0.7}$, the emission line intensity proves to be proportional to the product of the ejected particle density and the excitation probability. Since CO and H intensities are thought to be proportional to the excitation probability by the RF plasma, Si, F, CN and N2 are confirmed to reflect real reaction products. Furthermore, in the discharge of SiF_4 gas, the Si line intensity was proportional to the applied power, indicating that the excitation probability has the dependence of $(\text{power})^1$.

As will be described in section 2.5, the Si_3N_4/Si interface was not detected positively by means of F emission line in RSE, while Harshbarger et al(2.8) reported the effectiveness of F line as an etching monitor of Si_3N_4 films in the plasma etching. This

is probably because the F radicals in RSE do not play such an important role in etching Si3N4 as in plasma etching.

The effect of mixing O2 in C2F6 was investigated in order to determine the reaction products and active species. Figure 2.7 shows the dependence of emission line intensities and etching rate of Si3N4 on the O2 percent in a C2F6+O2 mixture at the pressure of 0.04 torr and the applied power of 60 W. In this case, the spectrometer was focused immediately above the sample surface. Among these lines, CN line shows the same tendency as the etching rate which shows a maximum value in the case of 20 % O2. Therefore, CN is considered to be the reaction product. The fact that N2 and CO_2^+ lines show an analogous tendency of intensity increase with O2 admission implies that these two species are produced by the following reactions:

$$\begin{aligned} &mSi_3N_4 + nCF_x \longrightarrow m'SiF_4 + n'CN \\ &CN + O_2 \longrightarrow CO_2 + 1/2\ N_2. \end{aligned} \qquad (2.1)$$

Thus N2 is produced by the oxidation of CN which is ejected from Si3N4 in RSE, while N2 in plasma etching is directly produced by the following reaction:

$$Si_3N_4 + 12\ F \longrightarrow 3\ SiF_4 + 2\ N_2 \qquad (2.2)$$

Therefore, the active species in RSE proved to be CFx, not F radicals, which are reportedly the active species in plasma etching(2.10). The implication that N2 in RSE is converted from CN by oxidation is confirmed by transient measurements. It is found that emission line intensities can be given by the following function of the elapsed time after the start of discharge,

$$I = Io\{1-\exp(-t/\tau)\}, \qquad (2.3)$$

where Io is the intensity at the steady state and τ is the relaxation time. For CN, F, Si, H and CO, τ was about 4 seconds under the RSE condition of 60 W and 0.04 torr C2F6. On the other hand, τ for N2 was about 12 seconds. This long relaxation time implies that N2 is not directly produced by the etching.

The dependence of Si, F and N2 line intensities on C2F6 pressure was also investigated. As shown in Fig. 2.8, the maximum point of N2 intensity gets nearer to the sample surface with increasing C2F6 pressure, indicating that the plasma in the low C2F6 pressure has a wide ion sheath region. While N2 line intensity increases with C2F6 pressure, the etching rate of Si3N4 shows a maximum point at 0.1 torr. The intensity of Si line, which could be observed only in the ion sheath region, corresponds to the etching rate. The discrepancy between the N2 and Si line intensities can be explained as follows: while N2 is produced only by the oxidation of CN at lower pressures, at higher pressures the etching proceeds not only by CFx ions (RSE mechanism), but also by F radicals (plasma etching mechanism). Thus N2 intensity increases with pressure. The increase of F line intensity at the negative glow with increasing pressure verifies this explanation.

(3) Emission spectra in etching Si and SiO2

The intensity profiles of the emission spectra above the sample surface in etching Si and SiO2 are shown in Figs. 2.9 and 2.10. The ratio of Si line intensity in etching a SiO2 plate (78 cm^2) to that in etching a Si wafer (60 cm^2) was about 2.9 at the point just above the sample. Since the ratio of the SiO2 etching rate to that of Si was about 5 under this condition, the ratio of the number of Si atoms ejected from the two samples was 2.2. The good proportionality between Si emission line intensity and the ejected Si atoms indicates that both Si and SiO2 are etched not by sputtering but in the from SiF4 or SiFx, because the emission efficiency of Si atoms physically sputtered from Si substrates with Ar gas was smaller by about two orders of magnitude than that from SiO2. This small emission efficiency from Si was explained by the non-radiative process competing with the radiative de-excitation(2.11). Therefore, the Si emission lines in RSE can be attributed to the excitation of Si atoms decomposed from SiF4, which is the reaction product in both cases, Si and SiO2. Since the Si emission line ($4s\ ^1P_1 \longrightarrow 3P_0\ ^1D_2$) has the same proportionality to the etching rate as the SiF_3^+ mass spectral line, it has a possibility for the etching monitor.

The strong CO_2^+ line at the cathode fall in etching SiO2 compared to Si is thought to reflect the direct reaction product CO2 from the SiO2 sample. The C line observed especially in etching the Si substrate is presumably due to carbon atoms sputtered from the surface carbon layer(see Chap. 3) deposited on the Si substrate as well as to those decomposed from the C2F6

gas. On the contrary, the comparatively small C line intensity in etching Si_3N_4 and SiO_2 is explained by the volatile reaction products such as CN and CO_2.

The emission spectra in discharging the SiF_4 gas were also measured in order to confirm the formation of SiF_4 in etching Si compounds. Figure 2.11 shows the spectral line intensity profile, where a strong Si emission line could be observed, especially in the ion sheath region. In this case, the number of SiF_4 molecules introduced into the etching chamber was 1.3×10^{20} molecules/min., while the number of SiF_x molecules ejected from the Si sample (60 cm^2) was about 4×10^{18} molecules/min., where the etching rate of Si was 120 A/min. Therefore the experimental ratio of the Si line intensity (about 66) is comparable to the predicted ratio of SiF_4 molecule density (about 33), which indicates that SiF_4 is the reaction product in RSE.

2.4 Determination of plasma gas temperature

Optical emission spectra were also used for determination of plasma gas temperatures by means of rotational analysis of molecular spectra. The molecular spectrum used was (0,3) band (bandhead: 5610 A) in CO angstrom system(2.12). The simulation technique by a least square procedure following the work of Slovetskii(2.13) was adopted here, because the spectrometric resolution (about 0.1 A) is not high enough to recognize the J number from the emission spectra.

The intensity of the (J',J") transition is given by

$$I_{J'J"} \propto q_{v'v"} S(J')\exp(-B_{v'}(J'+1)J'/kT), \qquad (2.4)$$

where $q_{v'v"}$ is the Franck-Condon factor, S(J') is the Honl-London factor and $B_{v'}$ is the rotational constant. Taking into account the broadening of rotational lines(2.14), the CO (0,3) band spectrum was synthesized with the computer. Figure 2.12 shows the observed CO spectrum (a) and the calculated spectrum assuming the temperature to be 450 K (b). From the dependence of determined temperatures on etching condition (C2F6 pressure and power), it is concluded that T is proportional to the applied power and that reactive sputter etching has lower temperature than that in conventional plasma etching, as shown in Fig. 2.13. Gas rotational temperature was also investigated by R.A.Porter in an RF glow discharge of N2 at a pressure of 1.0 Torr and an RF power of 100W. The gas temperatures obtained in this work are comparable to the reported values in the N2 plasma.

The influence of gas (O2 and C2H4) mixing into C2F6 on Tg was also investigated in order to compare with the results in

Fig.2.7. As shown in Fig. 2.14, Tg increases by mixing C2H4 (a reductive gas) and decreases by mixing O2 (an oxidative gas). This is probably because the discharge of C2F6 gas in which a small amount of O2 or H2O was mixed produces some COF2 or COF molecules which decrease the gas temperature. A small amount of COF2 (or COF) is thought to be reduced to C-F system by mixing C2H4 and to generate the formation energy of COFx, while C2F6 is oxidized into COF2 by mixing O2 and the energy is absorbed. As shown in Fig. 2.7, the CO intensity has the maximum point at about 20 % O2, which corresponds to the minimum point of Tg at 10 to 20 % O2 in Fi. 2.14. The deccrease in Tg in the mixture of C2F6 with He is analogous to the result reported by Duffendack(2.15).

2.5 Application to process monitoring

(1) Mass spectra for process monitor

Figure 2.15 shows mass spectral line intensity-time curves using O^{16+} and SiF_3^{85+} as the etching monitor for the reacitive sputter etching of SiO2/Si system. In the O^{16+} mass specrum, only a slight change was observed at the SiO2-Si interface, while in the SiF_3^{85+} mass spectrum, a large change could be observed. For O^{16+}, the background level is so high, as shown in Tables 2.1 and 2.2, that the amounts of O^+ and CO^+ produced in the following reactions proved to be quite small compared with those of the background in the etching gas.

$$SiO2+CF4 \rightarrow SiF4+CO2,$$
$$CO2 \rightarrow CO+O. \qquad (2.5)$$

This result was confirmed by emission spectra, (Fig.2.10) which showed that the main spectra were due to CO molecular lines and H atomic lines. Therefore, in these cases, the mass spectra should be used which involve only a small percent of the background composed of H, C and O, and their compounds.

Intensity-time curves in the etching process of SiO2-Si system were obtained using various mass spectral lines. The results are summarized in Table 2.3 in the form of "decrement ratio" defined as (A-B)/Ax100%. Here, A indicates the mass signal intensity just before the intensity change at the SiO2-Si interface, and B indicates the intensity just after the SiO2 film is completely removed. Method 1 corresponds to the monitoring of the etching process by the mass spectra of species containing O. The sample was an SiO2 film of 5.5 cm^2 on Si and the power

applied was 100 W. In this case, the decrement ratio was only a few percent. Method 2 corresponds to the case monitored by the mass spectra of species containing Si. From the result in Table 2.3, it is concluded that the mass spectral lines of Si-F compounds can be used to monitor the etching process in the SiO2-Si system.

Since the CF_3^+ peak was the strongest in the mass spectrum of CF4 gas under "mass analysis conditions 2 and 3" in Table 2.1, $^{85}SiF_3^+$ is considered to be mainly due to the reaction products SiF4. Thus, its intensity is expected to be proportional to the number of Si atoms ejected from SiO2 or Si. This implies the possibility of monitoring the etching process in the SiO2-Si system using the $^{85}SiF_3^+$ signal.

When SiO2 and Si are etched at the same etching rate, the number of Si atoms sputtered from SiO2 and Si per unit volume are ρ_{SiO2} $x N_A/(28+16x2)$ and ρ_{Si} $x N_A/28$, respectively, where ρ is the density, N_A is Avogadro's number and 28 and 16 are the atomic weights of Si and O, respectively. When the etching rate of SiO2 is R times as large as that of Si, the ratio of the number of Si atoms sputtered from SiO2 to that from Si is R/2.27, where 2.27 is equal to $(\rho_{Si}/28)/(\rho_{SiO2}/60)$.

Figure 2.16 shows the dependence of the $^{85}Si_3^+$ intensity on the sample area (x) in etching SiO2 films. The intensity (A) in etching SiO2 and that (B) in etching Si, respectively, are found to be proportional to the sample area having the same background intensity (C). Their proportionality coefficients are denoted k and k' respectively. From the relationship in Fig. 2.16, the

decrement ratio y is given by

$$y=(k-k')x/(kx+C) \qquad (2.6)$$

Furthermore, from the proportionality of k and k' to the number of Si atoms sputtered from SiO2 and Si, R/2.27 is equal to k/k'. Then, eq.(2.6) is substituted as follows:

$$y=(1-2.27/R)\frac{1}{1+C/kx} \qquad (2.7)$$

This equation means that, when R is larger than 2.27, the signal decreases abruptly at the interface.

Figure 2.17 shows the dependence of the decrement ratio (y) on the sample area (x) exposed to the etching gas. The solid lines show the values calculated from eq.(2.7) using optimum values as C/k. Thus, it is concluded that the $^{85}SiF_3^+$ intensity can be expressed quantitatively by R, x and the M/e=85 background.

(2) Comparison of mass spectra with emission spectra

The comparison was made for mass spectra and emission spectra in terms of signal stability. The end point, namely the SiO2-Si interface, was not positively detected by means of CO and F emission spectral lines. However, using a collimating system consisting of two quartz lenses (F/5.2), the Si atomic line could be detected only near the sample surface, that is, the ion sheath region. Thus, end-point monitoring using the Si emission line(2882 A) was attempted.

Figures 2.18 and 2.19 show the signal intensity-time curves in etching SiO2 filme on Si substrates. Although an emission spectrometer is less expensive than a mass spectrometer which needs the differential pumping, the S/N ratio of the emission line for the etching monitor turned out to be inferior to the mass spectral line.

Next, Si3N4 films on Si substrates were examined for etching monitoring. In etching Si3N4, CN and N2 lines were expected to be available spectra for end point detection because these line intensities varied with the etching rate of Si3N4 films as shown in Fig. 2.7. Figure 2.20 shows F and CN intensity-time curves in etching 19.6 cm^2 area Si3N4 sample at 60 W applied power, where the etching rate was 1100 A/min. In this monitoring, the measurement point was 20 mm above the sample where N2 and CN lines had their maximum points in intensity. An etching monitor using N2 line was also examined, and the signal decrement ratio at the Si3N4-Si interface was plotted in Fig. 2.21 compared with that by CN line. Since the analogous decrement ratio was obtained

even by means of mass spectra, that is $^{85}SiF_3^+$, it can be said that both mass and emission spectra are useful in the case of Si3N4/Si system. However, The CN line is found to be most suitable for end-point detection in etching Si3N4 samples of small area down to 2 cm^2.

2.6 Conclusion

A monitoring technique using mass spectrometry and emission spectroscopy in reactive sputter etching has been investigated. The $^{85}SiF_3^+$ mass peak proved to be the most effective indicator for the SiO2/Si system. The decrement ratio for its intensity at the SiO2/Si interface was correlated with the sample area from its proportionality to the etching rates of SiO2 and Si and the sample area.

Optical emission spectra were measured with a collimating system to obtain the concentration profiles of several radical species in the gas plasma. From the dependence of observed line intensities (Si, F, N2, CN, CO, CO_2^+, H and C) on etching condition, it is concluded that SiF4 is the reaction product, and that Si, CN and N2 lines reflect the etching process of Si3N4, while only Si line reflects the etching process of SiO2 and Si. The active species in etching Si3N4 and SiO2 in RSE is considered to be CFx, not F radicals. Using these lines, end point detection was performed successfully in Si3N4/Si system.

In addition, plasma gas temperature was determined by a simulation technique, and the dependence of Tg on etching condition was investigated. The increase in Tg caused by mixing C2H4 and the decrease by mixing O2 were explained by the decomposition and formation of COF2 or COF.

References for Chapter 2

2.1) S. Somekh, J. Vac. Sci. and Technol. 13 (1976) 1003.

2.2) H. Abe, Y. Sonobe and T. Enomoto, Jpn. J. Appl. Phys. 12 (1973) 154.

2.3) S. Matsuo and Y. Takehara, Jpn. J. Appl. Phys. 16(1977) 175.

2.4) N. Hosokawa, R. Matsuzaki and T. Asamaki, Proc. 6th Int. Vacuum Congress, Tokyo, 1974, Jpn. J. Appl. Phys. Suppl.2, Pt.1, (1974) 435.

2.5) J. A. Bondur, J. Vac. Sci. and Technol. 13(1976) 1023.

2.6) J. W. Coburn, H. F. Winters and T. J. Chuang, J. Appl. Phys. 18(1977) 3532.

2.7) B. A. Raby, J. Vac. Sci. and Technol. 15(1978) 205.

2.8) W. R. Harshbarger, R. A. Porter, T. A. Miller, and P. Norton, Appl. Spectrosc. 30(1977) 201.

2.9) R. A. Porter, J. Electrochem. Soc. 126(1979) 460.

2.10) C. J. Mogab, A. C. Adams, and D. L. Flamm, J. Appl. Phys. 49(1978) 3796.

2.11) N. H. Talk, I. S. T. Tsong, and C. W. White, Anal. Chem. 49(1977) 16A.

2.12) R. W. B. Pearse and A. G. Gaydon, "The Identification of Molecular Spectra" (Chapman and Hall, London, 1963).

2.13) D. I. Slovetskii and A. S. Sokolov, Opt. Spectrosc. 36(1974) 265.

2.14) D. M. Phillips, J. Phys. D. appl. phys. 8(1975) 507.

2.15) O. S. Duffendack, R. W. Revans and A. S. Roy, Phys. Rev. 45(1934) 807.

Mass Spectrometer

↓

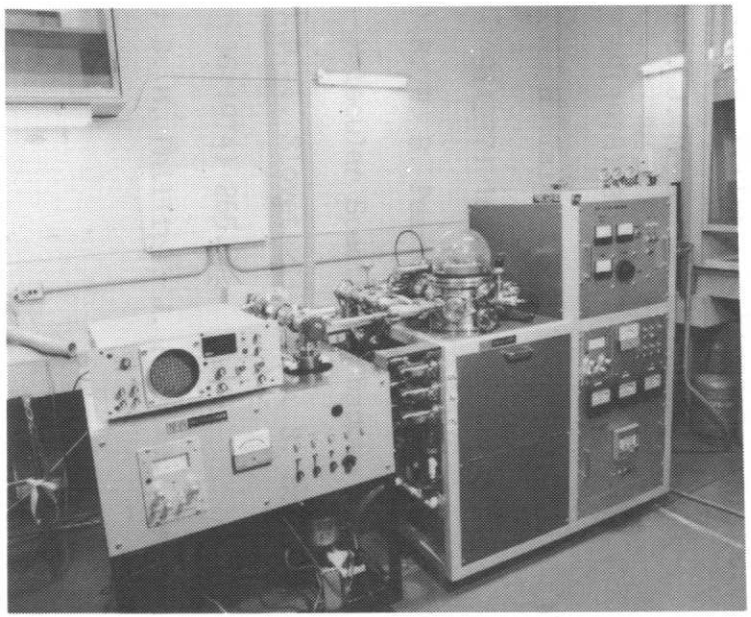

↑

Reactive Sputter Etching Apparatus

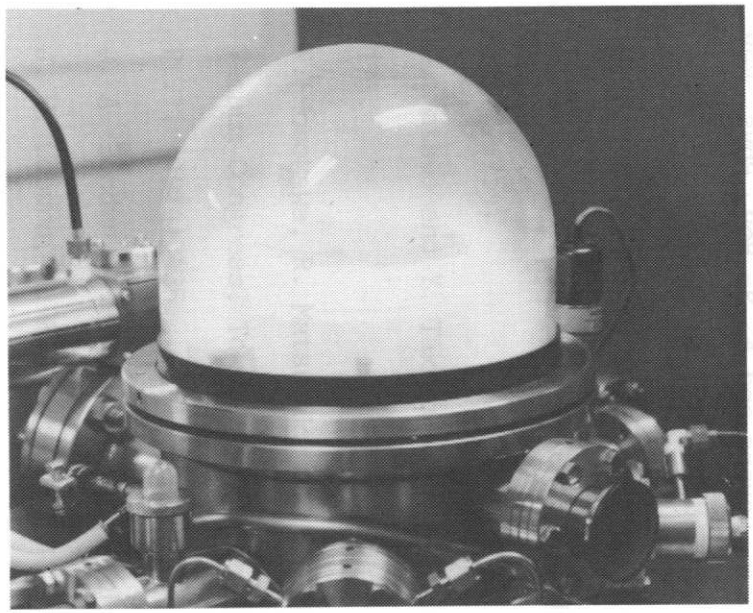

Reactive Chamber during Discharging

(CF_4 4×10^{-2} Torr, 80 W)

Fig.2.1 Reactive sputter etching apparatus with the mass spectrometer.

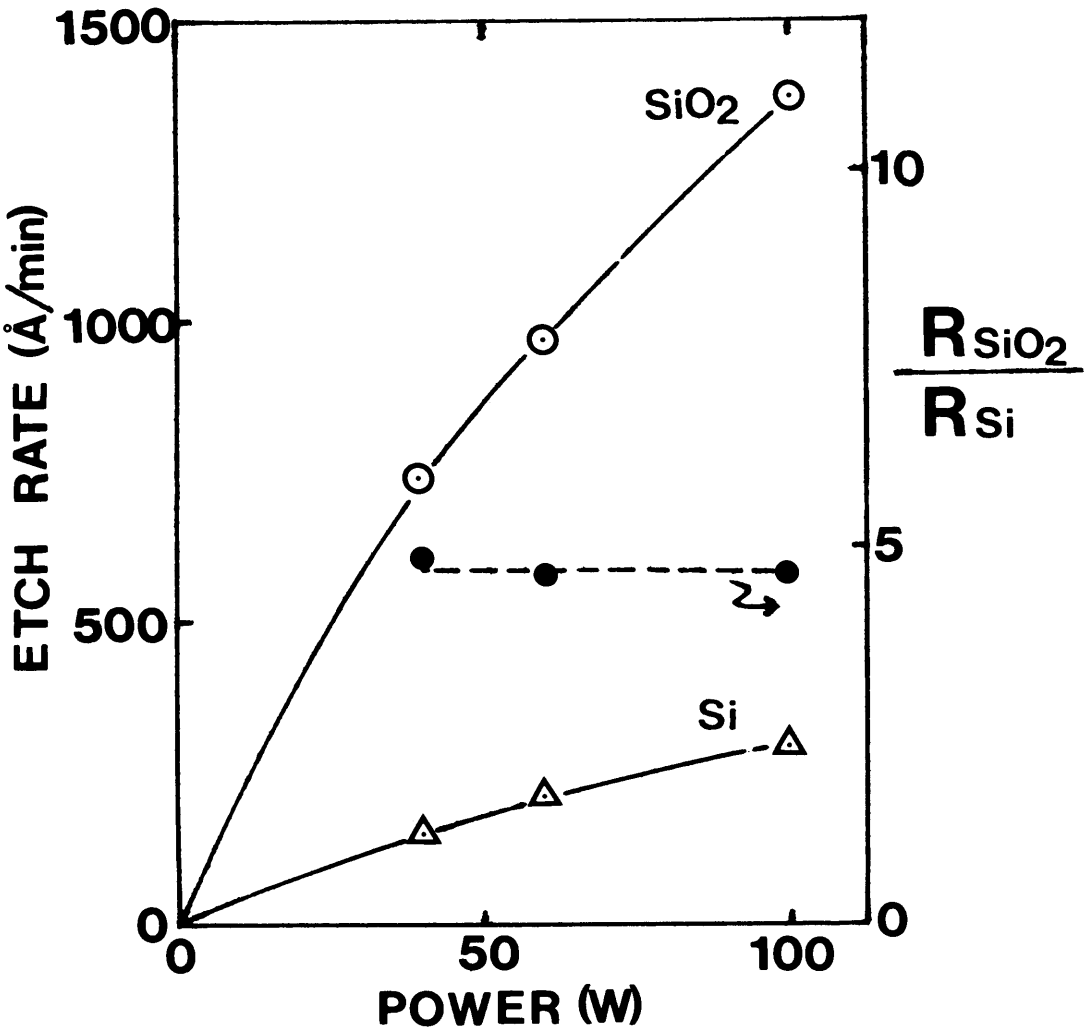

Fig.2.2 Etching rates of SiO2 and Si as a function of applied power.

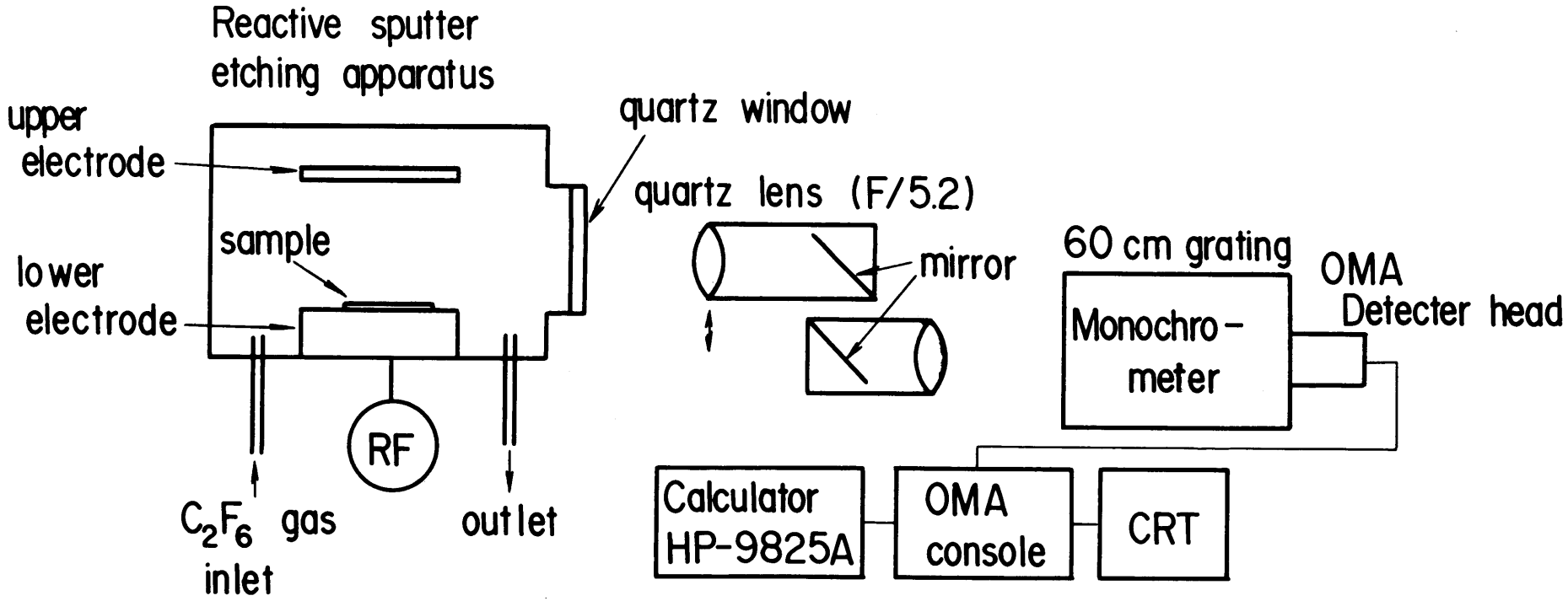

Fig.2.3 Schematic diagram of the experimental apparatus.
Electrode, 10 cm in diameter.

Table 2.1 Mass spectral intensity under four conditions.
$CF_4+C_2H_4$ total pressure; 4×10^{-2} Torr, applied power; 100 W.
1; Residual gas analysis (pressure in the mass filter: 1×10^{-7} Torr).
2; Mass spectra of mixed gas (7×10^{-7} Torr).
3; Mass spectra in etching a teflon target without Si wafer (7×10^{-7} Torr).
4; Mass spectra in etching Si wafer (1.25″ ϕ) over a teflon target (7×10^{-7} Torr).

M/e (mass number)	Mass analysis condition (a. u.)			
	1	2	3	4
1(H)	1.5×10^2	2.1×10^2	2.3×10^2	1.3×10^2
12(C)	3.6	5.5×10	1.5×10^2	1.8×10^2
16(O)	2.8×10	8.0×10	4.9×10	3.8×10
18(H_2O)	1.1×10^3	4.9×10^3	1.8×10^3	1.4×10^3
20(HF, etc.)	1.9×10	1.1×10^2	8.4×10^2	3.8×10^2
28(CO, Si)	1.6×10	7.0×10^2	1.6×10^3	1.0×10^3
29(Si, etc.)	3.2	2.1×10	2.3×10	1.8×10
30(Si, etc.)	0.9	3.4	6.0	4.7
31(CF)	1.1	2.2×10	6.0×10^2	1.1×10^3
32(O_2)	—	1.5×10^2	1.6×10	1.9×10
44(CO_2, SiO)	5.4	2.7×10	6.6×10	4.0×10
47(SiF, COF)	0.1	0.4	7.4×10	5.7×10
50(CF_2)	0.4	2.8×10	2.7×10^2	4.2×10^2
66(SiF_2, COF_2)	—	—	3.2×10	2.1×10
69(CF_3)	0.5	6.7×10	1.8×10^3	2.5×10^3
74(C_3F_2)	—	—	3.2	8.1
81(C_2F_3)	—	0.1	3.5×10	5.5×10
85(SiF_3, COF_3)	—	0.2	3.9	1.4×10
93(C_3F_3)	—	—	6.8	1.4×10
100(C_2F_4)	—	—	1.9	2.9×10
104(SiF_4)	—	—	—	0.2

Table 2.2 Mass spectral intensity in etching Si and SiO_2 substrates with Al_2O_3 target and teflon target. CF_4 pressure; 3×10^{-2} Torr, applied power; 100 W.

M/e (mass number)	Etching condition (a.u.)			
	Al_2O_3 target		Teflon target	
	Si	SiO_2	Si	SiO_2
16(O)	3.0	2.0	2.0	2.5
31(CF)	8.0	8.2	22.0	23.5
32(O_2)	1.6	1.3	1.0	0.8
44(CO_2)	11.6	9.0	9.6	12.4
47(SiF, COF)	6.7	6.0	1.6	2.0
50(CF_2)	10.2	13.7	12.0	13.0
66(SiF_2, COF_2)	4.2	5.1	1.1	1.8
81(C_2F_3)	—	—	4.3	4.0
85(SiF_3, COF_3)	16.0	4.4	3.4	2.6
93(C_3F_3)	—	—	0.8	1.2
100(C_2F_4)	—	—	3.5	4.0
119(C_2F_5)	1.4	2.0	6.5	9.3
Etching rate (A/min)	1590	977	445	1116

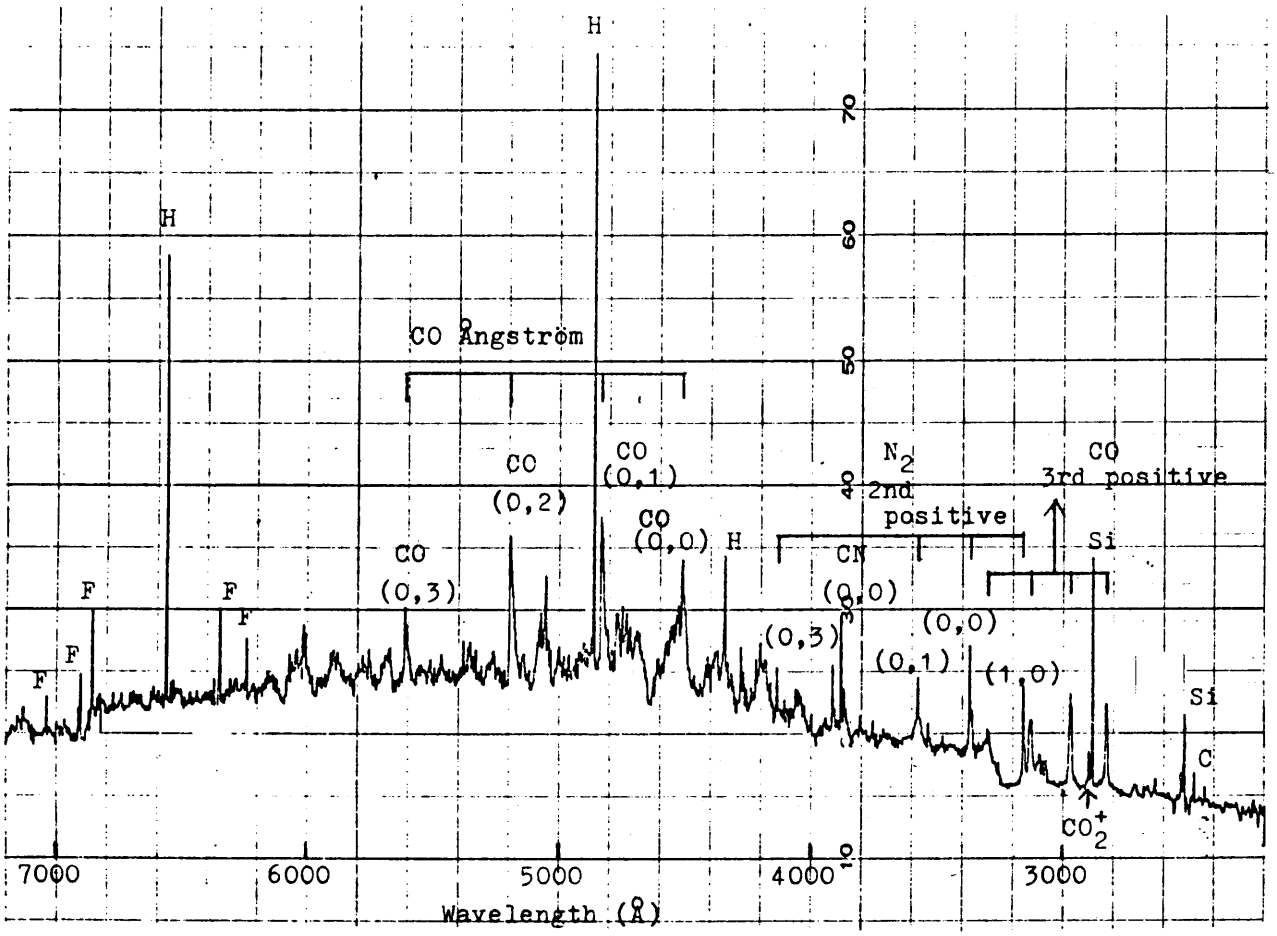

Fig. 2.4 Emission spectra during RSE of Si3N4 at 0.04 Torr C2F6 pressure and 60 W applied power. The spectrometer was focused just above the sample surface.

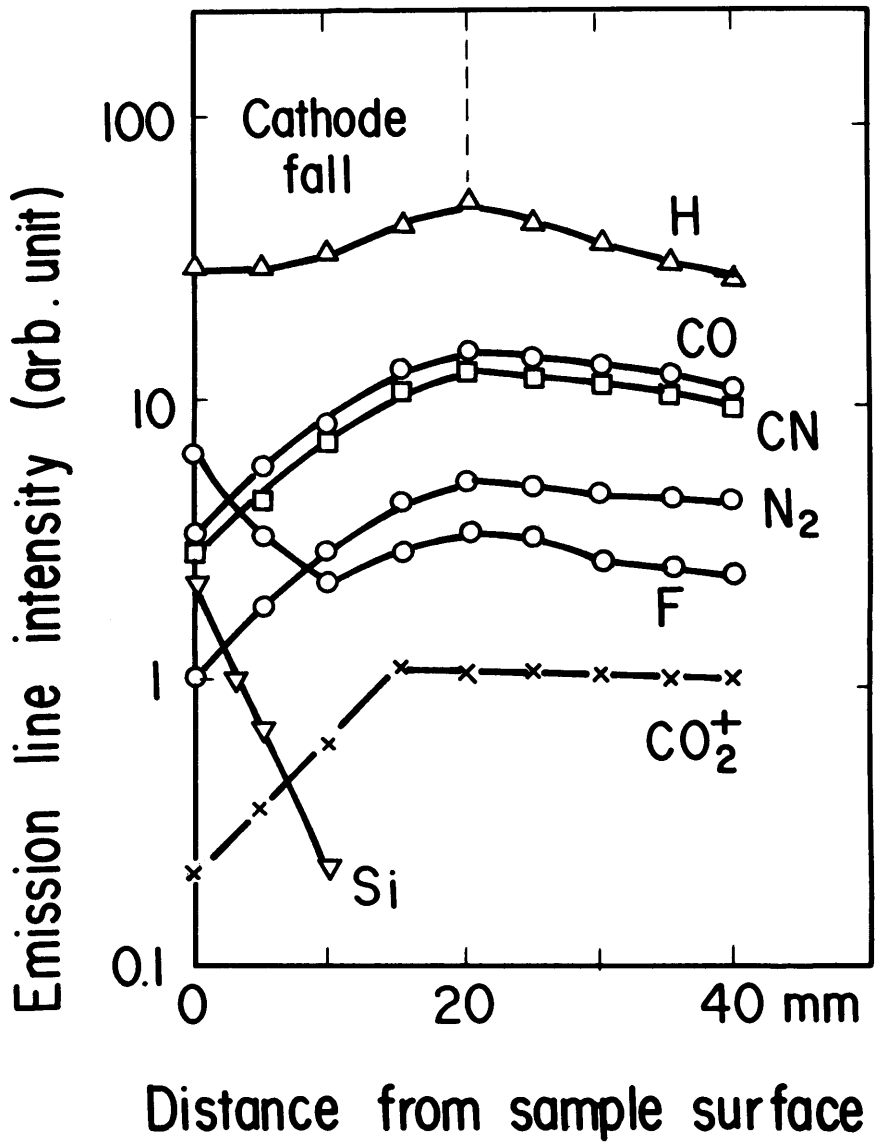

Fig.2.5 Emission line intensities as a function of distance from the sample surface during RSE of Si3N4 at 0.04 Torr C2F6 pressure and 60 W applied power. H(4861 A), Si(2882 A), F(6856 A), CO(4835 A), CN(3883 A), N2(3159 A), CO_2^+ (2896 A).

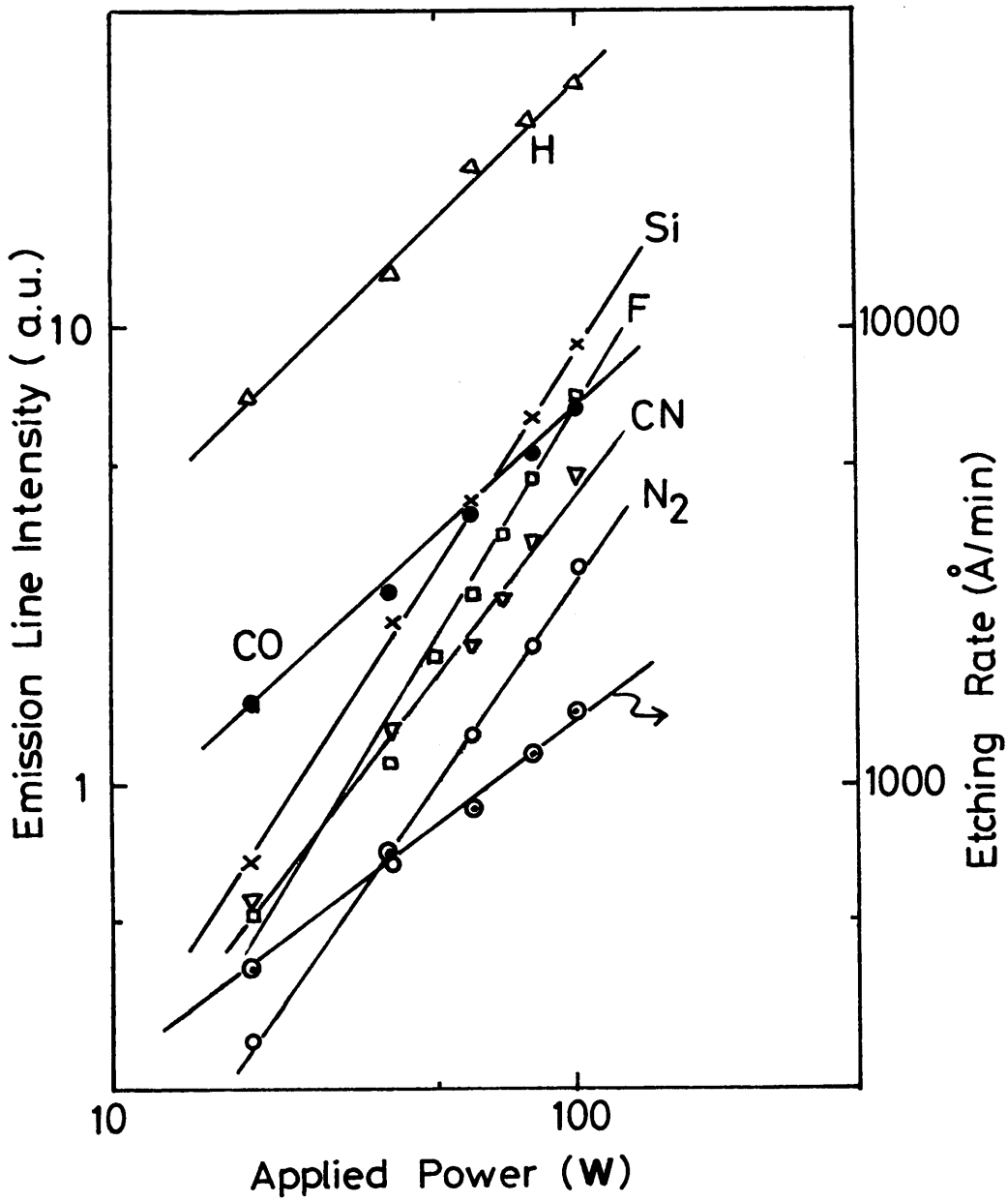

Fig.2.6 Emission line intensities during RSE of Si3N4 at 0.04 Torr C2F6 pressure, and etching rate of Si3N4 as a function of applied power. The spectra were measured just above the sample surface.

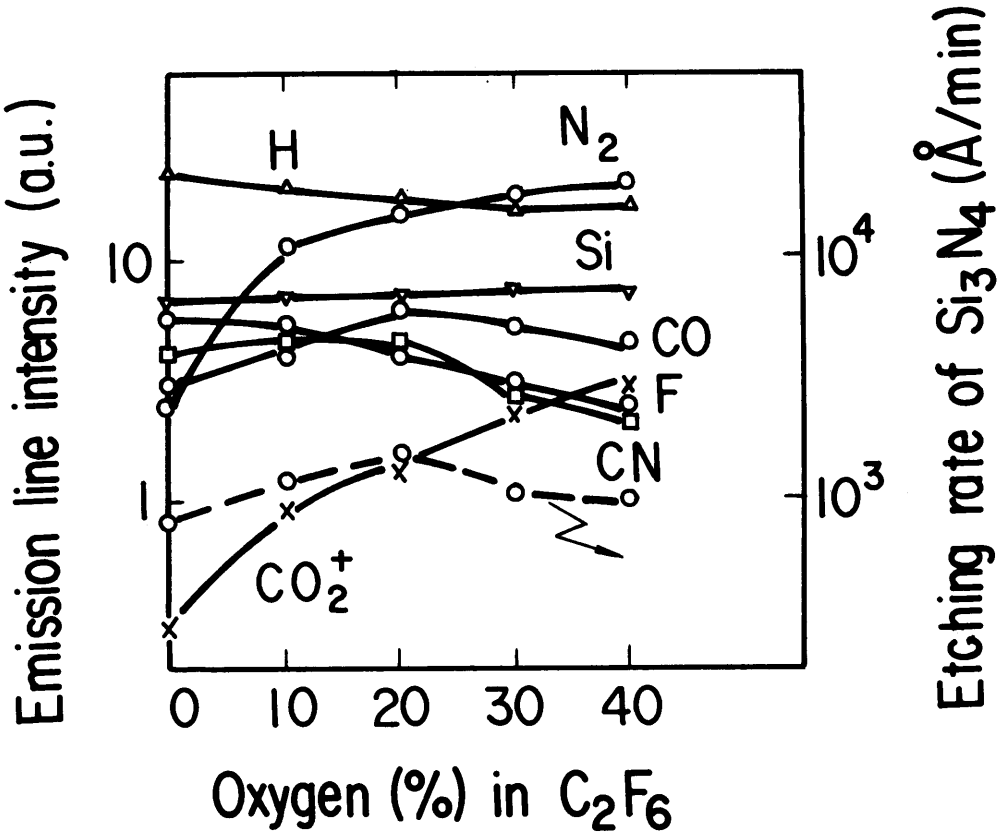

Fig.2.7 Emission line intensities during RSE of Si3N4 at 0.04 Torr total pressure and 60 W applied power, and etching rate of Si3N4 as a function of oxygen percentage in C2F6+02 gas mixture. The spectra were measured just above the sample surface.

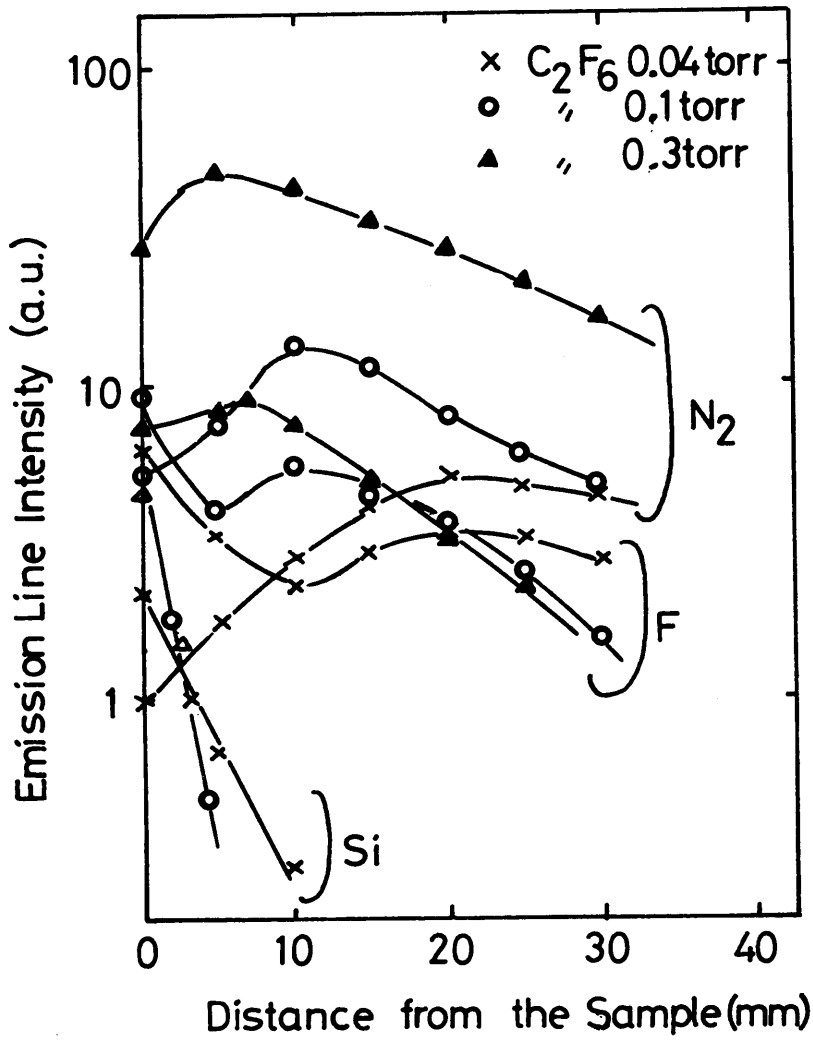

Fig.2.8 Dependence of Si, F and N2 line intensities as a function of distance from the sample surface on C2F6 pressure. Sample; Si3N4 (78 cm^2), power; 60W.

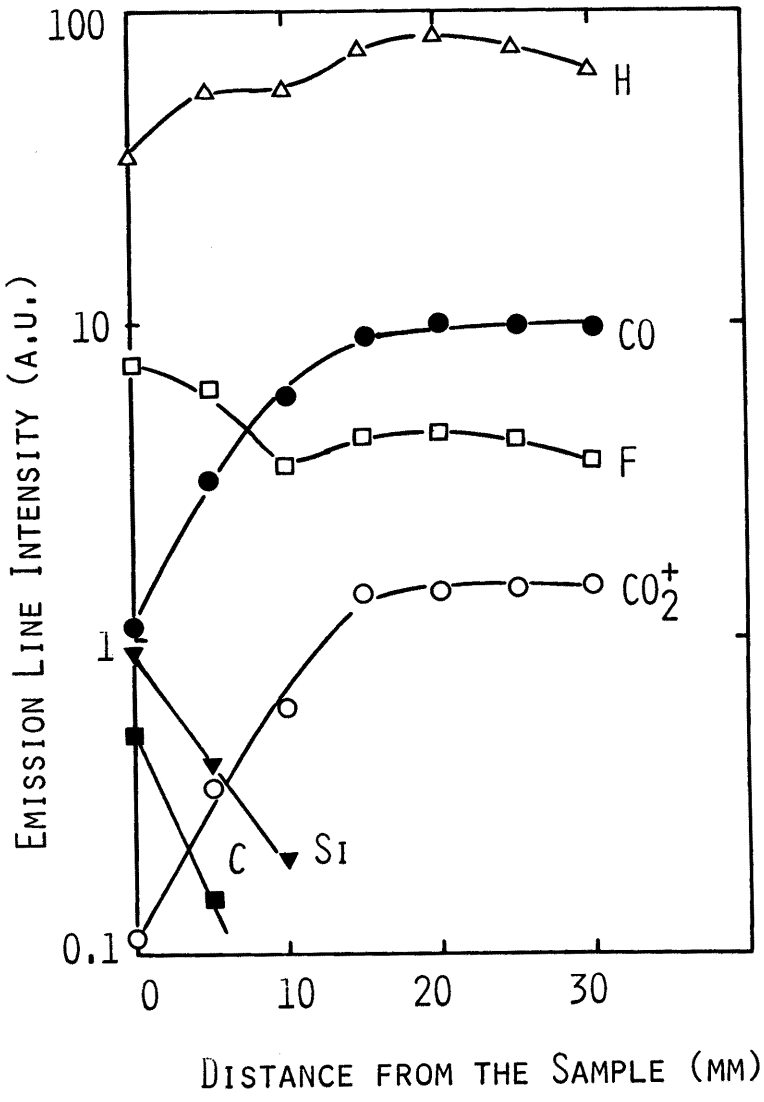

Fig.2.9 Emission line intensities during RSE of Si at 0.04 Torr and 60 W as a function of distance from the sample surface. C(2479 A).

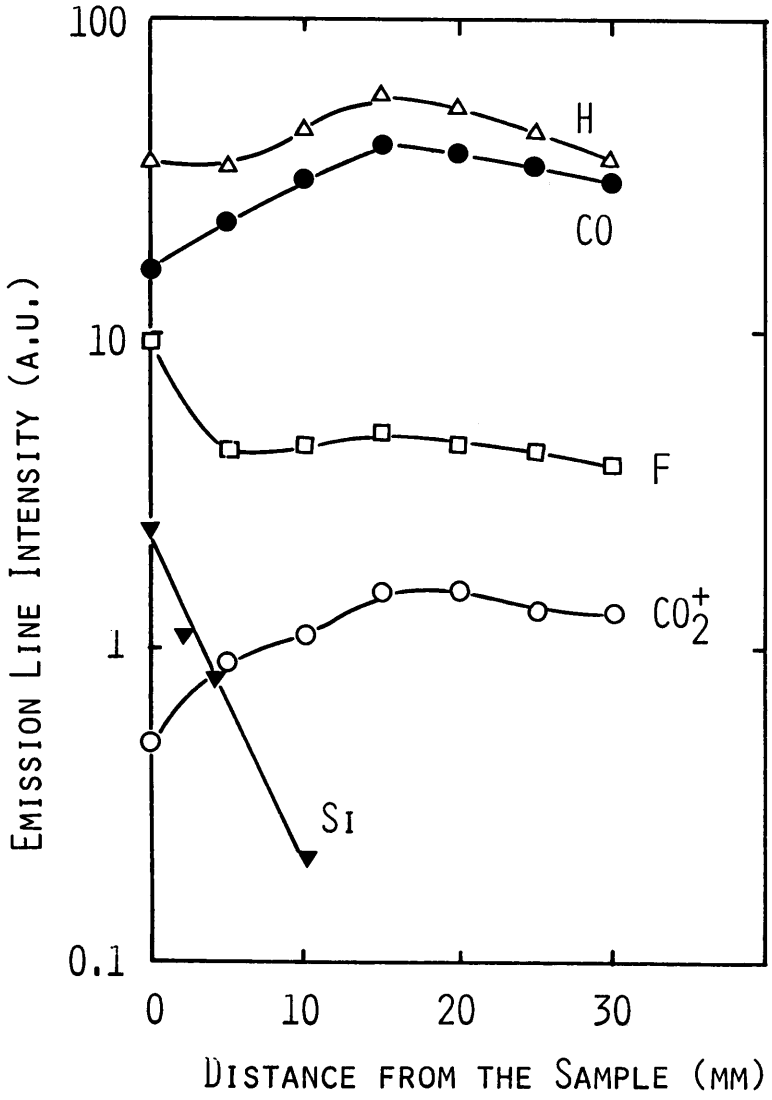

Fig.2.10 Emission line intensities during RSE of SiO2 at 0.04 Torr and 60 W as a function from the sample surface.

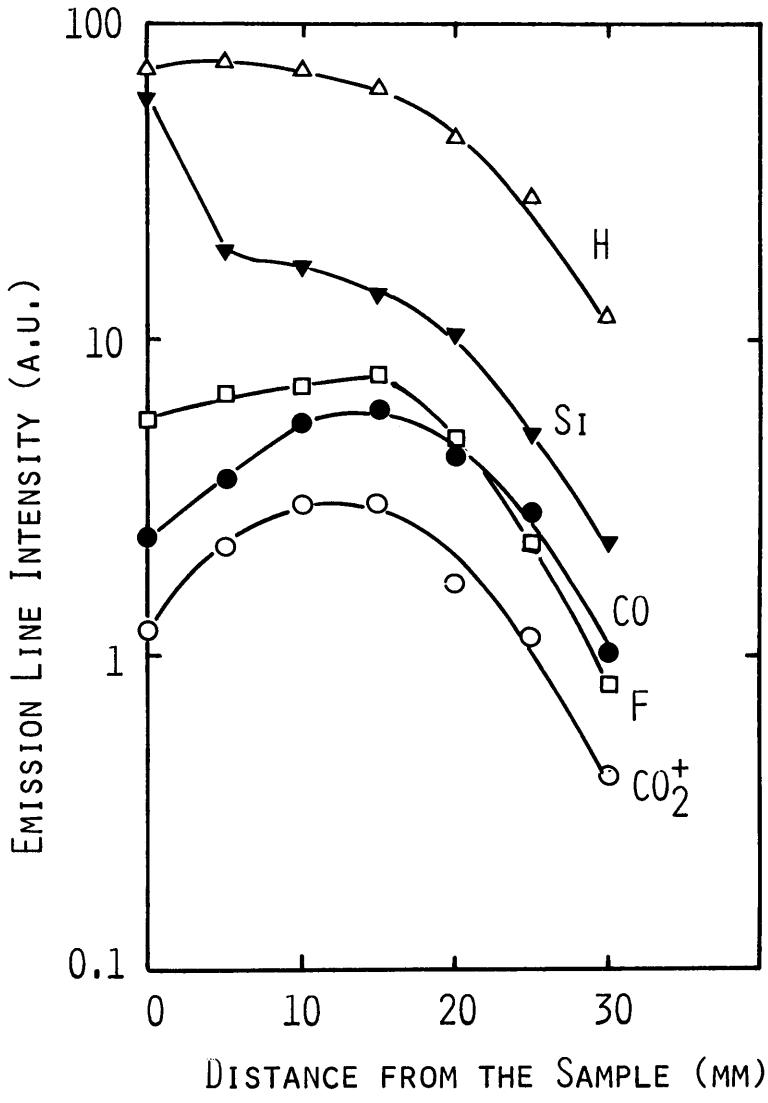

Fig.2.11 Emission line intensities during the RF glow discharge of SiF4 gas as a function of distance from the sample surface.

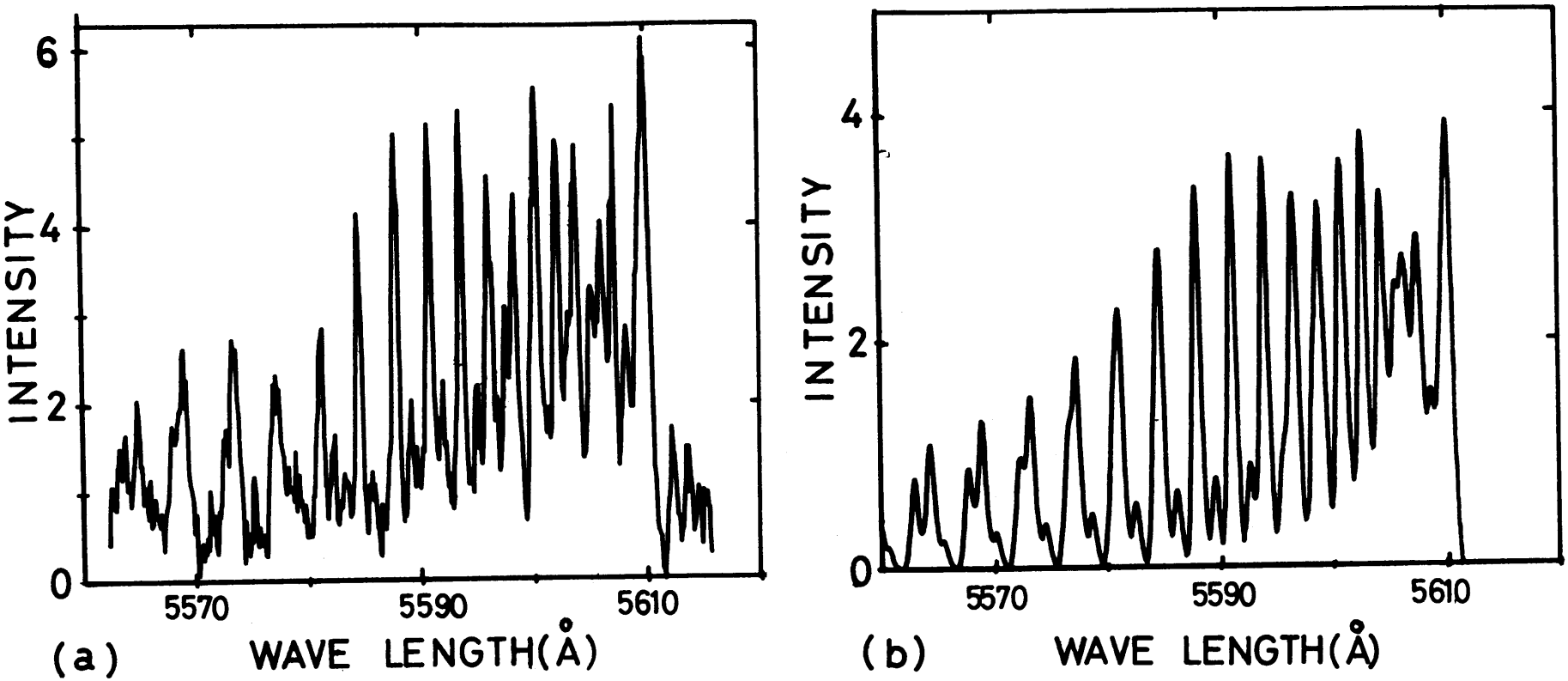

Fig.2.12 Emission spectra of "Angstrom" system (0,3) band from C2F6 plasma at 0.04 Torr pressure and 20 W applied power. (a) Spectra observed near the negative glow. (b) Spectra calculated at Tg=450 K.

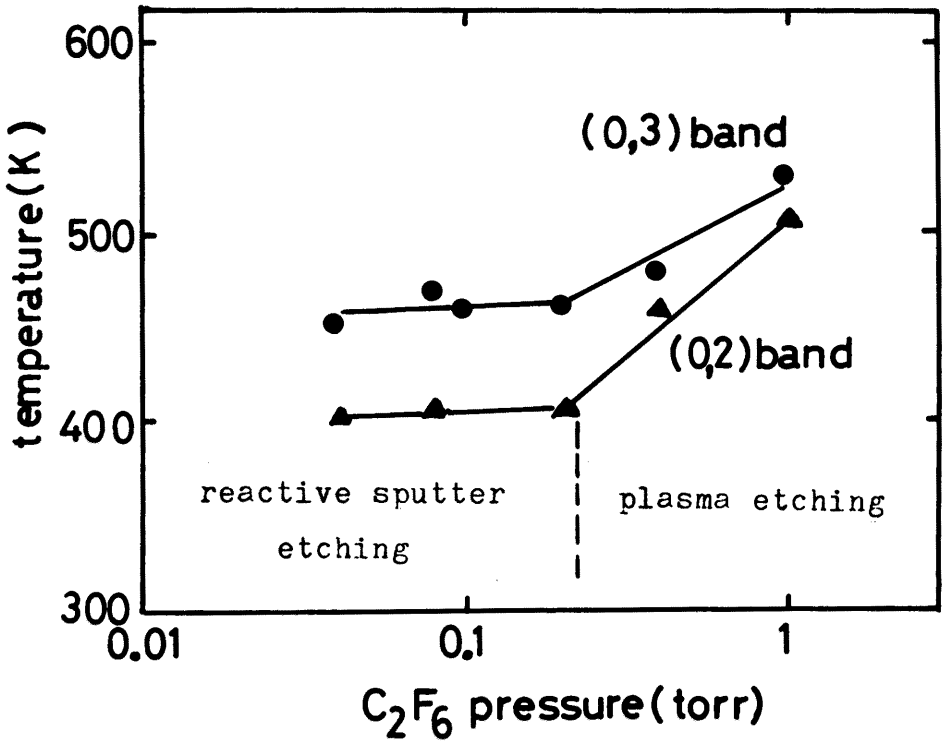

Fig.2.13 Dependence of gas temperature on C2F6 pressure at 20 W applied power. Temperatures were simulated using CO (0,3) and (0,2) bands.

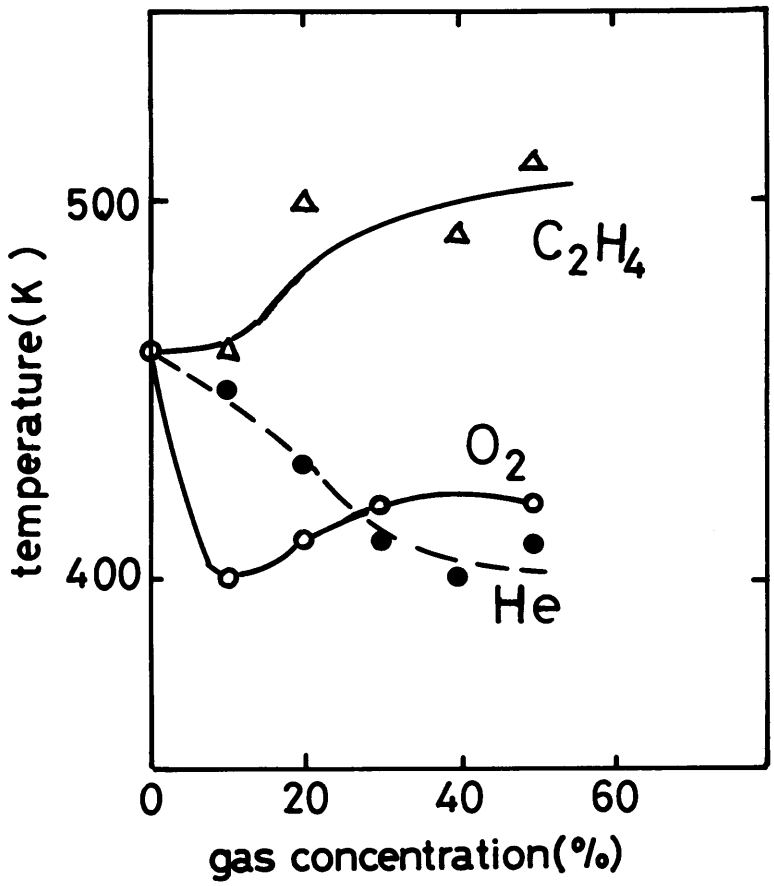

Fig.2.14 Relationship between gas temperature and added gas percentage in C2F6-He, O2 and C2H4 mixtures at 20 W applied power and 0.04 Torr total pressure.

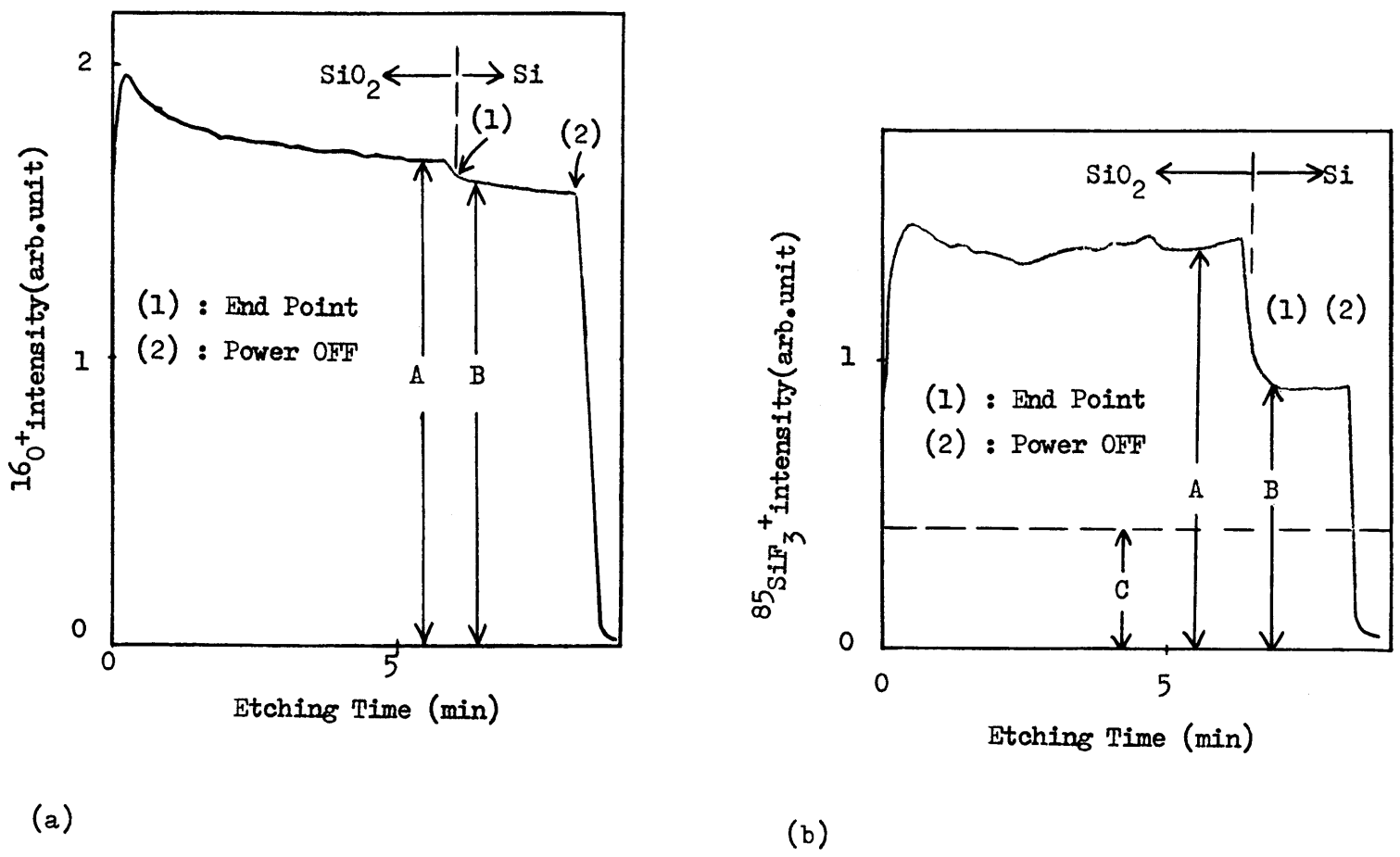

Fig.2.15 Mass spectral intensity-time curves using $^{16}O^{+}$ and $^{85}SiF_3^{+}$ as etching monitor. Applied power; 100 W, SiO2 area exposed; 5.5 cm^2, ratio of SiO2 to Si etching rate; 4.71.

Table 2.3 Decrement ratios of various mass spectral lines as etching monitor at SiO_2–Si interface.

Method	Monitoring signal	Decrement ratio (%)
1	$^{16}O^+$	4.6
	$^{32}O_2^+$	0.0
	$^{28}CO^+$	0.0
	$^{44}CO_2^+$	5.8
2	$^{29}Si^+$	13.4
	$^{30}Si^+$	7.5
	$^{47}SiF^+$	10.1
	$^{66}SiF_2^+$	11.3
	$^{85}SiF_3^+$	37.8
	$^{104}SiF_4^+$	19.2

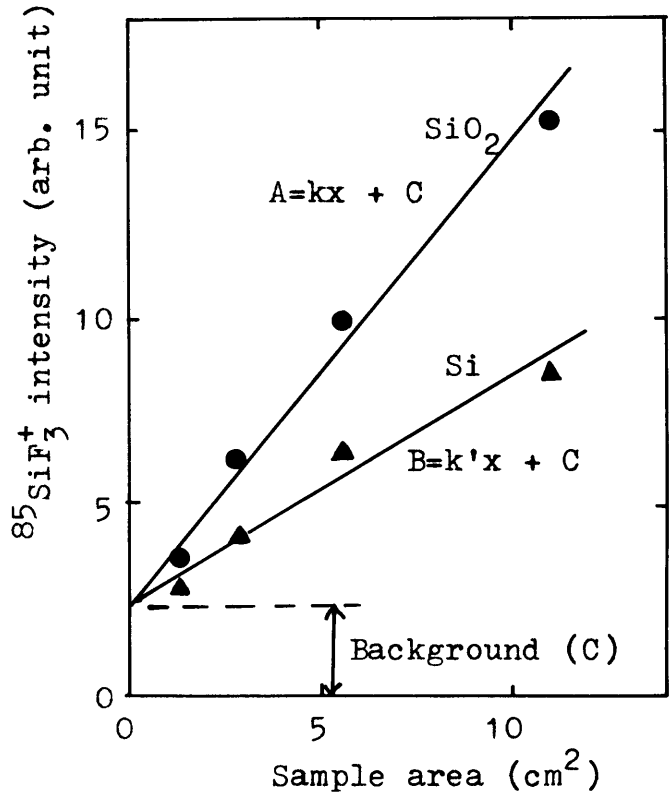

Fig.2.16 Dependence of $^{85}SiF_3^+$ intensity on sample area in etching Si and SiO2 substrates. CF4+C2H4 total pressure; 4×10^{-2} Torr, applied power; 60 W.

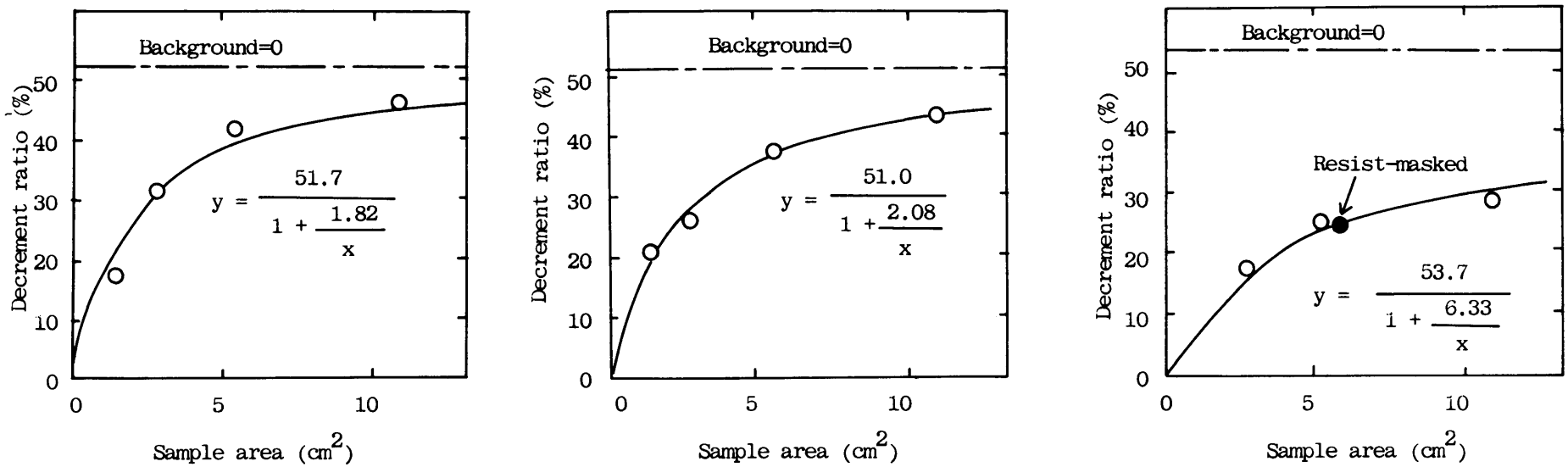

Fig. 2.17 Dependence of decrement ratio of $^{85}SiF3^{+}$ intensity on SiO2 area exposed. Applied power; (a) 100 W, (b) 60 W, (c) 40 W. Solid circle shows result observed in etching 2 μm line and space pattern masked with a resist film.

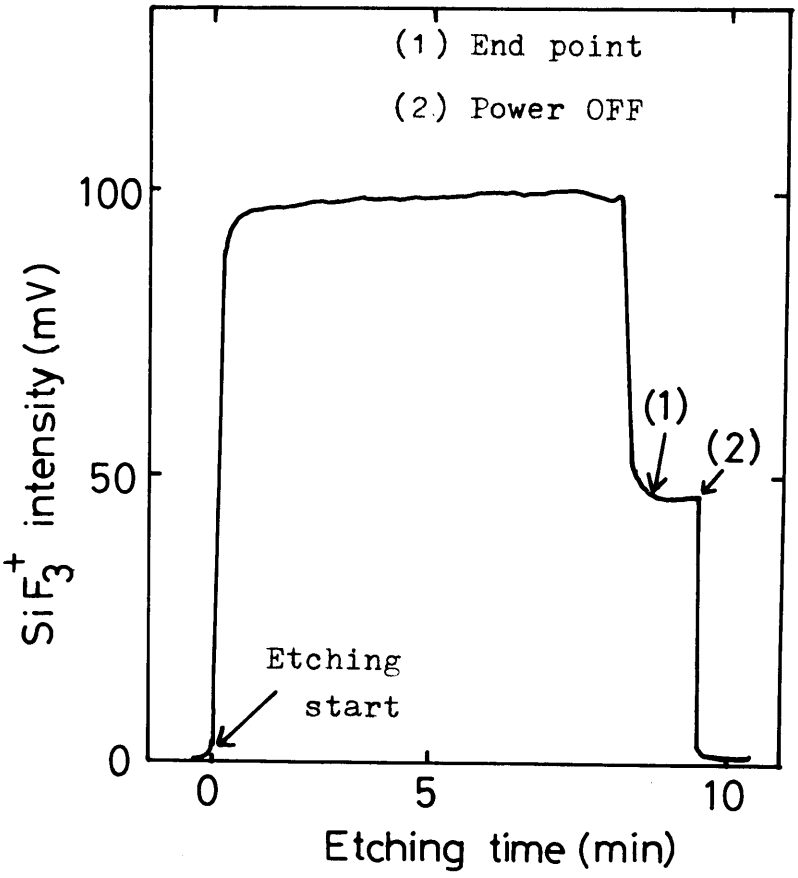

Fig.2.18 Typical $^{85}SiF_3^+$ intensity-time curve under following conditions. C2F6 pressure; 4×10^{-2} Torr, applied power; 50 W, C2F6 flowrate; 9cc/min, Pressure in mass analyzer; 8×10^{-7} Torr, SiO2 area exposed; 9.8 cm^2, target; carbon.

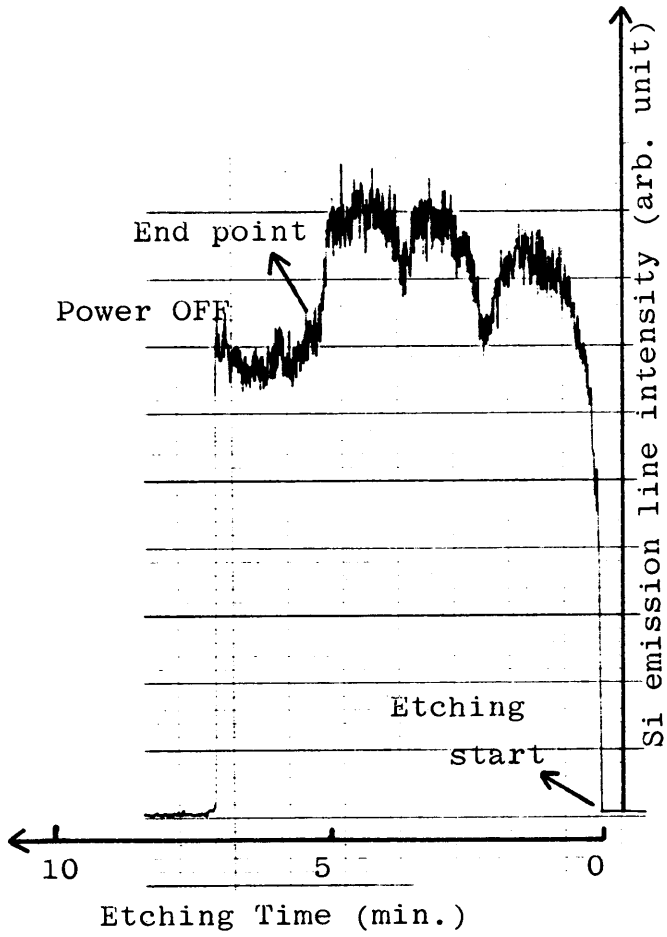

Fig.2.19 Si emission line (2882 A) intensity-time curve using 60 cm grating spectrometer under standard etching conditions.

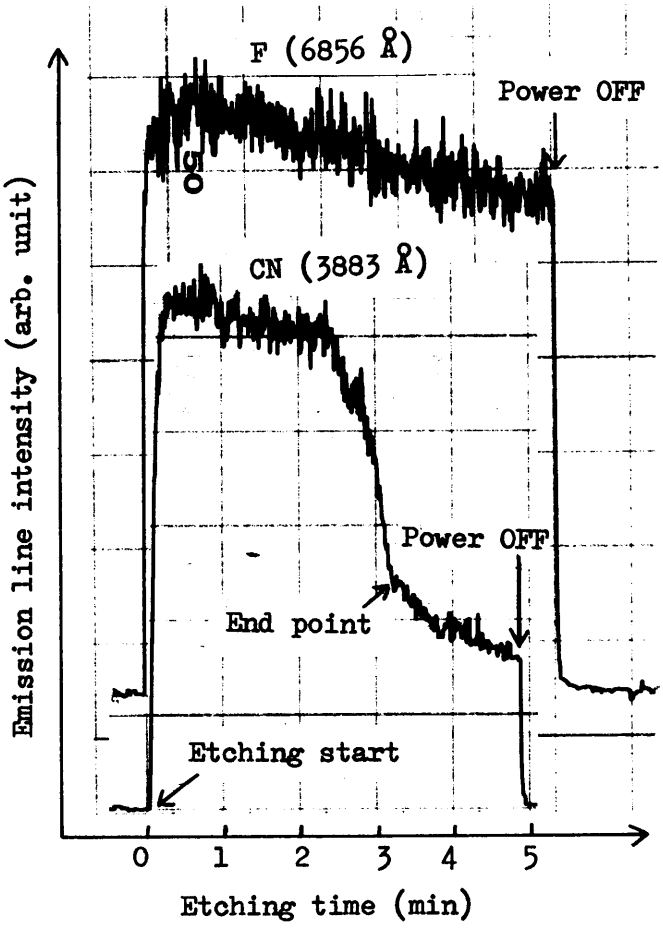

Fig.2.20 F and CN emission line intensity-time curve during RSE of Si3N4 films on Si substrates. RSE; 0.04 Torr, 60 W, Sample area; 20cm^2

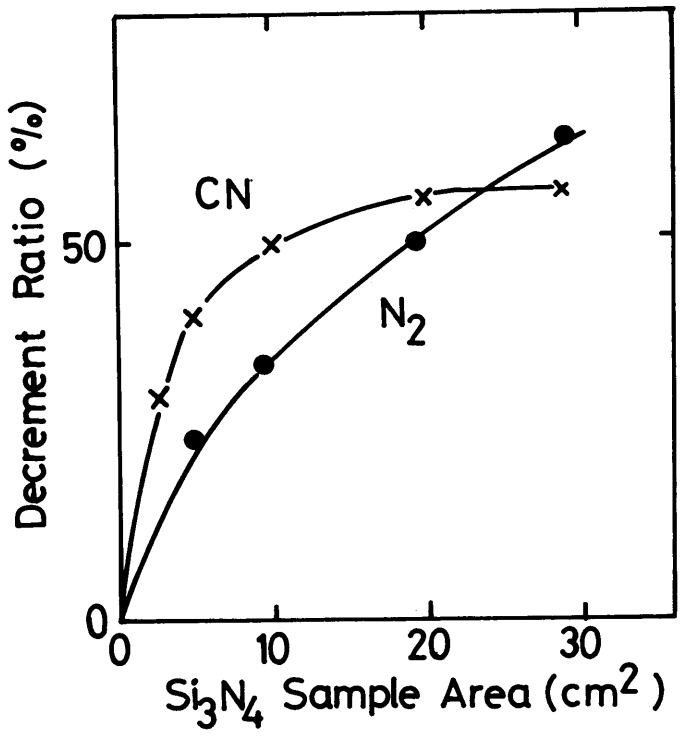

Fig.2.21 Signal decrement ratio of CN and N2 lines at the Si3N4-Si interface as a function of Si3N4 sample area. RSE; 0.04 Torr, 60W.

Chapter 3 Surface Analysis of Reactive Sputter Etched Silicon Wafers *

3.1 Introduction

Reactive sputter etching (RSE) is an effective technique to selectively etch SiO2. The selectivity in etching SiO2 is considered to be due to high energy (several hundred eV) ion bombardment. Therefore, this technique is suitable for fine pattern delineation without undercutting. However, it can be anticipated that Si and SiO2 surfaces may be subjected to damage by high energy CF_3^+ ions(3.1).

Only a few studies have been reported on the contamination of silicon surfaces during dry etching. Hosokawa et al(3.2) reported that traces of C and Cl were detected on a Si surface etched by CCl2F2(R-2) gas and these contaminations could be removed by a slight bombardment of Ar^+ ions. Yang et al(3.3) showed that Si surfaces plasma etched with CF4 were contaminated with carbon due to deposition from plasma decomposed source gas(3.4). Coburn(3.1) investigated the surface chemistry of Si subjected to CF_3^+ ion bombardment in AES analytical chamber by means of AES and XPS. In order to introduce the RSE technology into LSI fabrication process, RSE surfaces should be evaluated in lights of surface contaminations and crystalline defects.

In this chapter, surface contaminations are characterized using AES (Auger Electron Spectroscopy), SIMS(Secondary Ion Mass Spectrometry) and XPS (X-ray Photoelectron Spectroscopy) in order to elucidate the etching selectivity in RSE and evaluate the

*Most of this part has been reported in ref. (A.3).

amount of RSE-caused contaminations.

3.2 Experimental

The experiments were carried out using the diode RF sputter etching apparatus with a target 100 mm in diameter. C2F6 gas was used as the etching gas. Samples were Si(100) substrates and SiO2 films grown by thermal oxidation in wet O2. Surface analysis was performed with SIMS, XPS and AES (PHI, ESCA/Auger Electron Spectrometer). Depth profiles were obtained with AES and SIMS, and the chemical compositions of the etched surfaces were determined from XPS data. The studies of XPS chemical shifts with a signal averaging system and electron-stimulated desorption with AES were also performed. In situ AES studies were done using the Auger Electron Spectrometer coupled with the RSE apparatus in vacuum (10^{-4} Torr) in order to investigate the RSE surface without the effect by contamination from air.

3.3 Results and discussion

(1) Surface contamination

The SiO_2-Si interface, determined from $^{85}SiF_3^+$ monitoring, was checked by XPS. The sample was an SiO_2 film (5000 A) on an Si substrate. Figure 3.1 shows XPS spectra of surface after etching in 4 steps; 3min (Point A), 6min (Point B), 6.5min (Point C), and 12min (Point D). As shown in the schematic $^{85}SiF_3^+$ intensity-etching time curve in Fig. 3.1, the SiO_2 film still remained on the Si substrate at Point A. This was confirmed by the XPS spectra of the RSE sample surface at Point A, where the O1s peak is the strongest and the Si peaks show a chemical shift. Then at Point B, where the mass signal just begins to decrease abruptly, the O1s peak is considerably diminished. At Point C, where the decrease in the mass signal intensity terminates completely, indicating the complete removal of the SiO_2 overlayer on Si, the O1s peak is also small. At Point D, the XPS spectra also indicate that no SiO_2 film remains on the RSE surface. Since RSE samples were transfered into the XPS specimen chamber via room air within 10 minutes and analyzed by XPS, the etched Si surface was slightly oxidized. The difference between the C and F peak heights on etched Si and SiO_2 will be discussed elsewhere.

On the surface of RSE Si, four peaks due to Si, C, O and F were detected. The dependence of F and C contaminations on the etching conditions was investigated. Figure 3.2 shows F KLL Auger peak heights and F SIMS peak heights as a function of the RF power applied to the lower electrode. A tendency for a large amount of F contamination to remain at high powers was observed.

Fig. 3.3 shows F peak heights as a function of etching pressure of C2F6. With regard to C contamination, the amount could not be obtained exactly because of carbon adsorption from room air after RSE. We investigated the relative carbon contaminations on several series of samples etched at various applied powers and etching pressures. The tendency was for the carbon contamination to increase with higher power levels and lower pressures. As described later this tendency was confirmed. In etching at low pressures, namely RSE, the effect of CF3 ion bombardment becomes dominant, so that the surfaces are subjected to large C and F contaminations.

Next, the profiles of these contaminations were investigated by means of SIMS in-depth analysis. It is shown that the F-contaminated surface layer by RSE was about 20-30 A thick at 80 W applied power from F, Si in-depth profiles, and the depth was dependent on the applied power. Fig.3.2 shows profiles normalized by Si peak height on Si surfaces processed at various annealing conditions. The amount of F contamination caused by reactive sputter etching (P(C2F6)=0.04 Torr) was several times as large as that caused by plasma etching (P(C2F6)= 1 Torr). These contaminations were removed by means of heat treatment in a H2+N2 atmosphere.

The amount of the C and F contaminations on the RSE SiO2 surface was from one fifth to one twentieth of that on Si, as shown in Fig. 3.5. This is considered to be due to the effect of the oxygen atoms disassociated from SiO2 causing oxidation of the carbon contaminations.

The C depth profile proved to extend to a greater depth than the F profile. The RSE surface was covered with an Al film in order to make the difference between C and F profiles clear, and AES in-depth analysis was performed. The maximum C profile position was a little deeper than that of the F profile as shown in Fig.3.6. This indicates that a carbon layer exists on the surface with a CFx layer on top of that.

(2) Surface Chemistry

We found that RSE results in a large amount of carbon and fluorine contaminations on the etched Si surfaces when lower pressure and higher applied power. Figure 3.7 shows the Si LVV Auger peak shapes of RSE Si surfaces. The peak at 84 eV is thought to be due to Si-CFx bondings because this peak intensity shows one-to-one correspondence to C and F peak intensities. Furthermore, it is found from the results of thermal desorption spetrometry of RSE Si surfaces that the mass spectra of CFx have the binding state of 3.1 eV. In this analysis, the first order desorption was supporsed to determine the binding energy. In addition, we found the existence of β-SiC on the RSE surface of some Si substrates by means of Transmission Electron Microscope. In this way, RSE surfaces show different chemical states dependent of RSE condition.

Electron-stimulated desorption using AES was performed to investigated the strength of the chemical bonding of F atoms. F KLL Auger peaks from Si, Si3N4 and SiO2 are shown as a function of time of exposure to a 3 keV 22 μA electron beam in Fig. 3.8. F on the Si surface adhered most strongly among these materials, probably because the Si surface is covered by a large amount of carbon layer combined with F. The F resulting from RSE, curve (a), adhered more strongly than F by plasma etching, curve (b). This strong adhesion might be attributed to the ion bombardment effect of RSE.

Next, we investigated the change of the surface composition by annealing in N2+H2 atmosphere. The composition was determined

using XPS data and sensitivities. The amount of C contamination did not change by annealing at 441 C, while the F contamination almost vanished. This indicates that, at first, only the CFx layer was removed by thermal desorption. The carbon layer was removed from the surface or diffused into the bulk at higher temperatures. Annealing at over 600 C caused the oxygen concentration to increase, and then a silicon oxide , namely a natural oxide, was formed.

In order to investigate the surface chemistry in detail, chemical shifts of Si and C were measured by means of the signal averaging system (about 200 times averaging). On as-etched Si, a shoulder peak (ΔE=2.5-3.0 eV) due to Si-C bonding was observed, as shown in Fig.3.10. After annealing at 441 C, this peak, presumably containing not only Si-C but also Si-O bonding, becomes larger than the elemental Si peak. After heat treatment at 800 C, a large peak due to SiO2 state (ΔE=4 eV) and a small Si peak were observed. As for the SiO2 sample, the spectrum from the as-etched surface which has almost no contaminations was the same as that from the unetched surface, as was expected.

With respect to the C 1s peak, three shoulder peaks (ΔE=2.9, 5.5, and 7.5 eV) were observed as shown in Fig. 3.11. Based on the XPS study of Siegbahn et al (3.5), the peaks 1,2, and 3, respectively, are due to CF, CF2 and CF3 bondings. Thus a CFx layer is formed on the Si surface subjected to RSE. Only one shoulder peak corresponding to the CF bonding appeared on the plasma etched Si surface.

(3) In situ Auger Electron Spectroscopy of dry-etched Si surfaces

We found that carbon plays an important role in RSE in a sense of etching selectivity of SiO2. However the quantitative analysis of carbon contamination was not possible because of surface contamination caused during sample transfer from the RSE chamber to the AES analytical chamber via air. Therefore we made the in situ AES apparatus which is a combined system of RSE and AES with the transfering path evacuated down to 10^{-4} Torr by sorption pumps. The schematic diagram of the system is shown in Fig.3.12 and the photo in Fig.3.13.

Figs. 3.14 and 3.15, respectively, show the AES in-depth profiles of RSE Si and SiO2 surfaces. The RSE condition was 0.04 Torr, 1.0 W/cm^2 and 3 minute etching. The concentration calculation was performed using the AES peak-to-peak sensitivities in the PHI data book, and the depth was estimated using the average sputtering rate determined by the sputtered depth. As shown in the profiles, carbon was found to penetrate into the Si wafer deeper than 100 A, while there was almost no oxygen , which indicates the validity of this in situ AES analysis. Fluorine contamination reached up to 50 A.

In order to make clear the effect of surface contamination due to exposure to air after RSE, the RSE Si wafer was exposed to air for 2 minutes and 10 minutes, and introduced into the AES analytical chamber. As shown in Figs. 3.14, the exposure to air was found to cause the RSE surface less contaminated with carbon and more oxygen-rich. This result implies that the RSE surface is very reactive and easy to form volatile compounds such as COx or

COFx. Furthermore, it suggests that in situ analysis is inevitable to discuss the carbon contamination due to RSE.

On the other hand, there was almost no carbon contamination on the SiO2 substrate and quite a small amount of fluorine contamination, as shown in Fig. 3.15. Therefore, the clean SiO2 is subjected to CF_x^+ ion bombardment all the time, while the Si surface suffers from carbon accumulation which might act as a prohibitor of the reaction between CFx and Si, and decrease the etching rate of Si.

Next, we investigated the dependence of the carbon profile on RSE condition, namely the applied power density and etching duration. First of all, the power dependency is discussed. Figure 3.16 shows the C profiles as a function of the applied power density at 0.04 Torr C2F6 for 3 min etching. In this RSE apparatus, 80 W($1 W/cm^2$) applied power corresponds to about 1 kV self-bias voltage and 1 mA/cm^2 current density. The larger the sef-bias voltage is, the deeper the C profile is, where the ion dosage is almost the same in three cases. Therefore, it is concluded that C contamination is due to C^+ ion implantation or the knock-on implantation of surface C contamination by CF_3^+ ions with self-bias potential.

The dependence of C contamination on the etching duration was investigated in order to elucidate the ion dosage effect on Si substrates. Figure 3.17 shows in-depth C profiles as a function of etching duration. The profiles become deeper with increasing ion dosage, which is presumably due to knock-on effect and C accumulation.

In order to investigate this C implantation effect, the amount of accumulated carbon atoms was calculated from Fig. 3.17 and plotted against the etching duration in Fig.3.18. Since the integration was carried out from the surface to 100 A depth, the true values might be 10 to 20 % larger than those in this diagram.

Although the exact ion dosage cannot be obtained, rough estimation is possible by means of the effective power density and the self-bias voltage. In this way, the ion dosage at 80 W and 3min comes to 1.1×10^{18} cm^{-2}, while the residual carbon number is nearly two orders of magnitude smaller than this calculated value. However, at 5 second etching the carbon contamination (order of 10^{15} cm^{-2})is close to the calculated dose (order of 10^{16} cm^{-2}).

This result can be regarded as comparable because the number of CFx^+ ions impinging into the substrate should be smaller than the product of etching duration and the total current density calculated by $J=1$ W/cm^2 /1 kV=1 mA/cm^2. If we supporse the ratio of CFx^+ ion number to that product is about 10 %, the accumulated carbon number for the first 5 second, that is 3.2×10^{15} cm^{-2} is quite comparable to the calculated ion dose, that is 3×10^{15} cm^{-2}.

Therefore, we can say that at the first stage of RSE CFx^+ ions impinging into the surface forms the carbon accumulated layer, and then the coming ions sputter off the accumulation of carbon. Since this is a competing reaction of the accumulation and the sputtering, it would reach the steady state because the projected range of the knocked-on carbon was not very deep even

after 10 min RSE.

Finally, the effect of the oxygen plasma ashing to eliminate the surface accumulated carbon layer was investigated. Figure 3.19 shows the AES in-depth profiles of plasma-ashed Si surface after RSE(80 W, 3min). Carbon contamination decreased with the ashing time and almost disappeared after 10 min ashing as shown in this figure. Fluorine was not detected. There exist the natural silicon oxide on the surface. In this way, plasma ashing which is employed to eliminate the resist pattern after RSE of through-holes, for example, was found to be useful to obtain clean surfaces.

3.4 Conclusion

The surface subjected to RSE was contaminated with carbon and fluorine to a thickness 20 to 30 A. The amount of contamination was dependent on the applied power, etching pressure and etched substrate. On the SiO2 surface, only slight contamination by C and F was detected due to the effect of oxygen atoms separated from SiO2.

XPS data indicated that there exist Si-C and C-Fx bondings on the RSE Si surface. Taking into account AES in-depth profiles, it is concluded that there exist a carbon layer covering the Si surface with a CFx overlayer. These contaminations were removed by annealing for 30 min in a H2+N2 atmosphere at over 600 C.

The in situ AES system combined with the RSE apparatus was made in order to investigate the carbon contamination on the RSE Si and SiO2 surfaces exactly. While almost no carbon remains on the SiO2 surface, the carbon accumulation on the Si surface is building up with the etching duration. The carbon extends more than 100 A depth. These results can explain the etching selectivity of SiO2/Si.

The oxygen plasma ashing was found to be very useful to get rid of these carbon contaminations.

References for Chapter 3

3.1) J. W. Coburn, H. F. Winters and T. J. Chuang, J. Appl. Phys. 48(1977) 3532.

3.2) N. Hosokawa, R. Matsuzaki and T. Asamaki, Jpn. J. Appl. Phys. Suppl. 2, Pt. 1, (1974) 435.

3.3) M. G. Yang, K. M. Koliwad and G. E. McGuire, J. Electrochem. Soc. 122(1975) 675.

3.4) H. Abe, Y. Sonobe and T. Enomoto, Jpn. J. Appl. Phys. 12(1973) 154.

3.5) K. Siegbahn, C Nordliing et al, "ESCA Applied to Free Molecules" (North-Holland, Amsterdam, 1971) p. 119.

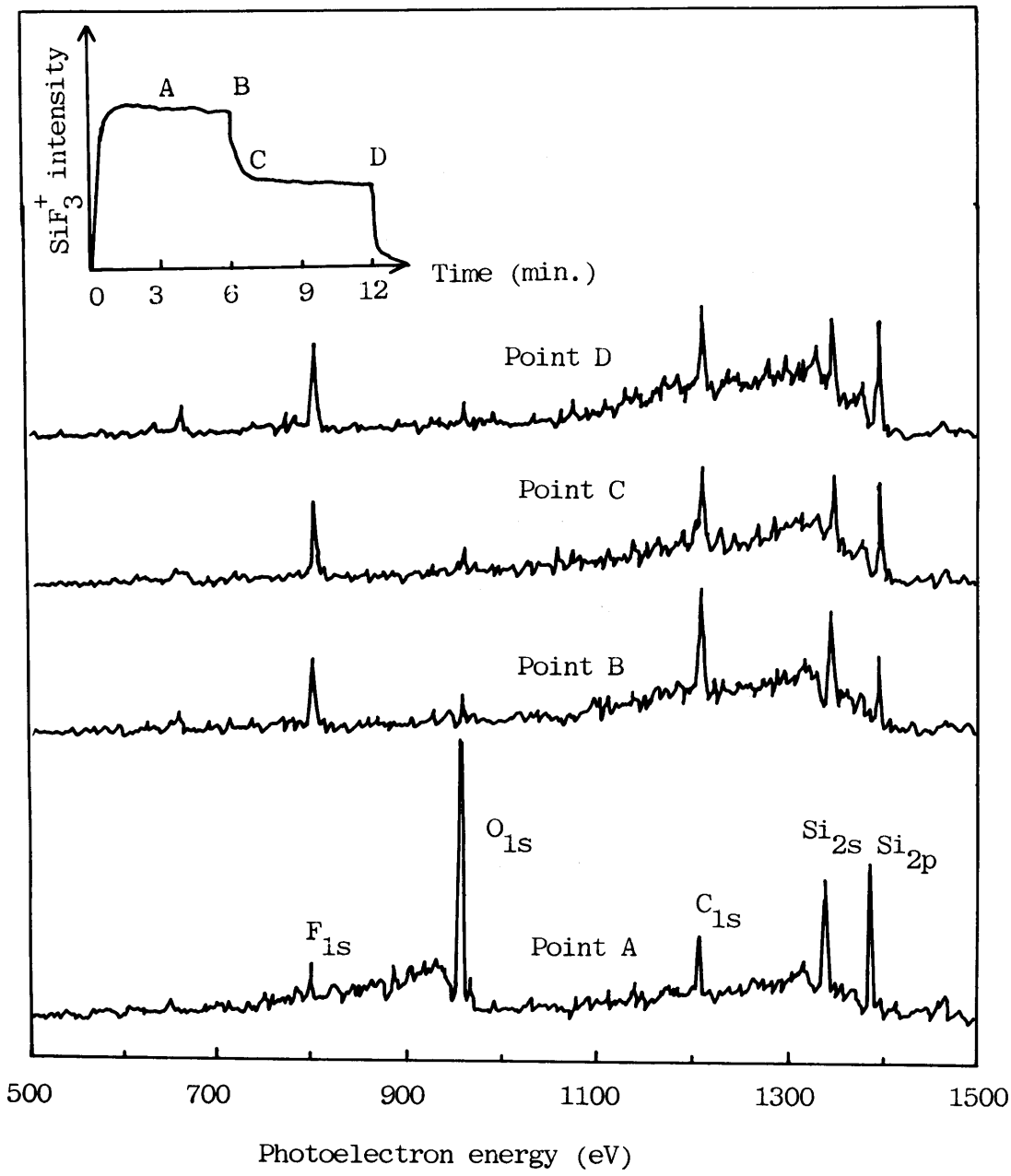

Fig.3.1 XPS spectra for four etched surfaces. Point A stands for surface etched for 3 minutes, point B for 6 minutes, point C for 6.5 minutes and point D for 12 minutes. In this case, point B corresponds to the beginning of the signal decrease and point C to the end of the signal decrease.

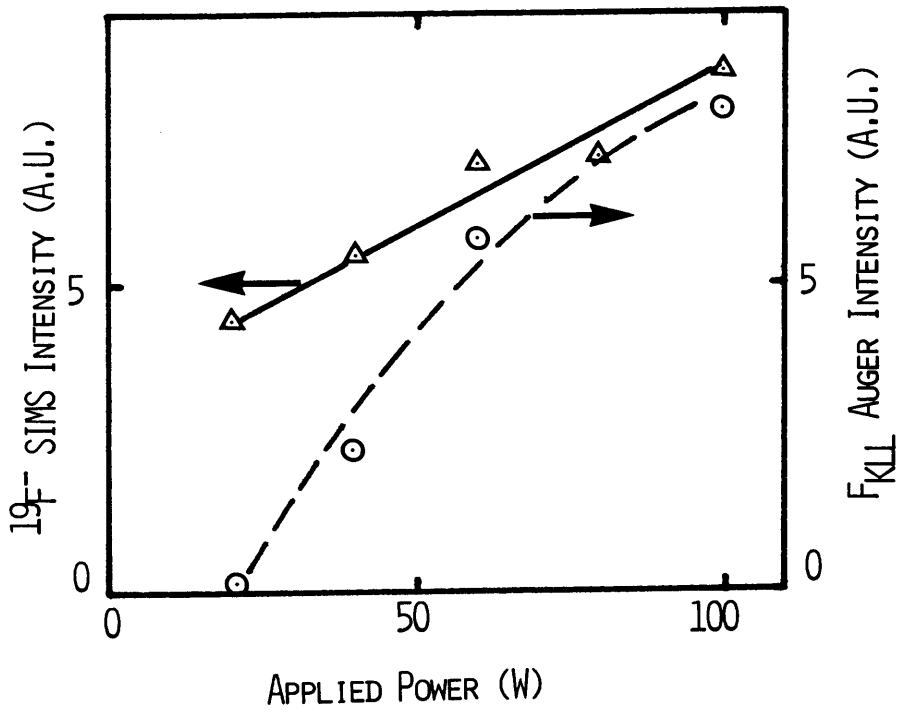

Fig.3.2 Fluorine peak height measured with SIMS and AES as a function of applied power.

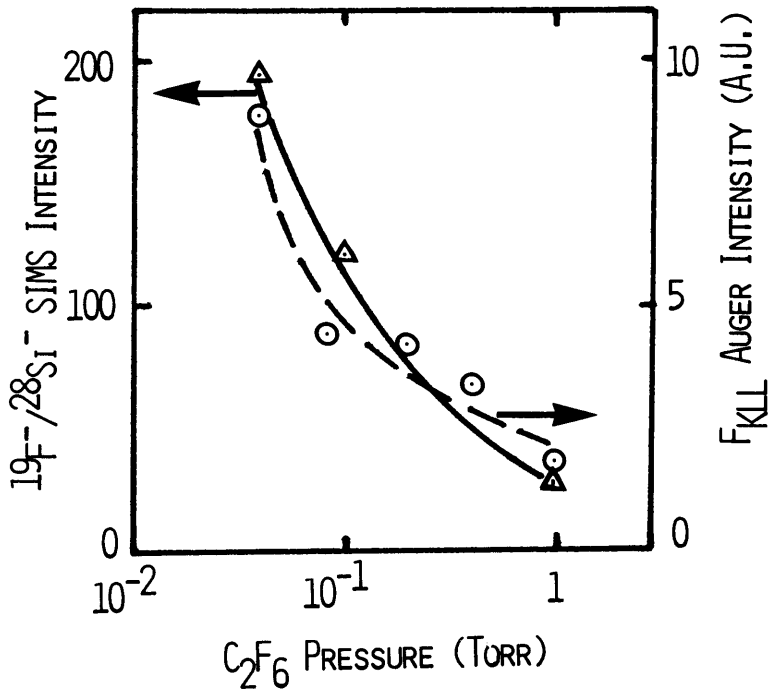

Fig.3.3 Fluorine peak heights measured with SIMS and AES as a function of etching pressure.

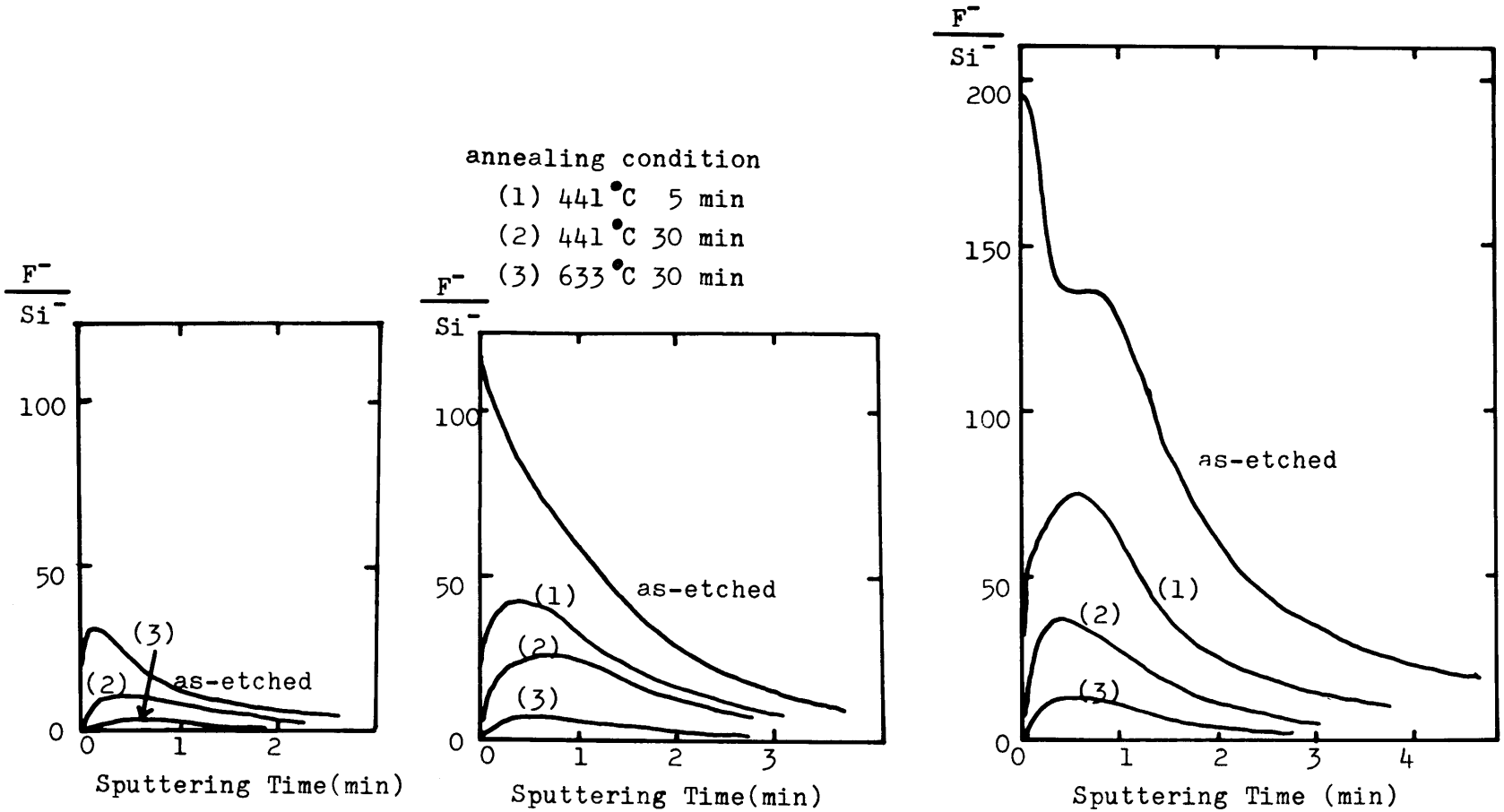

Fig.3.4 Dependence of F^- in-depth profiles on annealing temperature. Samples were Si substrates etched at three C2F6 pressures. SIMS condition: 4 keV Ar^+ beam

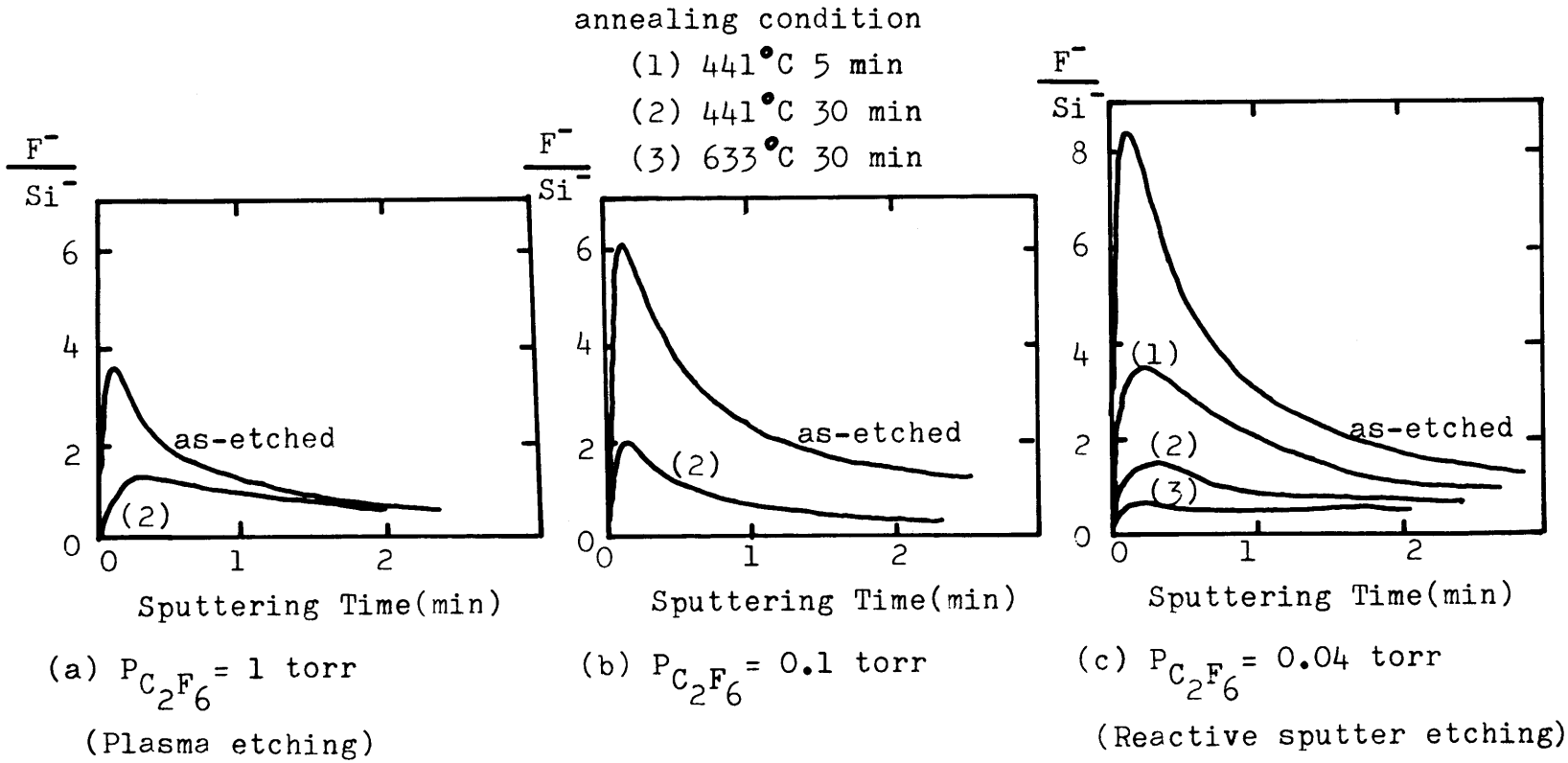

Fig.3.5 Dependence of F in-depth profiles on annealing temperature. Samples were SiO2 films etched at three C2F6 pressures. Other conditions are the same as Fig.3.4.

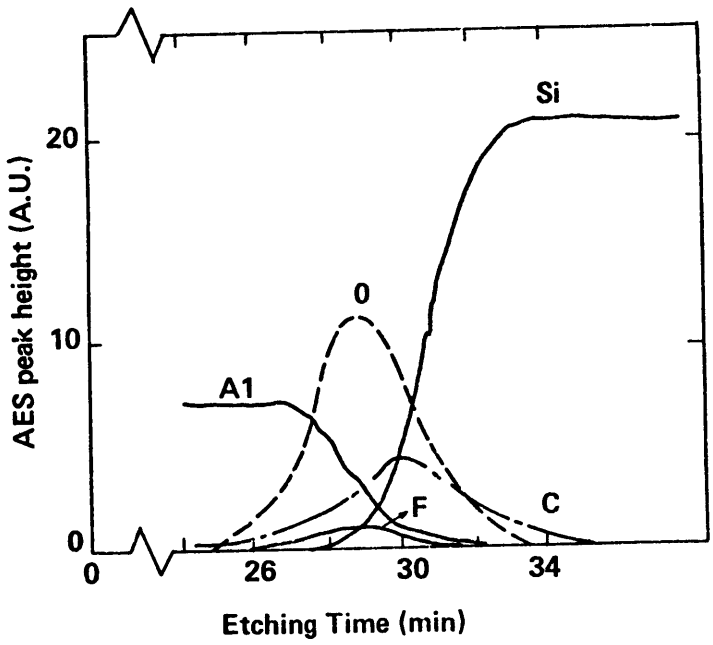

Fig.3.6 AES in-depth profile of an Al film deposited on the reactive sputter etched Si substrate. Sputter etching was performed with Ar^+ ion (1 keV, 30 mA).

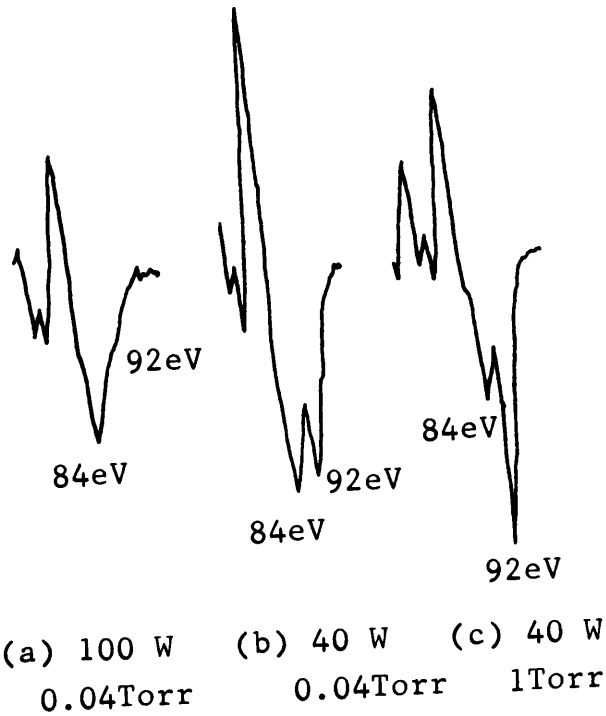

Fig.3.7 SiL_{LVV} Auger spectra of Si substrates reactive-sputter-etched at different C2F6 pressure and applied power.

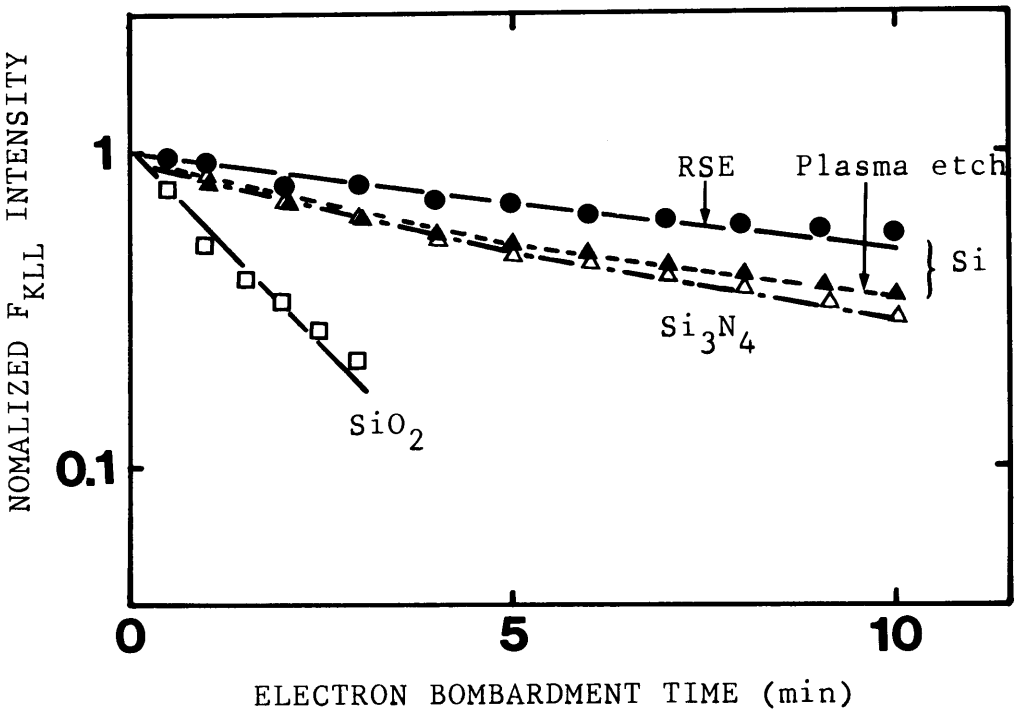

Fig.3.8 F_{KLL} Auger peak, as a functiion of time of exposure to a 3 keV 22μA electron beam, from (a) Si, (c) Si3N4 and (d) SiO2 surfaces subjected to reactive etching, and from (b) Si surface subjected to plasma etching.

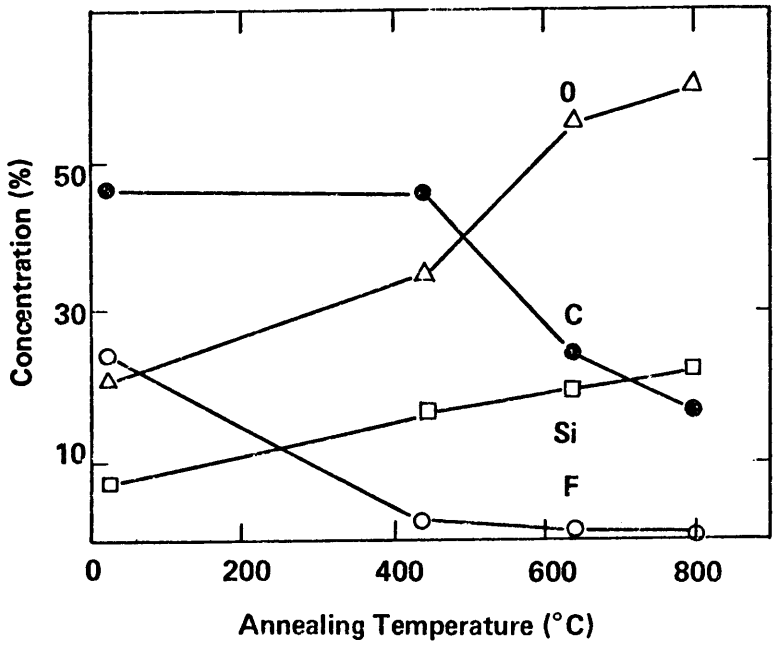

Fig.3.9 Dependence of chemical composition in the surface region of reactive sputter etched Si on annealing temperature in H2+N2 atmoshere. Annealing time is 30 min.

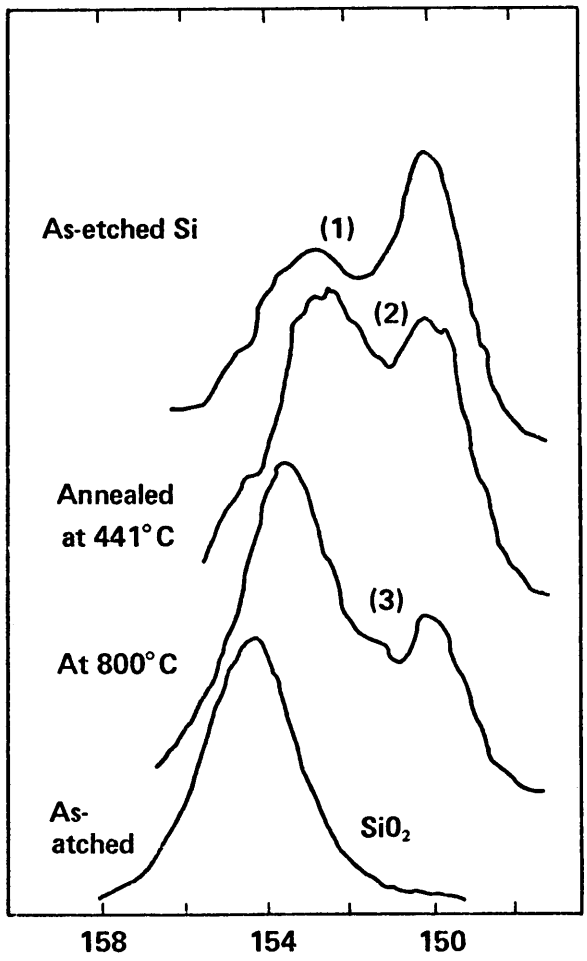

Fig.3.10 Si2s XPS spectra from reactive sputter etched Si and SiO2 surfaces using the signal averaging system. (1), (2) and (3) stand for the spectra from as-etched Si, annealed Si at 441 C and annealed Si at 800 C, respectively.

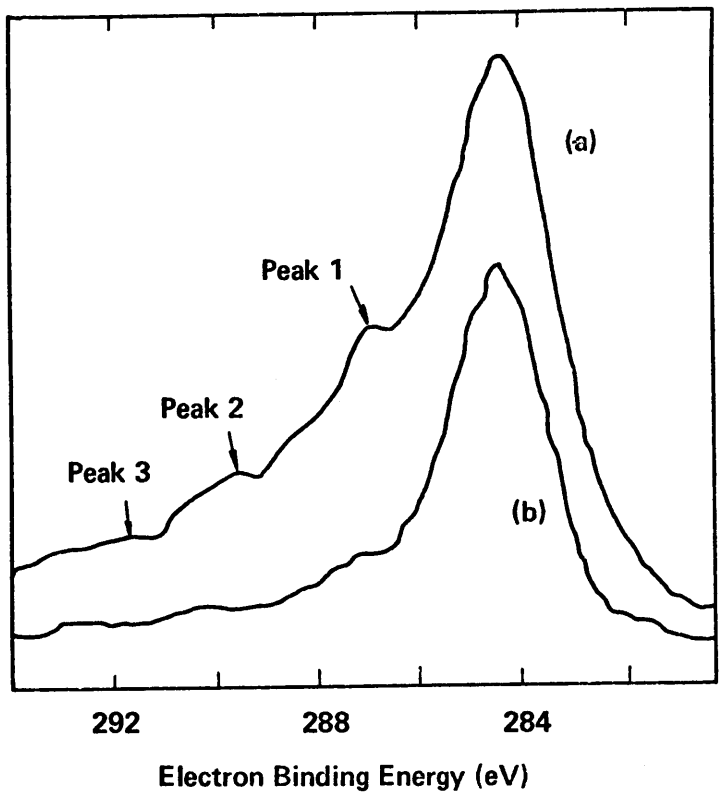

Fig.3.11 C1s XPS spectra from reactive sputter etched Si surface (a) and plasma etched Si surface (b).

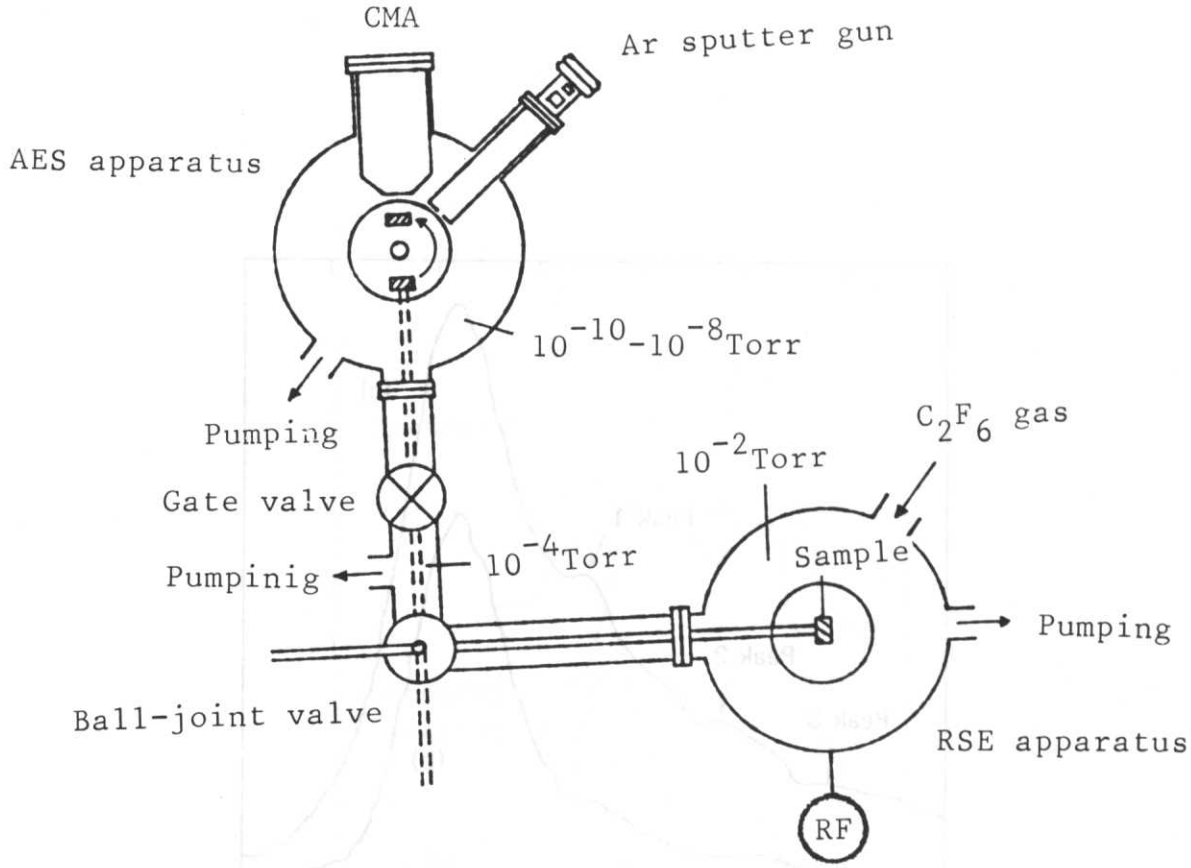

Fig.3.12 Schematic diagram of in situ AES system combined with the RSE apparatus in Vacuum.

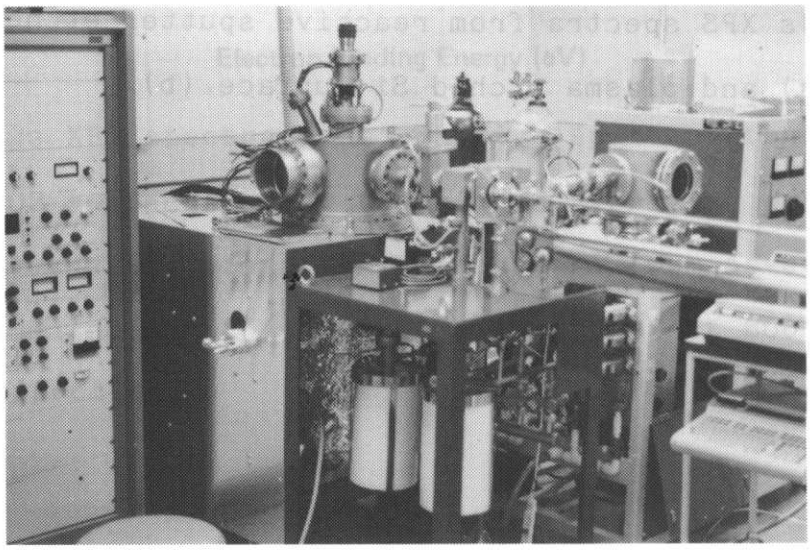

Fig.3.13 Photograph of the in situ AES system.

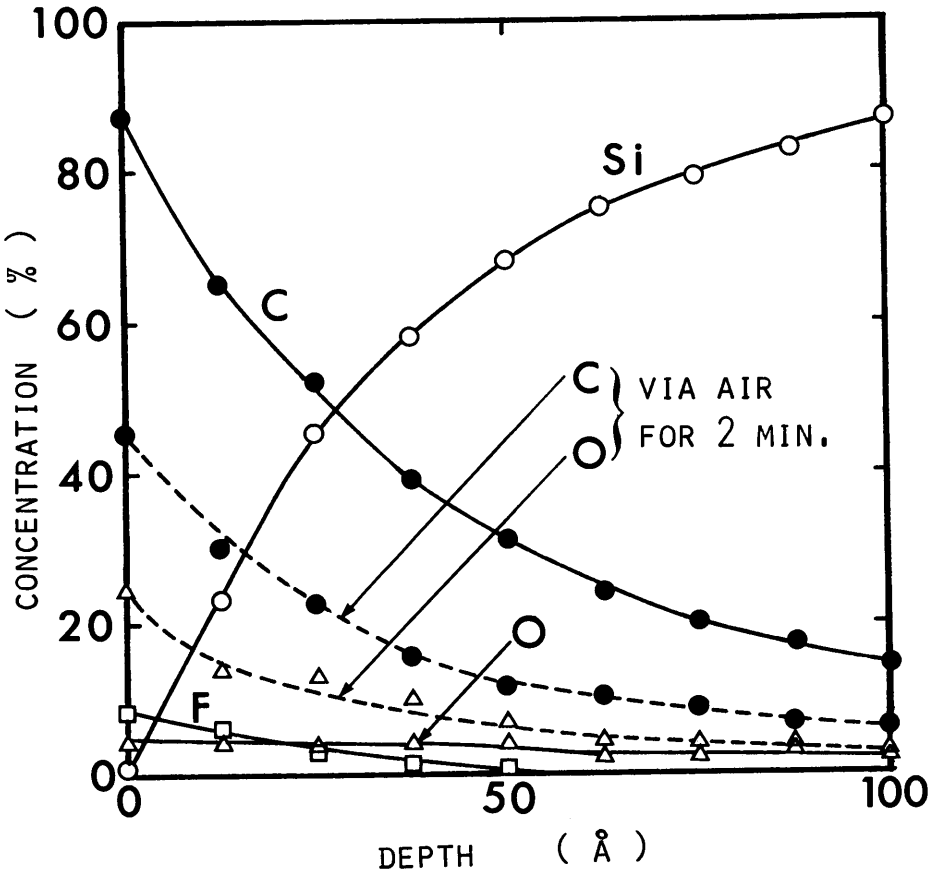

Fig.3.14 In situ AES in-depth profiles (solid lines) of RSE Si surfaces. Dashed lines indicate AES in-depth profiles of Si wafers transfered via air for 2 min.

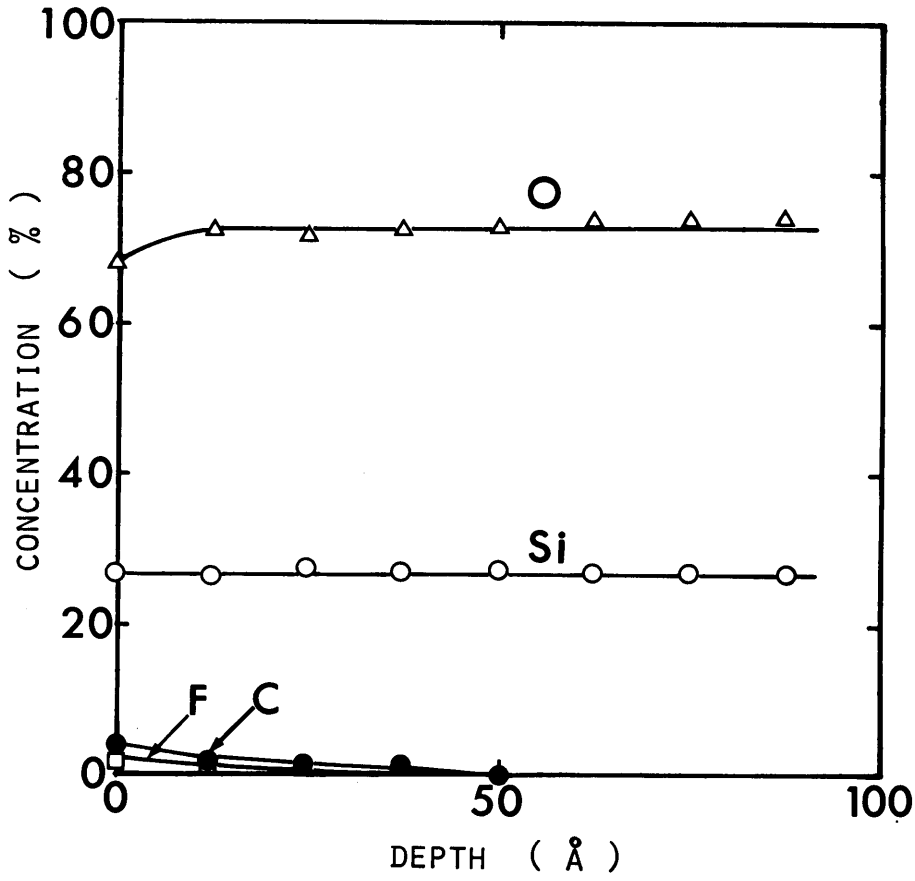

Fig.3.15 In situ AES indepth profiles of RSE SiO2 film

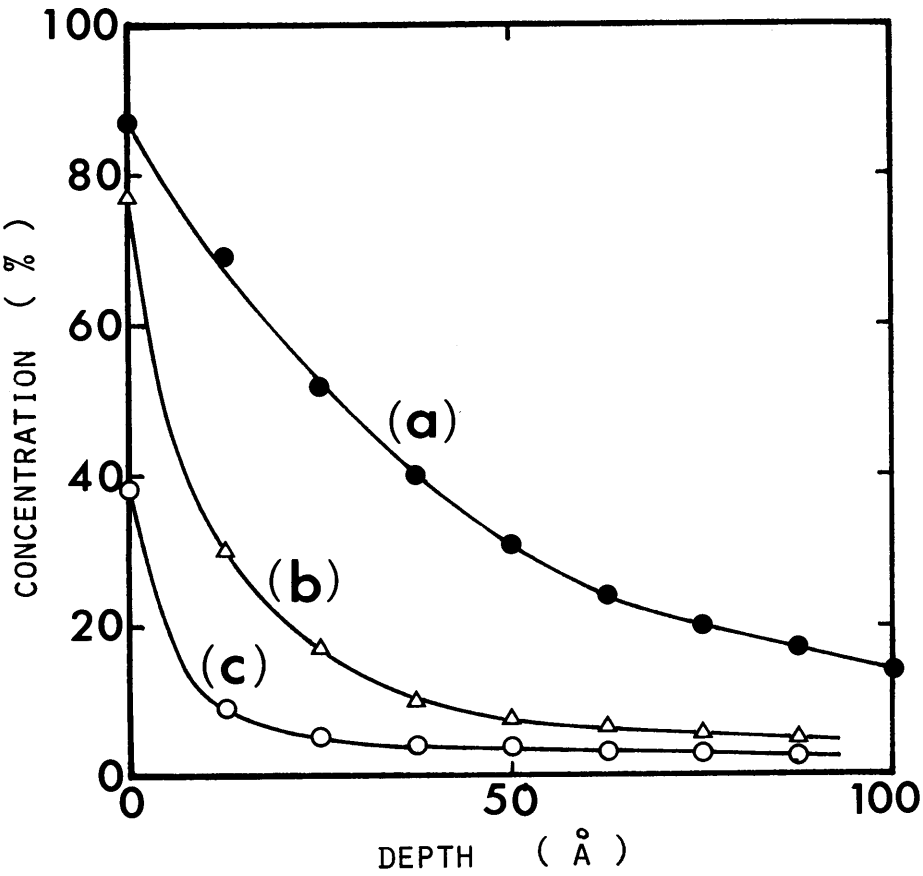

Fig.3.16 Dependence of Carbon in-depth profiles on applied power, measured with the in situ AES system.
(a) 80W, (b) 50 W, (c) 20 W

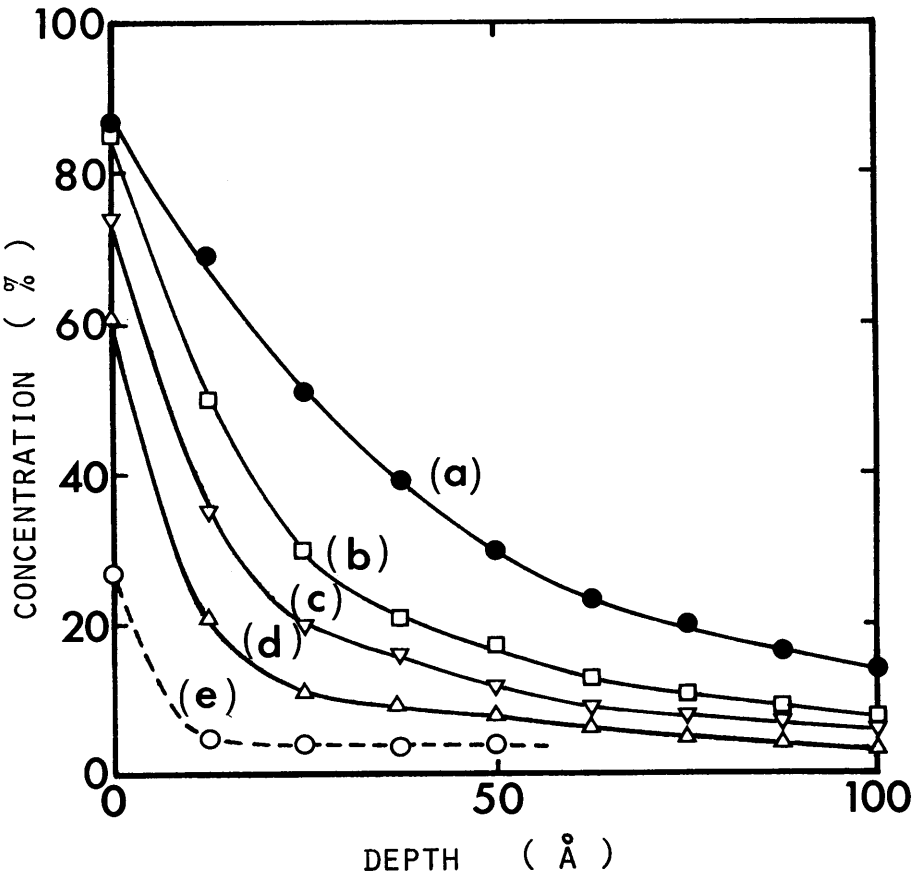

Fig.3.17 Dependence of Carbon in-depth profiles on etching duratiion, measured with the in situ AES system.
(a) 3min, (b) 1min, (c) 15sec, (d) 5sec, (e) no etch

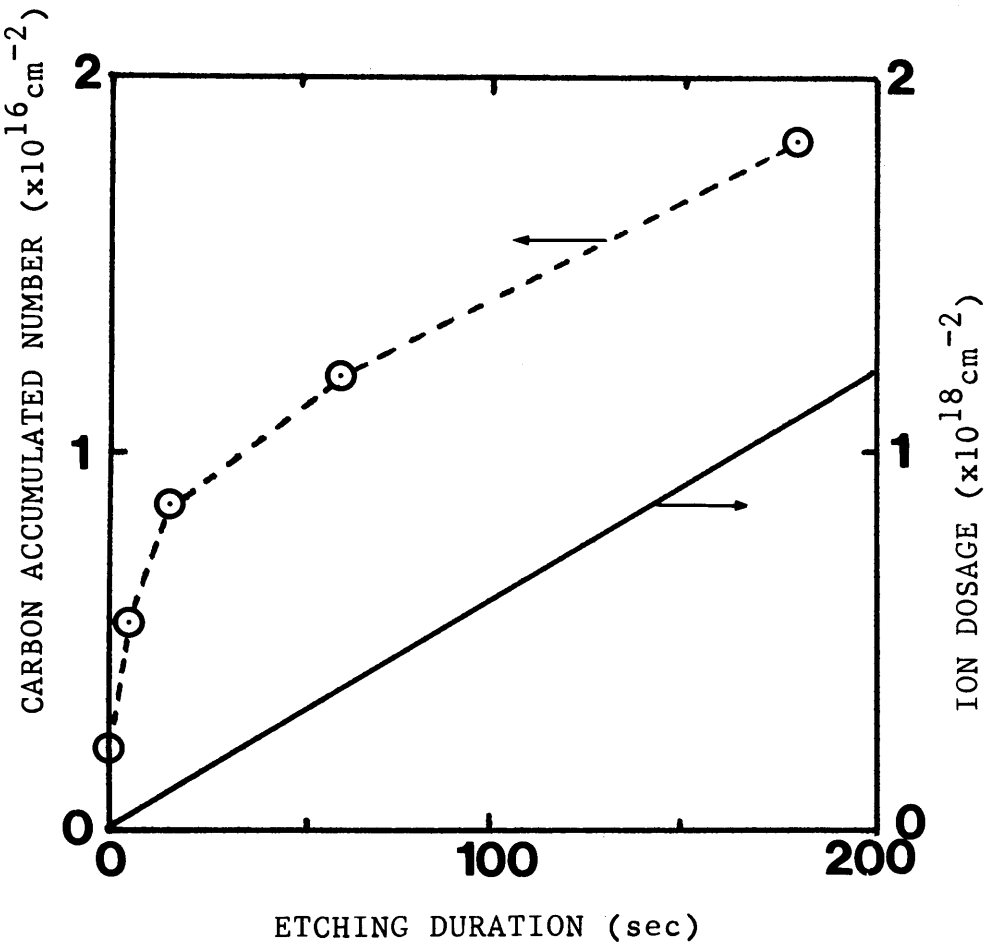

Fig. 3.18 The number of carbon accumulated on the RSE Si surface as a function of etching duration, which was derived from Fig. 3.17. Ion dosage was calculated from the effective plasma current.

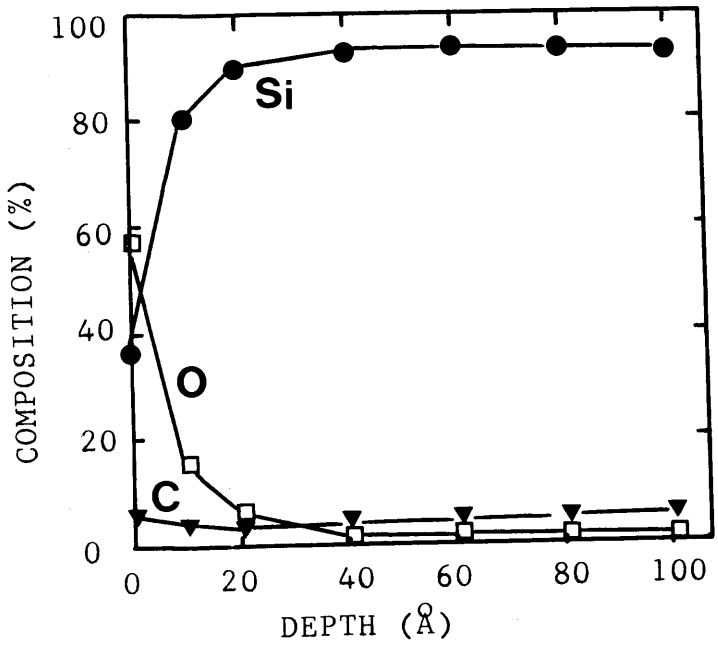

Fig. 3.19 AES in-depth profile of O_2 plasma ashed Si surface after RSE.
O_2 plasma ashing was performed for 10 min. at 0.5 Torr.

Chapter 4 Crystallographic Analysis of Reactive Sputter Etched Silicon Wafers with Transmission Electron Microscope *

4.1 Introduction

Dry etching for semiconductor device fabrication has been developed to realize fine line resolution, cleanliness, low-cost and process brevity. Reactive sputter etching (RSE), using RF sputtering configuration, is effective for the selective etching of Al and SiO2, while plasma etching is used to remove polycrystalline Si and Si3N4 films.

In particular, RSE utilizes bombardment effects of ions impinging vertically to the sample in addition to chemical reaction, so it is possible to realize fine pattern delineation without undercutting of various materials by selecting etching gases(4.1,2). However, after removal of filmes, substrates are subjected to radiation damage by ion bombardment during over-etching. The damaged layer on silicon substrates, caused by Ar ion bombardment at energy bellow 1 keV reportedly extend to the depth of 50-100A(4.3). In the case of RSE, CFx and CClx ions also impinge on the surface at several hundreds of eV, therefore surface damage may be formed. Damage is expected to consist of defects due to ion bombardment and contaminations due to decomposed etching gas, and might cause electrical characteristic deterioration. However, very few studies on surface damage caused by RSE have been reported.

In the present work, the surface damaged layer on slicon substrates caused by RSE overetching after removal of SiO2 films

*Most of this part has been reported in ref. (A.4) and (A.5).

has been investigated using transmission electron microscopy(TEM), reflection high energy electron diffraction (RHEED), oxidation Sirtl (OS) check and Auger electron spectroscopy(AES). Based on the obtained results, the recommended RSE conditions where no defects are formed on silicon substrates will be proposed.

In addition, the damage formation mechanism is discussed in terms of damage distribution determined by cross sectitonal TEM observation technique, and calculated ion distribution in silicon substrates.

As the application of damageless RSE technique, an in-depth crystallographic analysis method was developed using CBrF3 RSE and TEM observation step-by-step. Then, this method was applied to the oxygen-implanted Si substrates with 1.2×10^{18} cm^{-2} dose.

4.2 Experimental procedures

Two different diode RF sputter etching apparatuses were utilized in this study. One had a 100mm target at lower electrode (apparatus A) and the other had a 500mm target at upper electrode (apparatus B). Etching parameters in RSE were gas spieces (C2F6, CF4+H2 and Ar), RF power density, etching duration, gas pressure and target materials (carbon, teflon, quartz and iron). After O2 plasma ashing of RSE wafers, the RSE damage was investigated with transmission electron microscope(TEM) and oxidation Sirtl (OS) check.

Samples for TEM observation were prepared by RSE of silicon thin films, which were made by conventional thinning technique using HF+HNO3+CH3COOH solution, as shown in Fig. 4.1. Si wafers were (100) and (110) orientated p-type boron-doped wafers and (100) orientated n-pype phosphorous-doped wafers, which were used to investigate the gettering effects of the RSE damage by phosphorous.

An in-depth distribution of the RSE damage was observed by two sample preparation methods for TEM observation. One was the cross-sectional TEM observation. Samples were prepared by RSE of Si thin pieces set up normal to the target. The other was step-by-step thinning with TEM observation by chemical etching of the RSE Si thin pieces from the surface.

Furthermore, the dependence of the RSE damage on I-V characteristics of p-n junction diodes was measured.

4.3 Results and Discussion

(1) Defects caused by RSE

The dependence of surface damage structure on etching conditions, that is, power density, etching duration, C2F6 pressure and target materials, was investigated. The defects formed in RSE for long duration at high power density were found for the first time by TEM observation to be precipitates surrounded by elastic strain field. They existed on (111) planes along <011> directions taken from (100) direction, as shown in Fig. 4.2(a). These defects are formed on silicon substrates regardless of gas pressure and target materials. On the other hand, surface roughness pattern was formed under RSE conditions at lower power density, as shown in Fig. 2(b).

These experiments suggest that the damage structure depends especially on power density and etching duration. Then, the dependence of damage structure on these parameters was investigated by TEM at a C2F6 pressure of 0.04 Torr with a carbon target. The tendency of damage formation conditions is summarized as follows. (1) Precipitates surrounded by elastic strain field are formed with RSE for more than 1 minute at more than 1 W cm^{-2}. (2) No defects are observed within 15 seconds at 1 W cm^{-2} or within 5 minutes at 0.25W cm^{-2}. (3) Surface roughness pattern is formed under intermediate condition.

This defect proved to be intersitial type inclusion, because the image changed from bright to dark before and behind the defect along the direction of reciprocal lattice vector(4.4). Furthermore, it turned out to be converted into OSF(Oxidation

Stacking Faults) by annealing at 1100 C for 2 hours in wet O2. It should be noted that the region containing these defects is found to remain single crystalline from the selected area diffraction pattern.

When Ar was added to C2F6 in order to investigate the physical effect on surface damages, the surface destruction proceeded with increasing the Ar percent. In other words, ring patterns appear in addition to the single crystal silicon (100) pattern in selected area electron diffraction. These rings were found to be due to polycrystalline silicon and β-silicon carbide (zinc blende type). Polycrystallization of silicon substrate surface is enhanced with increasing Ar sputtering effects, while polycrystalline silicon was observed only by RHEED on the silicon surface etched with the pure C2F6. Therefore, the polycrystallization is thought to take place by ion bombardment effects. Since the momentum given to the surface by CFx ions could be consumed also for chemical reaction in C2F6 RSE, the ion bombardment effects would be reduced comparing with the case of Ar ion etching.

(2) Classification of RSE damages

When p-type Si substrates were reactive-sputter-etched using freon and Ar gases for long duration at high RF power density, interstitial type inclusions were formed on the surface regardless of etching apparatuses and gas spieces. They were accompanied with elastic strain field and lay on (111) planes with the density of about 5×10^{10} cm^{-2}. They are assigned to be stacking faults (SF) or dislocation loops. The surface was found to become uneven by ion impingiment from RHEED and TEM replica observation. Inclusions were also formed on the n-type Si substrates under the same RSE conditions as p-type Si. This result indicates that phosphoprous in Si has no gettering effects for RSE damage.

The most important parameters which control the damage formation proved to be not gas pressure and target materials etc., but power density and etching duration.
However, the classification of the damage with power density and etching duration depends on etching apparatus. Therefore, an attempt was made on classification of damage formation conditions with self-bias voltage and ion dosage as independent parameters on apparatuses. Self-bias voltage was measured by high-voltage probe (Tektronix P6015). Ion dosage was calculated using power density, self-bias voltage, ion current and etching duration. Figure 4.3 shows the classification of the damage formed in two etching apparatuses using self-bias voltage and ion dosage. The success of this classification indicates that the damage formation is determined by the amount of deposited

energy into Si lattices. RSE conditions should be decided from this diagram in order not to cause damages on Si wafers.

(3) In-depth damage distribution

Two analytical methods were attempted for observation of in-depth defect distribution. Figure 4.4 shows the preparation method for the cross-sectional TEM observation. Although this method is very primitive and the yield of getting successful samples was quite small, useful and reproducible data were taken. Figure 4.5(a) shows the cross-sectional TEM image of the sample reactive-sputter-etched at 0.9 kV and 1.3×10^{18} cm^{-2}. Inclusions, which were formed on the top of this sample by vertical ion bombardment, as shown schematically in Fig. 4.5(b), are distributed up to a depth of 1000 A. This result was confirmed by means of step-by-step thinning by chemical etching and TEM observation.

The region where inclusions were distributed seems much thicker than that expected from RSE energy. Figure 4.6 shows the calculated values of deposited energy against depth in a 2×10^{18} cm^{-2} CF_3 -implanted Si wafer at 0.8 kV bias voltage, which corresponds to 0.14 keV C and 0.22 keV F on the assumption that CF_3 is decomposed into C and F on the surface. Taking into account deposited energy due to C and F, single crystal in only about 30 A depth region is found to turn to an amorphous state, which is formed when more than 1.75×10^{24} eV cm^{-3} energy is deposited in a Si crystal. The depth is far shallower than the results of TEM observation.

In order to solve the discrepancy, the following speculaion about defect formation mechanism is considered. F is consumed to react with Si to form SiF_4, which volatilizes from the surface.

On the other hand, C is accumulated on the surface and knocked-on into deeper region by following ions. During RSE, recrystallization takes place in the surface region owing to much higher bombardment energy per unit volume than ion implantation. At the same time, Si interstitial atoms are emitted from the surface region by replacement of C atoms to Si lattice sites. Then Si interstitial atoms can diffuse into deeper region by radiation enhancement effects and contribute to inclusion formation.

(4) Influence of RSE damages on electrical characteristics

Finally, the influence of the RSE damages on I-V characteristics of p-n junction diodes was examined. The p-n junction in the present work was made using As ion implantation(100keV, 5×10^{5} cm^{-2}) into p-type Si wafer. The junction depth was 2500 A,as shown in Fig.4.7. The As-implantation defects were analysed using TEM in order to distinguish them from the RSE damages. Figure 4.8 shows a TEM image of As-implanted Si wafer annealed at 900 C for 30 minutes in N2. Dislocation loops were observed with the density of about 3×10^{10} cm^{-2}. These defects are confirmed not to influence I-V characteristics on p-n diodes.

Through-hole etching of phosphorous silicate glass on the p-n junction was carried out using RSE or wet etching, and the difference between them in I-V characteristics was examined. I-V reverse current of p-n diodes made using RSE was 10^{-11} A for reverse voltage of 10 V, that means no remarkable damages were caused compared with the wet etching. It can be said that the RSE damage hardly relates to I-V characteristics of p-n diodes, although it may influence other electrical characteristics such as surface state density and deep levels.

4.4 Application of RSE technology to TEM in-depth analysis

A buried SiO2 layer structure formed by oxygen-ion implantation (4.5) and an epitaxial layer on the substrate is considered as an alternative for SOI (Silicon on Insulator) structure such as SOS (Silicon on Sapphire). In this section, the in-depth crystallographic analysis of oxygen implanted layer using RSE thinning technique and TEM observation was carried out. Samples were oxygen ion implanted p-type silicon wafer with a resistivity of 10^{3} Ωcm. The ion energy was 150 keV, and the dose was 1.2×10^{18} cm^{-2}. Annealing was performed in N2 at 1150 C for 2 hours. To observe the depth distribution of defects in the surface silicon layer, RSE by CBrF3 plasma was used for sample thinning. The sequence of the experiment is shown in Fig. 4.9. The surface silicon layer was removed from the substrate by 50 % HF etching. The samples were put on micro-grids for TEM viewing, and were etched step-by-step with RSE to remove any heavily-defective region preventing a less defective region from being observed. Then, the crystalline structure was observed by TEM.

First, we tried RSE of Si using CBrF3 gas in order to etch the Si wafer. Fig.4.10 shows the etching rate of Si substrates at CBrF3 pressure of 0.1 Torr and 30 W applied power. Under this condition, no defects were found to be formed on Si substrates. As shown in Fig. 4.10, linear etching characteristics was obtained. The fact that the straight line does not cross at zero may be attributed to the slow initial etching rate due to surface oxide layer of contaminations.

Figure 4.11 shows electron micrographs and corresponding electron diffraction patterns for in-depth crystallographic analysis of the surface silicon layer of the substrate with 1.2×10^{18} cm^{-2} oxygen dose. The thickness of the surface silicon layer is about 2500A. Since the as-removed surface silicon layer contains a polycrystalline silicon layer near the buried SiO2 layer, it is impossible to observe the crystallinity in a single crystalline layer. After 65 nm etching by RSE from the side of the interface between the buried SiO2 and the surface silicon layer, no ring patterns are observed, which indicates that only a single crystalline silicon layer remains. However, a high density of dislocations can be observed in the micrograph. After 130 nm etching, all dislocations in the micrograph disappear, and only branch-like patters are observed. These branch-like patterns are diffraction contrast caused by the roughness of a sample surface which probably reflects the shape of the interface between the single crystalline and polycrystalline layers. The patterns did not change for samples etched to 180 nm or more. Thus, the region near the surface is found to consist of dislocation-free single crystalline silicon.

This defect distribution can be explained by the oxygen concentration distribution. Figure 4.12 shows an AES oxygen depth profile for 1.2×10^{18} cm^{-2} oxygen implanted and annealed silicon layer with the defect distribution. The polycrystalline region contains 1 to 3×10^{22} cm^{-3} oxygen atoms. Such a high concentration of oxygen prevents recrystallization epitaxially from the surface region, which remains single crystalline in the as-implanted

state. In the depth range of 100 to 200 nm from the surface, 0.5 to 2.5×10^{21} cm^{-3} oxygen atoms exist. This high concentration results in the formation of large precipitates which contribute to the formation of the crystalline defects shown in Fig. 4.12(b). Although no dislocations are observed in the surface region (<100 nm), oxygen atoms of concentration about 10^{19} cm^{-3} exist at the skirt of the implanted oxygen distribution. This value far exceeds that soluble in silicon. So, these excess oxygen atoms are expected to form small precipitates. However, owing to the branch-like patterns, such precipitates cannot be observed in Fig. 4.12(c).

4.5 Conclusion

The dependence of the RSE damage on etching conditions and the damage formation mechanism have been investigated using TEM. The etching conditions under which the RSE damage, namely, inclusions accompanied with elastic strain field and surface roughness pattern, was formed can be classified with only self bias voltage and ion dosage regardless of etching apparatuses and other etching conditions.

The degree of surface damage is enhanced by the addition of Ar gas to C2F6 because of increasing ions' momentum, while it does not change by adding C2H4 or O2 to C2F6.

Cross-sectional TEM observation showed that inclusions were distributed more than 1000 A depth from the surface. This result implies the diffusion of Si interstitial atoms by radiation enhancement effects.

The RSE damage hardly relates to I-V characteristics of p-n diodes.

In addition, the in-depth TEM observation technique was developed using CBrF3 RSE and TEM step-by-step in order to investigate the crystallographic distribution of the Si substrate with a buried SiO2 layer formed by oxygen-ion implantation. For a 1.2×10^{18} cm^{-2} dose substrate, the surface Si layer was found to consist of three regions from the surface, namely, a dislocation-free single crystalline Si region, a defective region with high density dislocations and a polycrystalline Si region near the buried SiO2 layer. These crystallographic properties are related to the oxygen concentration.

References for Chapter 4

4.1) H. W. Lehmann and R. Widmer, J. Vac. Sci. and Technol. 15(1978) 327.

4.2) J. W. Coburn and H. F. Winters, J. Vac. Sci. and Technol. 15(1978) 327.

4.3) H. R. Deppe, B. Hasler and J. Hopfner, Solid-State Electro. 20(1977) 51.

4.4) P. B. Hirsch, A. Howie, R. B. Nicholson, D. W. Pashle and M. J. Whelan "Electron Microscopy of Thin Crystals" (Butterworths, London, 1971) Chapter 14.

4.5) K. Izumi, M. Doken and H. Ariyoshi, Electron. Lett. 14(1978) 593.

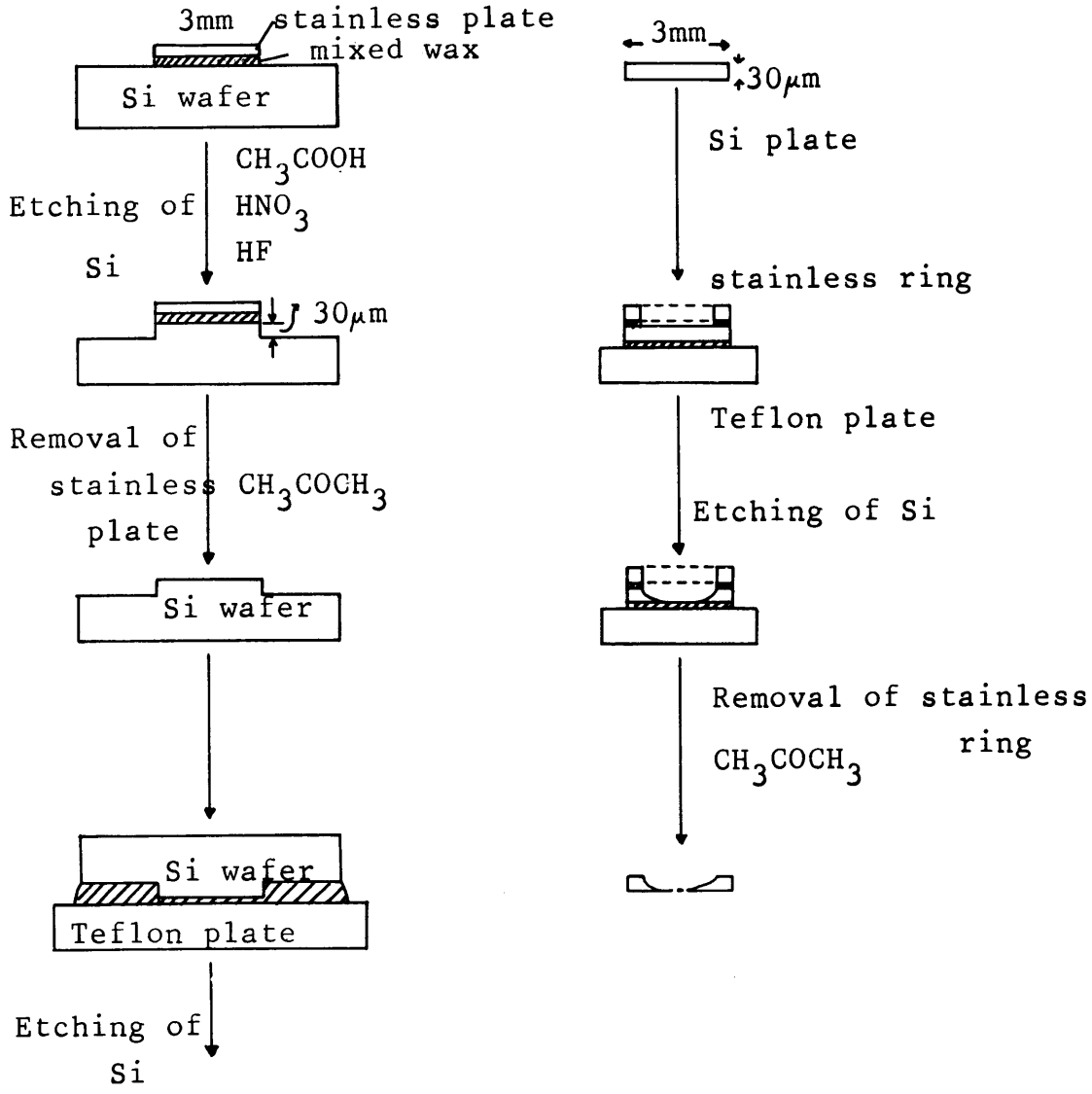

Fig. 4. 1 Sample preparation method for Transmission Electron Microscope.

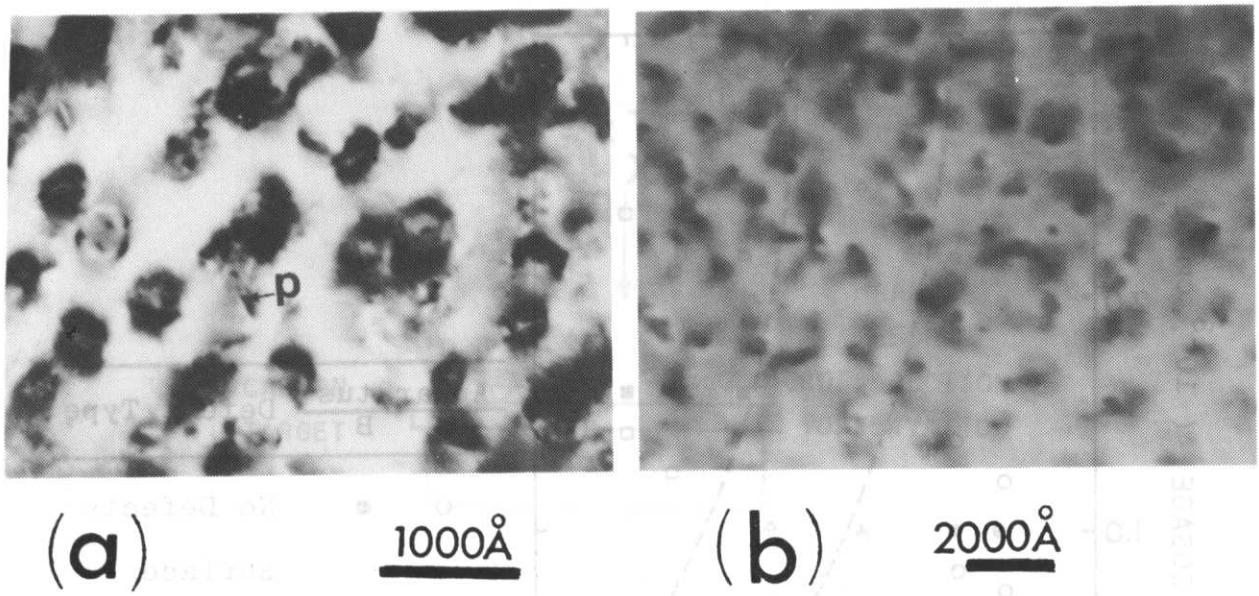

Fig.4.2 TEM bright field images of (100) silicon films:(a) Precipitates surrounded by elastic strain field, RSE for 3 minutes at 1 W cm^{-2}. P shows a precipitate. (b) Surface roughness pattern, RSE for 3 minutes at 0.6 W cm^{-2}.

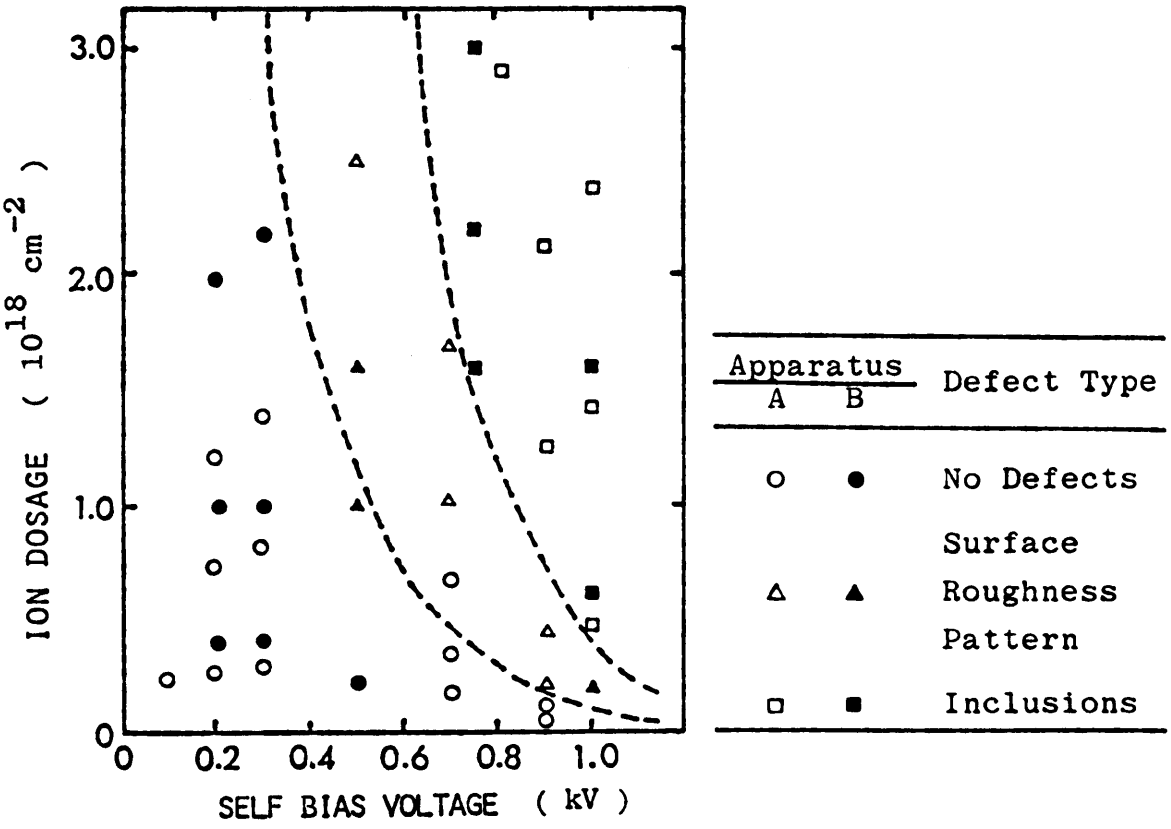

Fig.4.3 Dependence of the RSE damage on self bias voltage and ion dosage.

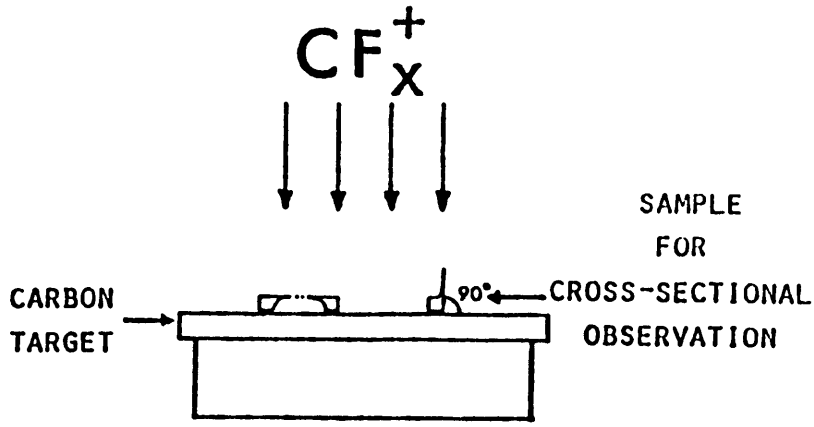

Fig.4.4 Schematic diagram of sample preparation method for TEM observation.

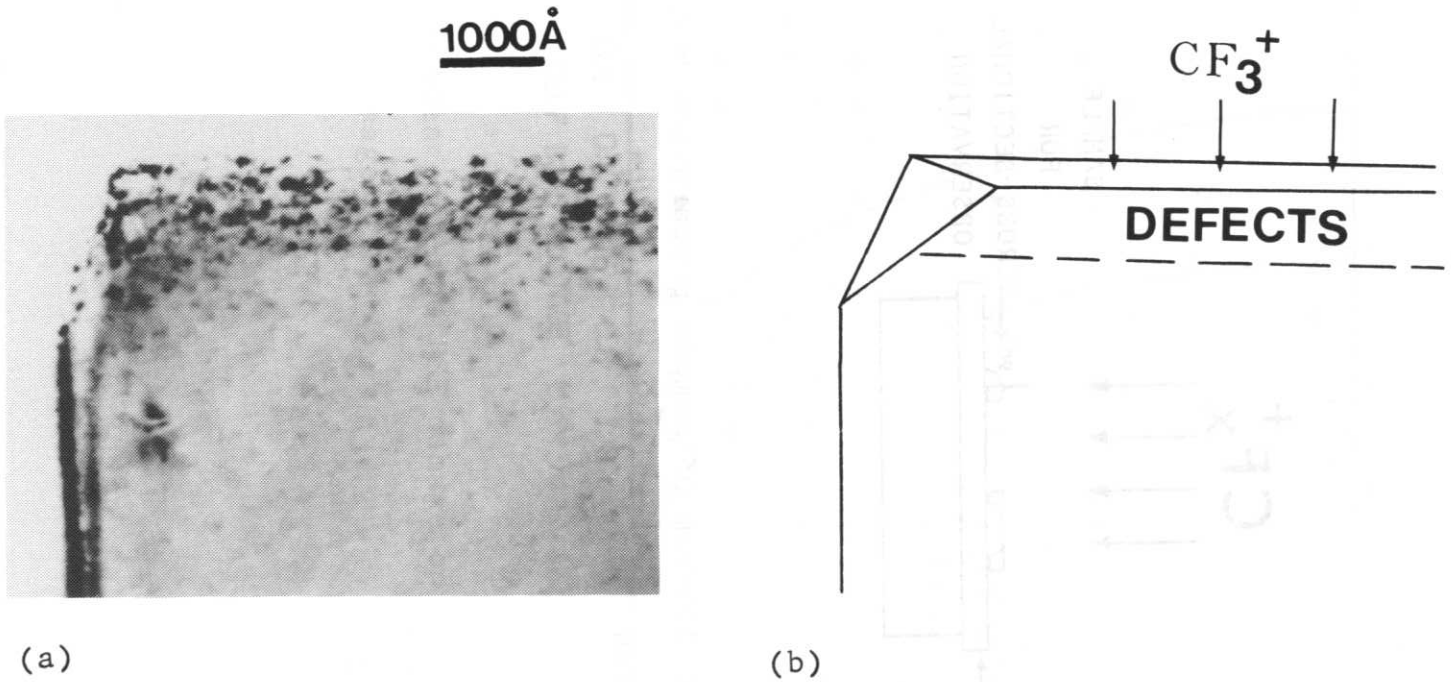

Fig.4.5 Cross-sectional TEM images of the RSE damage. (a) In-depth distribution of inclusions. (b) Schematic diagram.

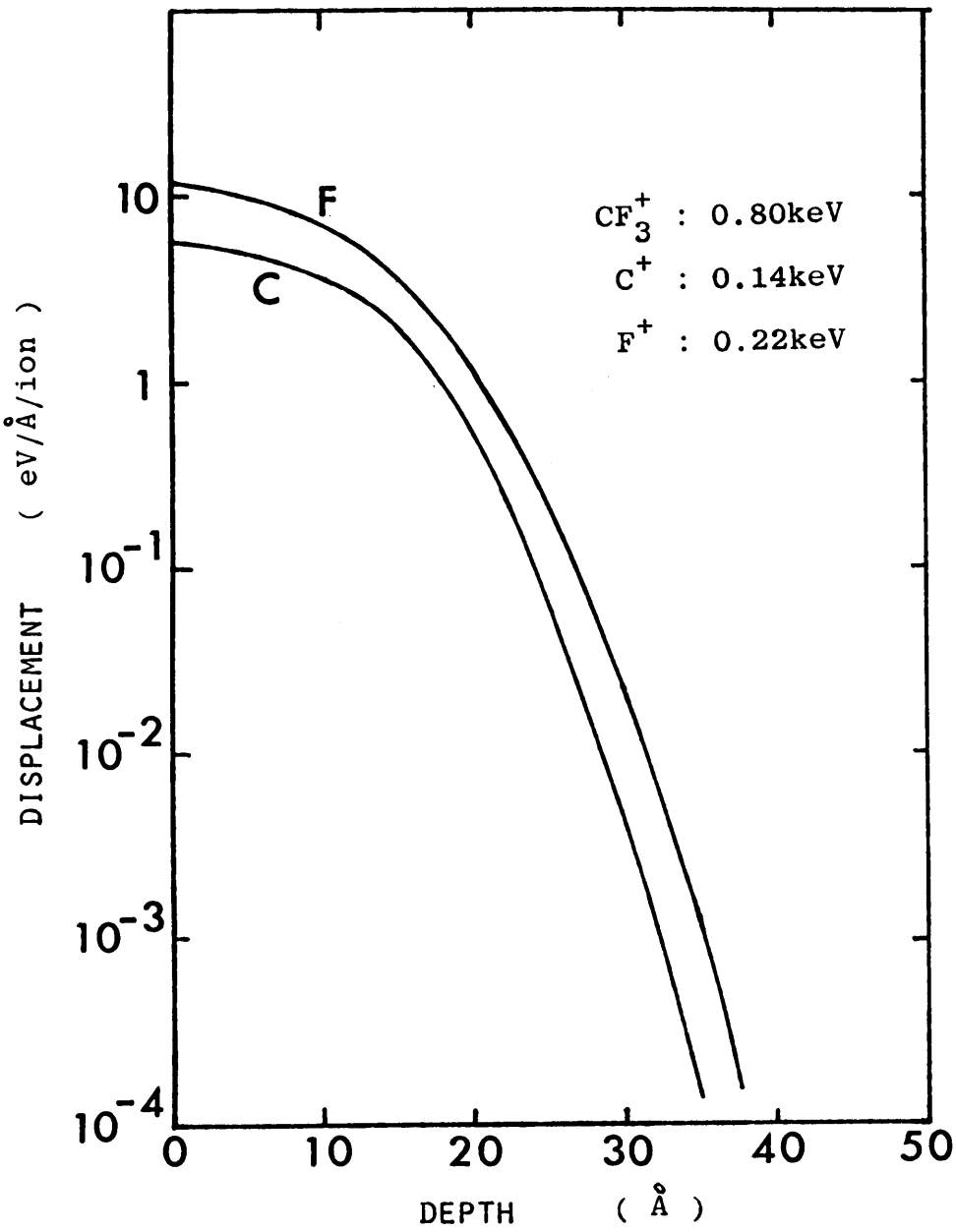

Fig. 4.6 Calculated values of deposited energy in a 2×10^{18} cm^{-2} CF_3^+ implanted Si wafer at 0.8keV, which corresponds to 0.14keV C and 0.22keV F.

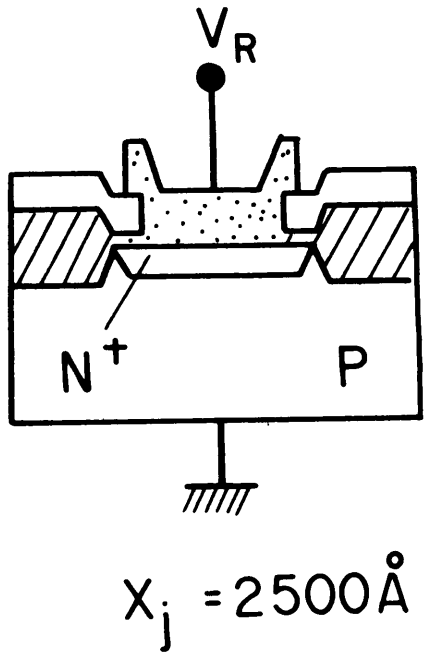

Fig.4.7 Sample structure for p-n diode characteristics measurement.

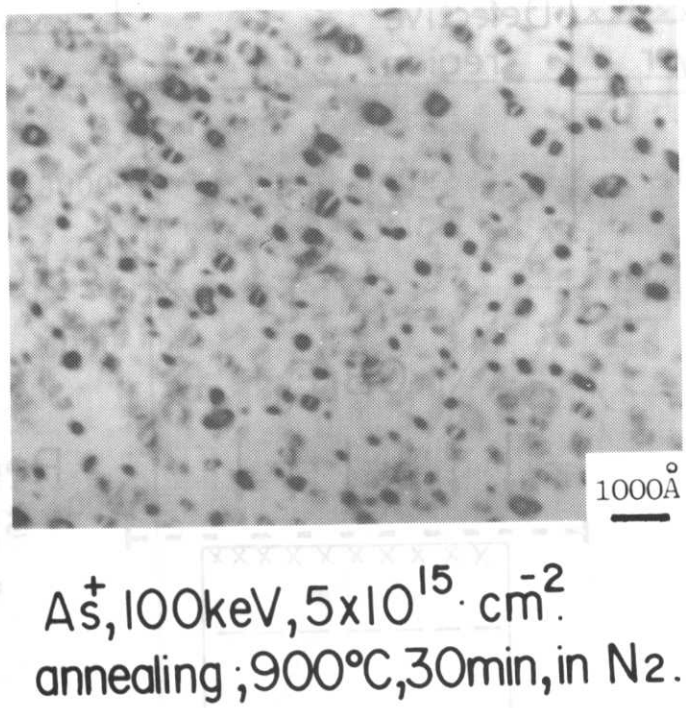

Fig.4.8 TEM image of As^+ ion implanted ($100keV, 5\times10^{15}\ cm^{-2}$) Si wafer annealed at 900 C for 30 min. in N2.

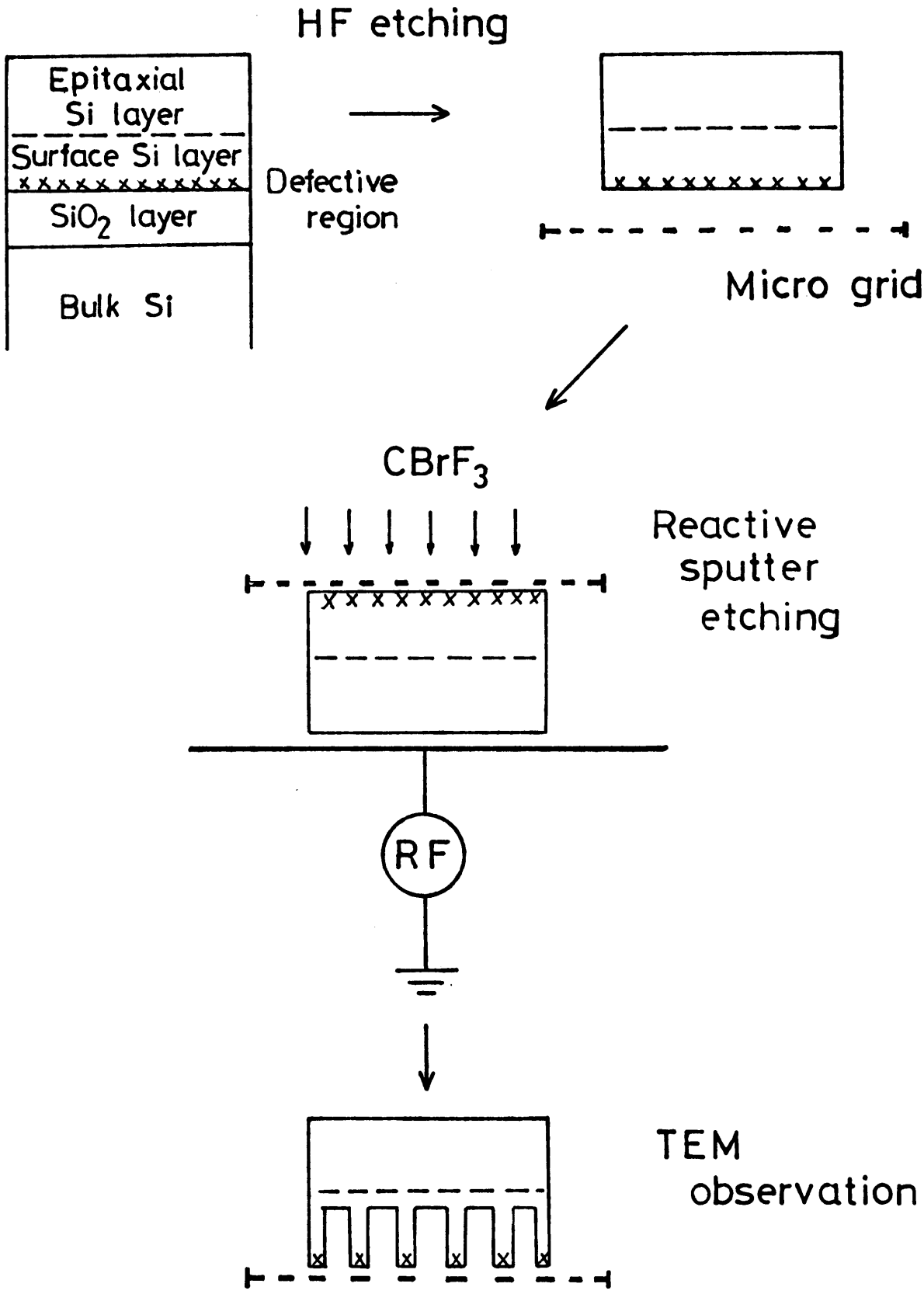

Fig.4.9 In-depth crystallographic analytical method using RSE.

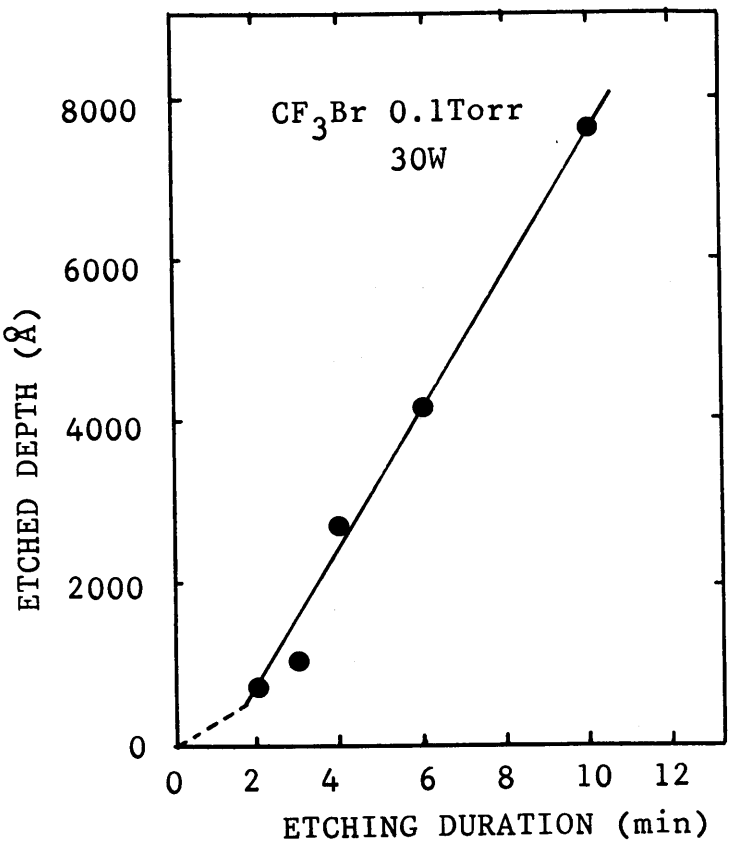

Fig.4.10 Etching characteristics of Si (100) substrate by CBrF3 RSE. Pressure; 0.1 Torr, Applied power; 30W.

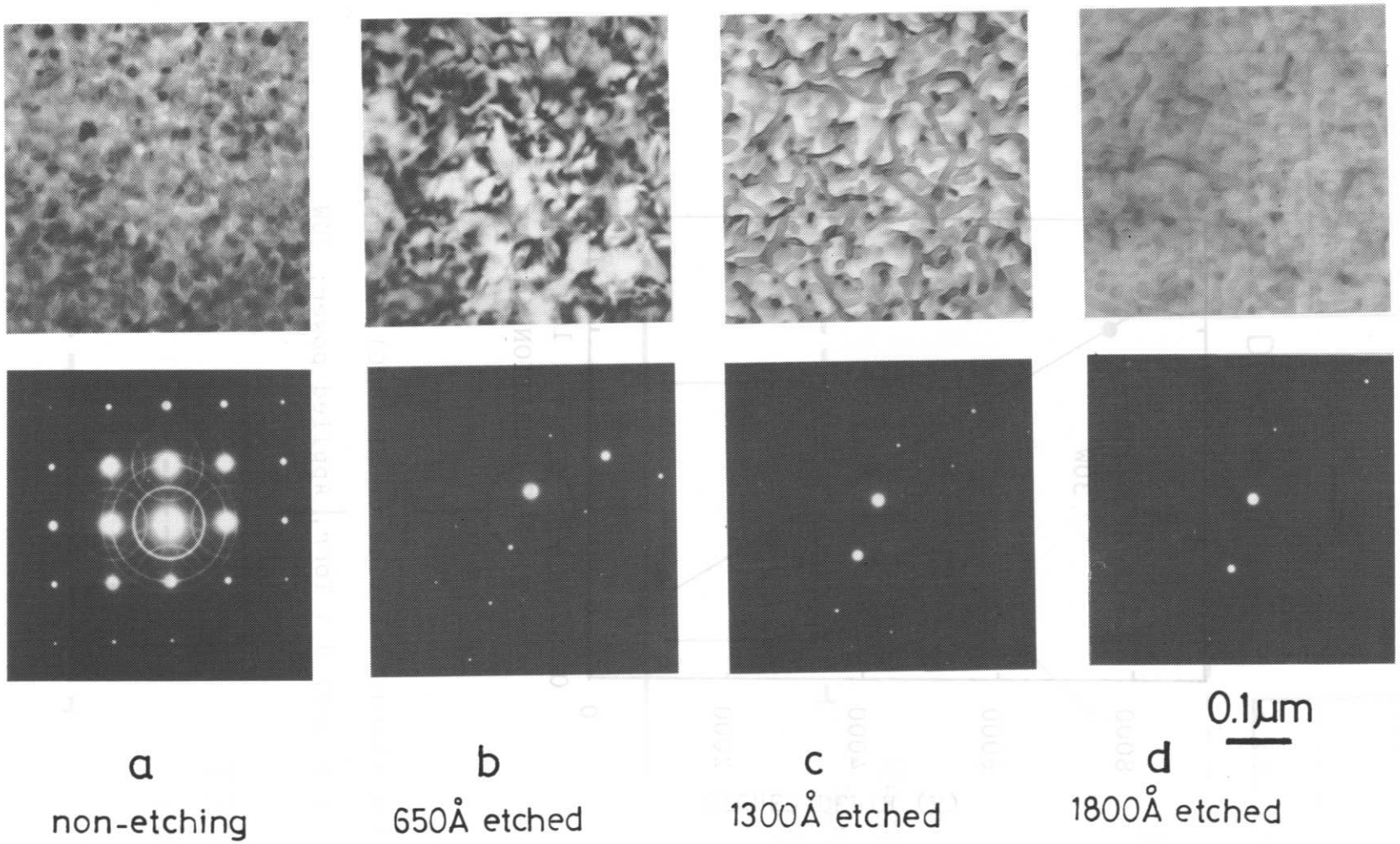

Fig.4.11 Transmission electron micrographs and corresponding diffraction patterns for in-depth crystallographic analysis of a surface silicon layer of 1.2×10^{18} /cm^2 oxygen implanted and annealed substrate.

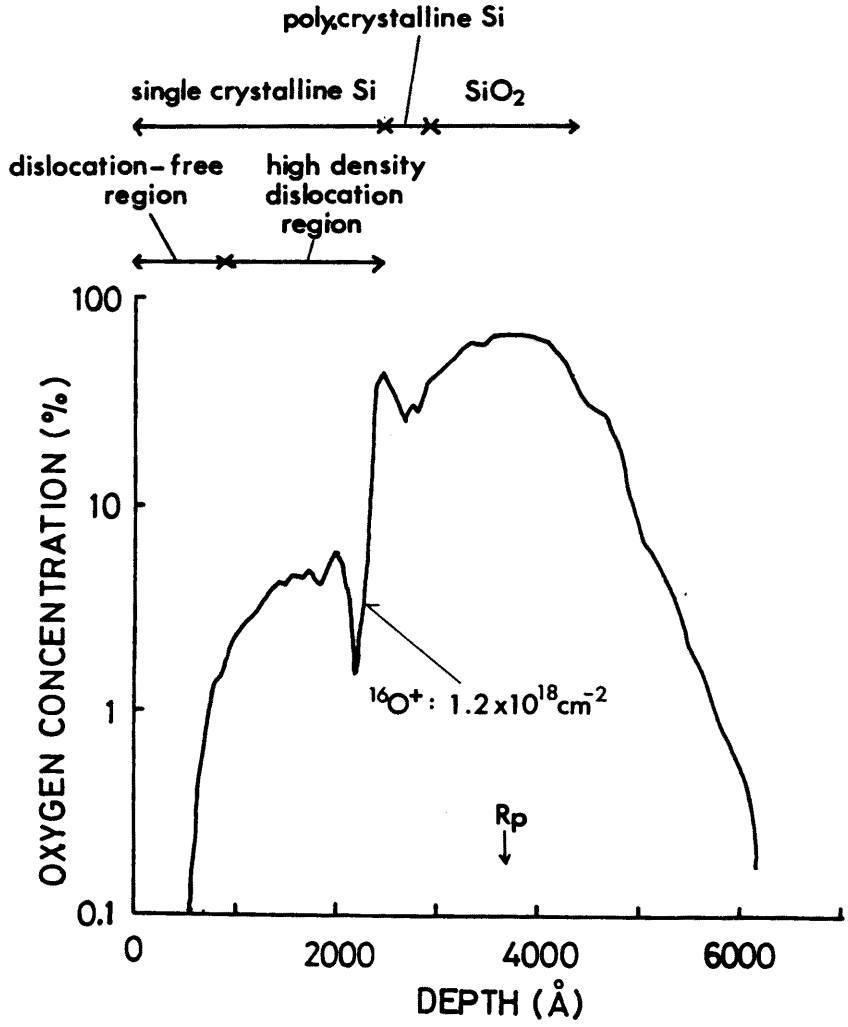

Fig. 4.12 AES depth profile for $1.2 \times 10^{18} cm^{-2}$ oxygen implanted and annealed silicon layer with crystallinity distribution.

Chapter 5 Quantitative Analysis of Impurities in Semiconductors with Secondary Ion Mass Spectrometry*

5.1 Introduction

The Secondary Ion Mass Spectrometry (SIMS) is an analytical technique having characteristics of both surface sensitive analysis such as AES and XPS, and bulk analysis such as Atomic Absorption Spectrometry and Spark Source Mass Spectrometry. This technique has been used for impurity trace analysis of semiconductors because of the high sensitivity in order to analyse impurity distribution in ion-implanted Si and GaAs.

However, the mechanism of generating secondary ions is extremely complicated, and the secondary ion intensity is affected by numerous factors, for example matrix effect, primary ion species, primary ion current, accelerated energy, pressure in the analytical chamber, etc.

Although there have been numerous attempts to understand the relationship between the secondary ion intensity (I) and an elemental content (C) for quantification, the LTE (Local Thermal Equilibrium) model proposed by Andersen and Hinthorne (5.1) is presumably the most successful of these attempts.

In this chapter, the first attempt was made to analyse the impurity concentration in GaAs and InGaAs using this model and the validity was checked. Then, the new method to determine the impurity concentration in a single element material such as silicon was developed on the basis of the simplified LTE model. This method does not require two plasma parameters, namely

*Most of this part has been reported in ref. (A.6), (A.7) and (A.8).

electron density (Ne) and electron temperature (Te) to determine the ionization yield, which make the concentration calculation very complicated.

Furthermore, secondary ion emission process is discussed in cases of both O_2^+ and Ar^+ primary beams. Then, the influence on the detection limit is discussed in terms of (1) the base pressure in the analytical chamber, (2) contamination surrounding the sample , so-called memory effect.

5.2 Theoretical considerations

(1) LTE (Local Thermal Equilibrium) model

When the primary ions bombard the sample surface, sputtering of the bombarded region takes place and ejected atoms are partly ionized. The mixture of ions and neutrals are regarded as a plasma. Since SIMS is an instrument to detect only ions from the surface plasma, we have to determine the ionization yield of the plasma in order to calculate the concentration of elements in the sample.

For the sake of simplicity of the calculation, we introduce a hypothesis as follows : This plasma can be regarded as an LTE plasma. The ionization equilibrium in the LTE plasma is expressed by Saha-Eggert equation.

$$\frac{N^+ N_e}{N^o} = \left(\frac{2\pi m_e kT}{h^2}\right)^{3/2} \frac{B^+ B_e}{B^o} \exp(-E/kT) \qquad (5.1)$$

Here, N^o, N^+ and Ne, respectively are the number per unit volume of neutrals, positive ions and electrons, h is Planck's constant, k is Boltzmann's constant, T is absolute temperature, m is mass number, B is partition function, and E is dissociation energy.

Eq.(5.1) can be written as follows:

$$N^+/N^o = f(Ne,T) \qquad (5.2)$$

The relationship between secondary ion intensity(I) obtained by SIMS and N^+ in the surface plasma is given by

$$N^+ = a\sqrt{m}I \qquad (5.3)$$

because the detection yield of ion detector is almost proportional to $1/\sqrt{m}$. Here, a is a constant.

For the element i in the sample, the concentration Ci is expressed by

$$Ci=\frac{N_i^o+N_i^+}{\sum_j (N_j^o+N_j^+)} \qquad (5.4)$$

Therefore, Ci changes with Ne and T. If we have more than two elements with known concentrations, we can determine Ne and T by making the calculated C1' and C2' equal to the real C1 and C2, where C1' and C2' can be determined by eq.(5.4) with suitable Ne and T.

The calculation is done by means of a least square method with the following function.

$$F(Ne,T)=\sum_k \left|(Ci^k-Ci)/Ci\right|^2 \qquad (5.5)$$

where Ci^k is known concentration and Ci is the calculated one by eq.(5.4). Since the dissociation energy:E is expressed by

$$E=U-\Delta E \qquad (5.6)$$

U;ionization potential

ΔE;energy depletion by Coulomb interaction

$$=2.95\times10^{-8}\times1.2\times(Ne/T)^{1/2},$$

eq.(5.5) can be rewritten as follows:

$$F'(T,\Delta E)=\sum_k \left|(Ci^k-Ci)/Ci\right|^2 \qquad (5.7)$$

which is a function of T and ΔE.

First of all, contour lines of $F'(T,\Delta E)$ was drawn in the case of low alloy steel sample. As shown in Fig.5.1, many minimum points exist. If the plasma produced by the ion beam bombardment is the LTE plasma, only one set of T and ΔE should be obtained which express the plasma state. However, the plasma on the sample surface is multi-peak type. This is the first problem in this

analytical method.

In this work, the point with the smallest F' value among these minimum points was regarded as the true set of T and ΔE, namely T and Ne for the convenience. Figure 5.2 shows the analysed result of an Fe-Cr alloy (NBS 838 steel). Although the calculated values of low concentration elements show slightly large ones compared to the known values, this analytical method was found to be useful for SIMS quantification.

(2) A simplified analytical method

In the analytical method based on the LTE plasma model, more than two internal standard elements are required to determine Ne and T. Furthermore, complicated minimization technique should be employed and it is not easy to find the true minimum value because of many minimum points.

So, the simplification of calculation process has been attempted to diminish the calculation time and to apply this technique to single element materials such as silicon. In the case of impurity A in matrix B, two formula of Saha-Eggert equation are given using eq.(5.1). In these equations, Ne,T and E are common. Therefore, if we make a ratio of N^+/N^o of element A to that of element B, a very simple equation is obtained as follows:

$$\frac{(N^+/N^o)_A}{(N^+/N^o)_B} = \frac{(B^+/B^o)_A}{(B^+/B^o)_B} \exp\left(-\frac{E_A - E_B}{kT}\right) \qquad (5.8)$$

The ratio of concentration of element A (C_A) to C_B is given by eq.(5.9), if N^+ is assumed to be negligibly small compared to N^o.

$$C_A/C_B = \frac{\sqrt{m_A}}{\sqrt{m_B}} \times \frac{I_A}{I_B} \times \frac{(B^+/B^o)_A}{(B^+/B^o)_B} \exp\left(-\frac{E_A - E_B}{kT}\right) \qquad (5.9)$$

This equation contains only one parameter, that is T. Therefore, if T is determined by using a standard sample with two elements of known concentration, other impurity concentration can be calculated by means of eq.(5.9). For example, in the case of silicon, it is very easy to get Si wafers with As or B impurity

of known concentration to determine T. Then, other impurities such as Na can be analysed.

This procedure was applied to the quantitative analysis of $In_{0.1}Ga_{0.9}As$ (C_{In} =0.05) to check procedure validity. Ga and As were chosen as internel standard elements to determine electron temperature from eq.(5.9) and In concentration calculation was performed. The results are summarized in Table 5.1. It should be noted that the T with O_2^+ beam was higher than that with Ar^+ beam at high accelerating voltage, while both T's were about the same at 3 kV accelerating voltage. The In concentration shows a good agreement with the value measured by EPMA.

5.3 Experimental procedures

The experiments were carried out using Hitachi IMA-2 with Ar^+ and O_2^+ primary beams of 3 to 10 keV and 1μA, and CAMECA IMS-3f with O_2^+ and Cs^+ primary beams of 15 keV and 10 keV, respectively. Sample stages were biased at 2.9 to 3.0 kV for IMA-2 and 4.53 kV for IMS-3f to enhance the emission yield of secondary ions. The base pressures of the sample chambers were $1x10^{-7}$ Torr and $4x10^{-9}$ Torr for IMA-2 and IMS-3f, respectively, so the former was used for quantitative analysis for bulk and the latter was for in-depth analysis with high depth resolution and ultra-trace analysis.

Cs^+ ion beam was employed to enhance the negative ion yield of elements with large electronegativity. In this experiment, the stability (coefficient of variance) of the beam intensity was 1-2 % in 10 minutes.

For standard samples, Emission Spectrometer was used to determine impurity concentration in Si-doped GaAs substrates. The calibration curve was obtained using G-Standard samples of Spex Co.(G1 to G4). Graphite powder was mixed with the GaAs samples and G-standard to stabilize the discharge, and 10 % Y_2O_3 powder was added as an internal standard for calibration. In the present work, the Yttrium emission line intensity had less than 20 % variation. The experimental parameters of emission spectroscopy are listed in Table 5.2.

In addition, $In_{0.1}Ga_{0.9}As$, Si, SiO_2 and PSG films were used for the simplified LTE plasma model calculation. In the case of bulk analysis, the measurement was carried out after sputtering

for more than 10 minutes. The electron gun was used in analyzing SiO2 and PSG with 0.8 kV accelerating voltage in order to prevent the charging effect and ion-induced mobilization effect (5.2) in the sample. Absorbance measurement in spectrophotometry was made on Shimazu Multiconvertible Spectrophotometer Double-40S. Determination of Na concentration in SiO2 films was performed using the Perkin-Elmer model 460 Atomic Absorption Spectrophotometer with a flameless atomizer.

For in-depth analysis and background evaluation, ion-implanted Si and GaAs substrates were used. Dopant elements were oxygen, silicon and arsenic.

5.4 Experimental results

(1) Impurity analysis in GaAs and InGaAs based on the LTE plasma model

For quantitative bulk analysis, three GaAs substrates doped with different content of Si were prepared and analyzed by the emission spectrometer to determine the Si concentration.

From spectral line intensities projected on photo-plates, the density of lines was calculated using

$$D=\log(Io/I) \qquad (5.10)$$

where Io is the intensity in the unexposed region measured by micro-photometer , and I is that in the region of spectral line. Intensity calibration by Yttrium line was performed using the following equation;

$$D'=D\cdot Dy^{std}/Dy \qquad (5.11)$$

where Dy^{std} is Yttrium density in the G-standard sample, and Dy is that in the sample.

Figure 5.3 shows the calibration curve of Si in GaAs measured by emission spectrometer. In the present work, only Si concentration was determined because other element concentration was less than the minimum value(1ppm) of G-standard samples. The results obtained from Fig.5.3 were multiplied 10 times(dilution ratio) and listed up in Table 5.3 in comparison with carrier concentration and the values calculated by means of the LTE plasma model. It is found that $O2^+$ primary beam can provide closer results to the emission spectroscopic data than Ar^+ beam in the LTE model calculation, which is probably because $O2^+$ beam is likely to produce surface ionization by chemical process. The

chemical process might be closer to the LTE plasma than the kinetic process of Ar^+ beam case. In addition, in low-Si content samples, Si dopants in GaAs matrices were found not to be fully activated, because the carrier concentration was slightly smaller than Si concentration. Some deep acceptors such as residual carbon may exist in the GaAs to compensate the Si donor.

Table 5.4 shows impurity concentration in S-16, S-17 and S-18 samples calculated on the basis of the LTE plasma model using $O2^+$ primary beam. Besides Si impurity, there are many elements, and Fe is the next impurity whose content is about 10 to 40 ppma. The existence of this impurity was qualitatively confirmed by the emission spectrometry. So, Fe might be the compensator for dopant Si atoms.

This LTE plasma model calculation was also applied to $In_xGa_{1-x}As$ epitaxially grown on GaAs substrates In this case, impurity analysis is impossible by bulk analytical technique such as emission spectrometry or atomic absorption spectophotometry. In other words, SIMS is only one possibility for trace analysis of thin films. Table 5.5 shows impurity concentrations in the epitaxial film and substrate. In this calculation, In, Ga and As were used as internal standard elements. It is found that Na, K and Ca contents in the epitaxial film are larger than those of the substrate. They might be contamination in the course of film growth.

(2) Determination of Na concentration in Si and SiO2 on the basis of the simplified LTE model

Recently, Na contamination has been reported to be one of the most important problems in the fabrication of LSI devices, because Na atoms or ions are very mobile in the SiO2 gate oxide and cause the fluctuation of C-V characteristics. Although the in-depth analysis of Na in SiO2 films has been performed using radio-activation analysis to find suitable treatment process to decrease Na contamination, this method is not easy, and has poor depth resolution. On the contrary, SIMS has the best sensitivity for Na because Na has very small ionization potential. Therefore, the Na detection limit of around 1 ppba can be expected.

Here, the simplified LTE plasma model whose validity was checked for InGaAs was applied for the quantification of Na in Si. A method was adopted involving measuring I_{Na}/I_{Si} from unknown samples after determining T from the reference sample, which involves two elements, such as Si and As, assuming that the T in unknown samples is the same as that in As-doped Si.

Electron temperatures are plotted in Fig.5.4 as a function of As concentration under three SIMS conditions, namely (1) Ar^+ primary beam at 2×10^{-7} Torr, (2) Ar^+ primary beam with O2 admission of 1×10^{-5} Torr, and (3) $O2^+$ primary beam at 2×10^{-7} Torr. From these results, the effect of oxygen proved to be electron temperature increase.

Next, an attempt was made to determine Na concentration in Si. In the case of Si, $(B^+/B^+O)Na/(B^+/B^+O)Si$ is almost equal to 0.8(5.3) in the temperature region of 3000 K to 7000 K. Therefore

C_{Na} is given by the following equation.

$$C_{Na} = \frac{I_{Na}}{I_{Si}} \times \frac{\sqrt{m_{Na}}}{\sqrt{m_{Si}}} \times 0.8 \exp\left(-\frac{E_{Na} - E_{Si}}{kT}\right) \qquad (5.12)$$

This procedure was checked with a Si wafer, whose C_{Na} was measured to be 4.3 ppba by activation analysis beforehand. The C_{Na} calculated by eq.(5.12) was about 8 ppba. Since the Na peak S/N ratio was about 5 in this case, the Na detection limit with SIMS proved to be about 1 ppba. Taking into account errors due to (I_{Na}/I_{Si}) measurement and temperature determination, the result is considered to be comparatively in good agreement with 4.3 ppba.

Figure 5.5 shows C_{Na} frequency of occurrence on the surface (about 50 A thickness) of a cleaned wafer (sample 1) and a contaminated one (sample 2). The large amount of scatter in measured values in sample 1 is attributed to the relatively large contamination during measurement. C_{Na} in the surface region can be reduced close to the bulk concentration (4.3 ppba) by means of an appropriate clean-up procedure. In this work, the RCA clean-up procedure(5.4) was adopted at the last cleaning step.

In order to caluculate impurity concentration in SiO2, determination of electron temperature by I_{Si}, I_{SiO}, and I_{O} was attempted using PSG films as standard samples. The P concentration in PSG films was determined by conventional spectrophotometry and was checked by activation analysis. Since I_{SiO} cannot be neglected compared with I_{O} for SiO2, electron temperature determination was carried out by the following

equation.

$$\frac{C_O}{C_{Si}} = \frac{N_O + N_{SiO}}{N_{Si} + N_{SiO}} \times \frac{X(O) + X(SiO)}{X(Si) + X(SiO)} \qquad (5.13)$$

$$X(M) = \sqrt{m_M}\, I_M / (B_M^+ / B_O)M / \exp(-E_M / kT).$$

Here, $(B_M^+ / B_O)SiO$, which cannot be found in literatures, is assumed to be equal to $(B_M^+ / B_O)Si$. The average electron temperature for Ar^+ beam was about 8630 K. Then, P concentration was calculated using this temperature by

$$C_P = C_O \times \frac{X(P)+X(PO)}{X(O)+X(PO)} \qquad (5.14)$$

and plotted in Fig. 5.6. The results were in good agreement with chemically analyzed values.

Then, the procedure was applied to the quantitative analysis of Na in SiO2. The results of electron temperature and Na concentration in borosilicate glass (BSG) are listed in Table 5.6. Higher temperature than that in PSG might be due to high Na concentration in BSG. The main reason why C_{Na}, determined with SIMS is about an order of magnitude lower than chemically analyzed value is due to the high ionization yield of Na because of high electron temperature. When the ratio of first ionized particle density to neutral particle density for Na cannot be neglected compared with 1, C_{Na} should be multiplied $(1+\alpha)$ times, where α is N_M^+ / N_O. Therefore, eq.(5.9) should be substituted for

$$\frac{C_{Na}}{C_{Si}} = (1+\alpha) \times \frac{X(Na)}{X(Si)} \qquad (5.15)$$

Since T is higher than 8000 K in the case of SiO2, $(1+\alpha)$ might be much larger than 1.0. In order to obtain the exact $(1+\alpha)$ value, electron density determination was performed using the conventional LTE model calculation. Ne for SiO2 proved to be about 1.3×10^{19} cm^{-3}. The C_{Na} corrected with the $(1+\alpha)$ term is comparatively in agreement with chemically analyzed value.

Next, quantitative analysis of Na in three kinds of high purity quartz glass which are used as a quartz tube in a diffusion furnace was carried out. C_{Na} in glasses were 0.62, 1.1, and 1.2 ppma from chemical analysis. In this case, the electron temperature was about 10000 K. SIMS values of C_{Na} calculated by eq.(5.15) was in good agreement (0.6 to 0.9 times) with chemical analysis values, which indicates the usefulness of this procedure.

Na in-depth profiles in MOS gate SiO2 films on Si substrates were measured to clarify the relationship between mobile charge density and Na concentration in SiO2. Samples were SiO2 films (about 500 A thick), on which photoresist films (AZ-1350) of three different thickness were covered. It was found that Na ions penetrated SiO2 films when the photoresist films were removed by O2 plasma ashing(5.5). Figure 5.7 shows Na in-depth profiles calculated by eq.(5.15). This pile-up phenomena at the SiO2-Si interface differ from the U-shaped distribution(5.6), which is considered to be due to the repulsion effect of O_2^+ or O^+ ion

bombardment. In this case, electron temperatures in SiO2 and Si, respectively, were about 9360 K and 4050 K. In order to confirm Na concentration in SiO2 films, electrical measurement with Triangular Voltage Sweep (TVS) method and chemical analysis with Atomic Absorption Spectrophotometry were carried out. Table 5.7 shows the results of integrated Na concentration by SIMS, TVS and AAS. While TVS values are in good agreement with AAS values, SIMS values prove 3 to 4 times as small as AAS values. Although this discrepancy has not been elucidated yet, the quantitative procedure proves useful also for C_{Na} determination in SiO2.

5.5 Discussion

(1) Chemical process and kinetic process in ionization

The secondary ion formation from semiconductor surfaces is discussed in this section. When the inert gas ions are used as the primary beam, the secondary ion intensity is generally increased by about 2 orders of magnitude by O2 gas admission into the sample chamber. This effect was explained as follows; the admitted oxygen molecules attack the sample surface to form the oxide layer on the surface, and the chemical ionization process takes place instead of the kinetic process. The former is the process in which the ionization yield of the element is strongly enhanced by breaking element-oxygen bonds, while the latter is the ion impact ionization.

As shown in Fig. 5.8, Si^{+} and B^{+} intensities are strongly enhanced in the case of B-doped Si substrate by the O2 admission of 1×10^{-5} Torr, while Si^{++} intensity is slightly decreased. In this case, the enhancement of Si^{+} ion intensity is regarded as the chemical process which might be due to the surface oxide formation on the Si substrate. On the other hand, the formation of Si^{++} ions is considered to be the kinetic process in which Si^{++} intensity is not affected by the oxide formation.

In order to compare the Si case with O2 admission to the SiO2 case, the same experiment as Fig.5.8 was performed for SiO2 films, and the ratio of Si^{++} intensity to Si^{+} was investigated for both cases, because this ratio is thought to express a ratio of the kinetic process to the chemical process.

Figure 5.9 shows the ratio for the Si substrate and the SiO2 film as a function of O2 partial pressure in the sample chamber. While the ratio for the Si substrate decreases almost 3 orders of magnitude, that for the SiO2 film decreases only by a factor of 2. This means that the ionization from the Si surface exposed by 1×10^{-5} Torr O2 becomes the chemical process from the kinetic process which is dominant at 10^{-7} Torr range. In addition, it can be said that the surface status of O2-admitted Si might be identical to that of SiO2 because both have the same value of I_{Si}^{++}/I_{Si}^{+}.

On the other hand, for compound semiconductors, no O2 admission effect was observed as shown in Fig. 5.10. However, it should be noted that O_2^+ primary ion beam produces higher secondary ion intensities and creates higher electron temperature plasma than Ar primary beam. In other words, only O2 ion beam can create the chemical process for compound semiconductors, which might be due to the fact that GaAs has an ion bonding to some extent between Ga^+ and As^-, and energetic oxygen ions are required to make Ga-O or As-O bonds.

Then, the secondary ion intensities from InGaAs sample for O2 and Ar beams were investigated as a function of primary beam energy. As shown in Fig. 5.11, the behavior above 5 kV accelerating voltage of O2 beam is quite different from that of Ar beam. In this case. the sample holder was biased at 2.95 kV , so the net ion energy was 2.05 keV for 5 kV. In order to elucidate the difference of the behavior, the LTE plasma model analysis was performed for 3, 6 and 10 kV accelerating voltages.

Figure 5.12 shows LTE plasma contour lines for both O2 and Ar beams. It should be noted that the LTE plasma , namely Te and Ne for O2 beam above 6keV becomes quite different from that for Ar beam, that is, higher Te for O2 beam, while the plasma is almost the same as for Ar beam at 3keV where the O2 ions have only 500 eV impinging energy. In this way, the requirement of high energy O2 ion bombardment for the formation of the chemical process is verified for compound semiconductors, while only O2 exposure is enough for elemental semiconductors and metals.

(2) Considerations on background of ion intensities

When the pressure in the analytical chamber is poor, the influence of molecules such as H2O, CO2, CO etc. bombarding the sample surface cannot be neglected for the detection limit of oxygen. The number of impinging molecules can be given by

$$N_i = 3.513 \times 10^{22} P_i / (M_i T_i)^{1/2} \quad \text{Molecules/cm}^2\,\text{sec} \quad (5.16)$$

Here, P_i is the pressure(Torr), M_i is the molecular number of the gas, and T_i is the temperature. When Cs^+ beam was rastered in the 250μmx250μm area at 10 keV, the etching rate of Si was about 50 A/sec. In other words, 1.6×10^{13} Si atoms/sec were ejected from the Si surface. On the other hand, 2.4×10^{9} molecules/sec impinge the Si surface at $P_i = 1 \times 10^{-8}$ Torr according to eq. (5.16).

If CO molecules are considered as the dominant gas species in the chamber, and ejected at the same time as oxygen in Si with the energy of 4.53 keV, the detection limit of O in Si due to the chamber pressure comes to 0.015 %, that is 7.5×10^{18} cm^{-3}. Eventually, the residual CO partial pressure is low and its sticking coefficient might be less than unity. Therefore the detection limit is thought to be considerably low.

In order to make clear this point, O^- detection from Si was performed with admission of O2 gas into the chamber. Fig. 5.13 shows the O^- in-depth profile of O-implanted Si wafer at the base pressure of 1×10^{-8} Torr. Surface O^- pile-up corresponds to the natural oxide. After reaching the background level of O^- intensity, O2 gas was introduced up to 2×10^{-8} Torr, where the O^- intensity increased by an order of magnitude. When O2 of 1×10^{-7}

Torr was admitted into the chamber, the intensity showed another order of magnitude increase.

Figure 5.14 which was derived from Fig. 5.13 shows the relationship between the O^- detection limit and pressure in the chamber. Since the pressure of 2×10^{-8} Torr consists of 1×10^{-8} Torr of residual gas containing CO2, H2O etc., and 1×10^{-8} Torr of pure O2, the straight line can be drawn. Therefore, the detection limit at the base pressure of 1×10^{-8} Torr correponds to that with O2 introduction up to 1×10^{-9} Torr. Since the O^- detection limit calculated by eq.(5.16) at O2 pressure of 1×10^{-9} Torr comes to 1.4×10^{18} cm^{-3}, the predicted value by eq.(5.16) is found to be in good agreement with the experimental value, that is 1.7×10^{18} cm^{-3}. Moreover, when the measurement was performed at 4×10^{-9} Torr, the background level of O^- intensity went down to 5×10^{17} cm^{-3}. Therefore, it can be said that O detection limit is explained by the residual gas impingement with the sticking coefficient of almost unity.

Next, the detection limit of O in GaAs was investigated. Figure 5.15 shows O^-, GaO^- and AsO^- in-depth profiles of O-implanted GaAs substrate using Cs^+ beam. While SiO^- is barely detected for O-implanted Si, GaO^- and AsO^- show almost the same sensitivity as O^-. This implies that O in GaAs should have different chemical state from O in Si. Taking into consideration the oxygen admission effect on secondary ion intensities of Si and GaAs as described in Figs. 5.8 and 5.10,GaAs oxide might be in forms of GaO and AsO, while Si oxide might be SiO which is easily broken to Si^+ with high intensity enhanced by the chemical

process and O^-. On the other hand, GaO and AsO stay as the molecular form, so Ga^+ and As^+ intensities are not enhanced by the O2 admission.

Furtherfore the effect of residual gas pressure on O^- intensity was surveyed. Figure 5.16 shows O^- in-depth profiles of O-implanted GaAs at different pressure. They show the same profiles except the surface O^- intensity. Here, the base value is $2x10^{17}$ cm^{-3}. This result indicates that $2x10^{17}$ cm^{-3} might be the bulk concentration of O in GaAs. Using much lower O concentration GaAs wafers, the detection limit of this SIMS was found to be less than $5x10^{16}$ cm^{-3}.

In addition to the base pressure, there are other factors which influence SIMS detection limit. The dominant factor is the surface contamination of the sample chamber wall. Figure 5.17 shows Si in-depth profiles measured using $O2^+$ beam under three conditions. (1) indicates the profile measured after measuring Si wafers for more than a week, (2) that measured after measuring GaAs wafers for two days, and (3) that measured under the same condition as (2) except biasing the sample at 4.43kV. After Si measurement, the Si base value in GaAs was $3x10^{18}$ cm^{-3}, while after coating the chamber wall (in particular the immersion lens) in front of the sample with GaAs the background level decreased down to $1x10^{18}$ cm^{-3}. Furthermore, taking into consideration that Si^+ ions from the contamination might have different energy from that from the sample, the sample holder was biased at 4.43kV. In this way, we got the value of $2x10^{17}$ cm^{-3}.

On the other hand, this wall contamination effect was found

not to exist for the analysis of As in Si, because exactly identical profiles were obtained with or without As contamination due to GaAs analysis beforehand.

5.6 Conclusion

The quantitative analytical technique based on the LTE plasma model was applied to semiconductors, in particular GaAs and Si for the first time. The validity was checked using other bulk analytical techniques such as Emission Spectroscopy. Activation Analysis and Atomic Absorption Spectroscopy. O_2^+ primary beam was found to be superior to Ar^+ beam for this LTE model calculation.

The simplified quantitative procedure for SIMS was developed and applied to Na impurity analysis in Si and SiO2. Furthermore, the Na in-depth profiles in MOS gate oxides were obtained, and showed good agreement with the electrical measurement, that is TVS.

The effect of the base pressure in the chamber and the surface contamination of the chamber wall on the background value of impurities was also discussed. The difference between the detection limit of oxygen in Si (5×10^{17} cm^{-3}) and that in GaAs (5×10^{16} cm^{-3}) might be attributable to the oxygen sticking coefficient on to both surfaces. The value in Si can be quantitatively explained by the residual gas impinging onto the Si surface assuming the sticking coefficient is almost unity.

Furthermore, it is found that the sample biasing technique is useful for the impurity analysis of elements which easily contaminate the chamber wall, especially the immersion lens in front of the sample.

References for chapter 5

5.1) C. A. Andersen and J. R. Hinthorne, Anal. Chem. 45 (1973) 1421.

5.2) C. W. Magee and W. L. Harrington, Appl. Phys. Lett. 33 (1978) 193.

5.3) M. Oshima, M. Seki and I. Kawashima, Jpn. J. Appl. Phys. 17 (1978) 1697.

5.4) W. Kern and D. A. Puotinen, RCA Review, June 81970) 187.

5.5) H. Karter, ECS Spring Meeting, 1976, Washington, D. C. P.335.

5.6) F. M. Fowkes and F. E. Witherell, IEEE Trans. NS 21 (1974) 67.

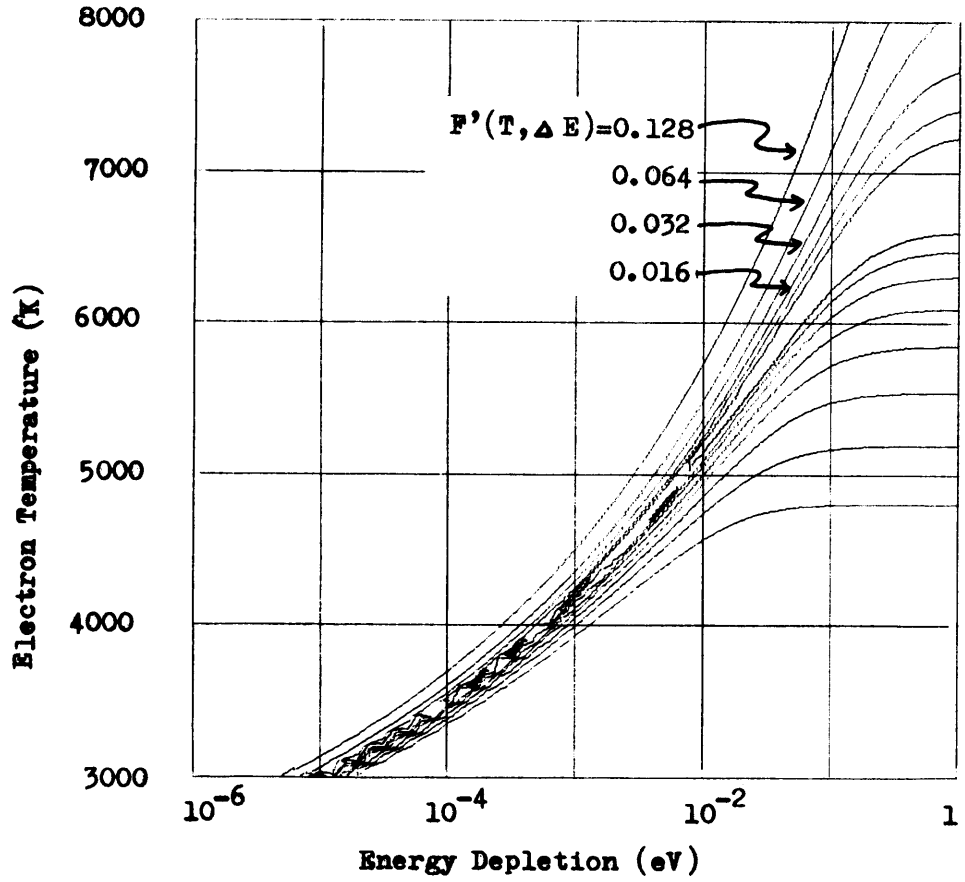

Fig.5.1 Contour line of the Fe-Cr low alloy steel sample in Te, ΔE space, calculated on the basis of the LTE plasma model.

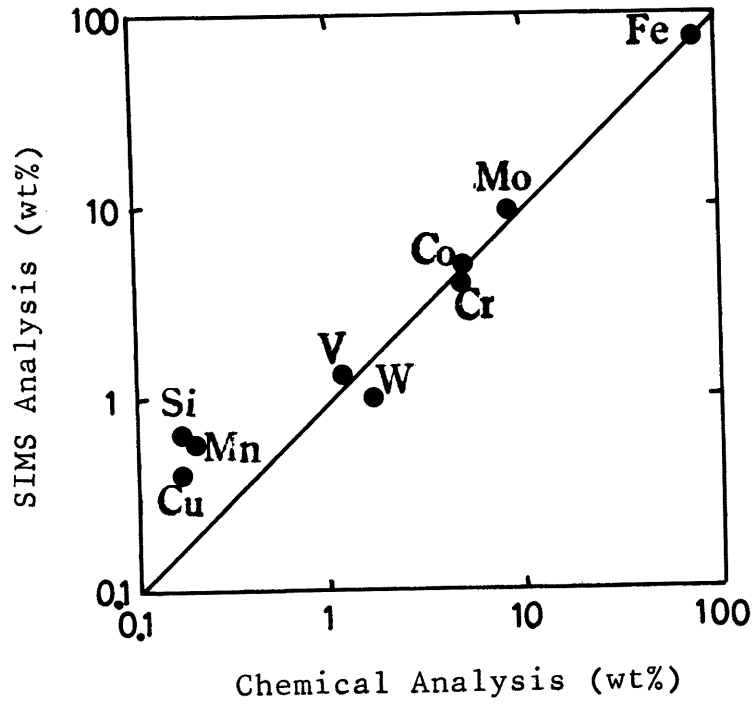

Fig.5.2 Comparison of SIMS analyses with chemical analyses for a number of elements in the low alloy steel sample. Internal standards are all elements.

Table 5.1 Electron temperature and In concentration determined by eq. (5.9) under 6 SIMS conditions. Sample: $In_{0.1}Ga_{0.9}As$ (C_{In} =0.05).

SIMS Condition (Accelerating Voltage)	Ar^+ beam			O_2^+ beam		
	3KV	6KV	10KV	3KV	6KV	10KV
Electron Temperature	4620K	3930K	4050K	4630K	5600K	5500K
In Concentration	0.054	0.054	0.056	0.056	0.055	0.065

Table 5.2 Experimental parameters of Emission Spectoroscopy.

Spectrometer	3.4 grating spectrometer (Shimadzu GE-340) grating ; PG-1200 (1200 lines/mm) resolving power ; 2.5Å /mm
Slit width	20μm
Excitation	DC arc 200V, 10A
Exposure time	30 sec without pre-discharge
Electrode gap	4 mm
Electrodes	Upper ; graphite rod, 5mmϕ, 60° cone Lower ; graphite rod, 5mmϕ, electrode hole (4mmϕ, 4mm deep)
Photoplate	Eastman Kodak SA-1
Development	D-19 20℃ 4min
Fixation	5min
Density measurement	Microphotometer (Shimadzu PD-20 type)
Line analyzed	Si ; 2881.578Å Fe ; 3719.935Å etc.
Internal standard line	Y ; 2956.04 Å

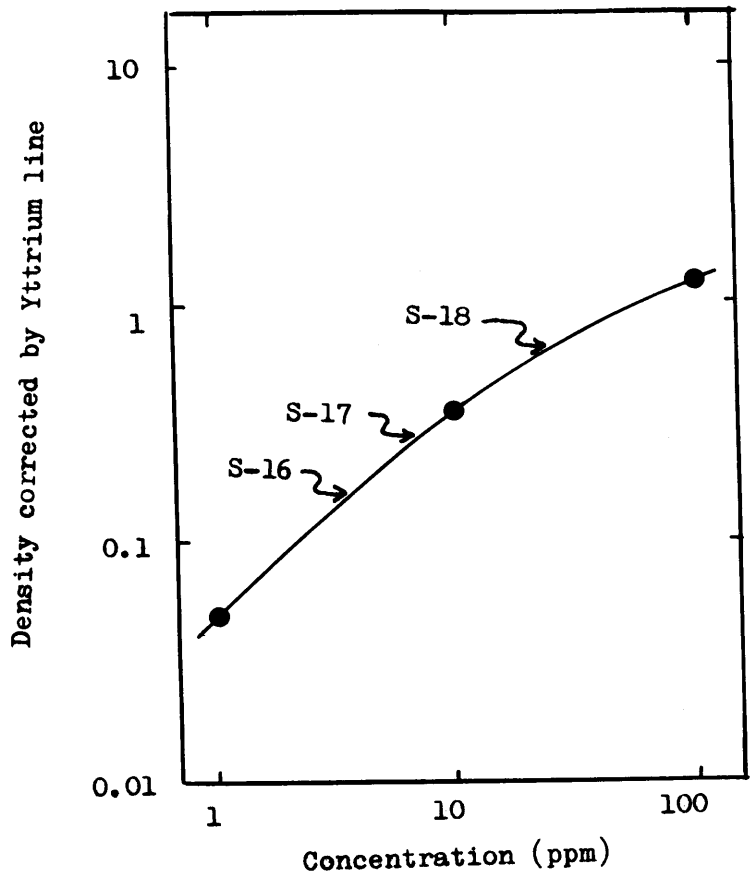

Fig.5.3 Calibration curve of Si in GaAs measured by means of Emission Spectroscopy.

Table 5.3 Carrier concentrations and Si concentrations in GaAs measured by SIMS (primary ion; Ar^+ and $O2^+$) and Emission Spectroscopy.

SAMPLE		S-16	S-17	S-18
CARRIER CONCENTRATION		6.3×10^{16}	1.8×10^{17}	2.1×10^{18}
SIMS	Ar^+ BEAM	1.3×10^{18}	3.6×10^{18}	6.4×10^{18}
	O_2^+ BEAM	7.2×10^{17}	7.6×10^{17}	2.0×10^{18}
EMISSION SPECTROSCOPY		8×10^{17}	5×10^{17}	3×10^{18}

(CM^{-3})

Table 5.4 Impurity concentrations in S-16, S-17 and S-18 samples calculated on the basis of the LTE plasma model. Primary ion; O_2^+. 0.70E-7 means 0.70×10^{-7}

Chemical Analysis (wt) Ga=0.482 As=0.518			
Calculated Value (wt)			
Element	S−16	S−17	S−18
Ga	0.4809	0.4809	0.4807
As	0.5190	0.5190	0.5191
Na	0.70E-7	0.10E-6	0.13E-6
Mg	0.82E-6	0.79E-6	0.44E-6
Al	0.21E-5	0.27E-5	0.49E-5
Si	0.63E-4	0.67E-4	0.17E-3
K	0.40E-7	0.30E-7	0.30E-7
Ca	0.98E-6	0.22E-5	0.21E-5
Cr	0.52E-5	0.71E-6	0.29E-5
Fe	0.44E-4	0.80E-5	0.25E-4
electron temperature	5849 K	5836 K	5864 K
electron density	1.05E16	1.05E16	1.05E16 (cm^{-3})

Table 5.5 Impurity concentrations in the epitaxial layer and the substrate calculated on the basis of the LTE plasma model. Primary ion; O_2^+.

IMPURITY	EPITAXIAL LAYER $In_xGa_{1-x}As$	SUBSTRATE GaAs
Na	5.2E17	2.9E15
Mg	———	1.4E17
Al	2.6E17	4.7E17
Si	1.9E18	8.7E18
K	1.1E18	8.1E15
Ca	7.1E17	6.9E16
Ti	5.2E16	1.0E18
Cr	3.0E17	1.4E18
Mn	———	1.6E17
Fe	1.2E18	3.8E18
Ni	3.8E17	———
Cu	1.4E17	———
Te	3746 K	5944 K
Ne	4.67E10cm^{-3}	1.13E16cm^{-3}

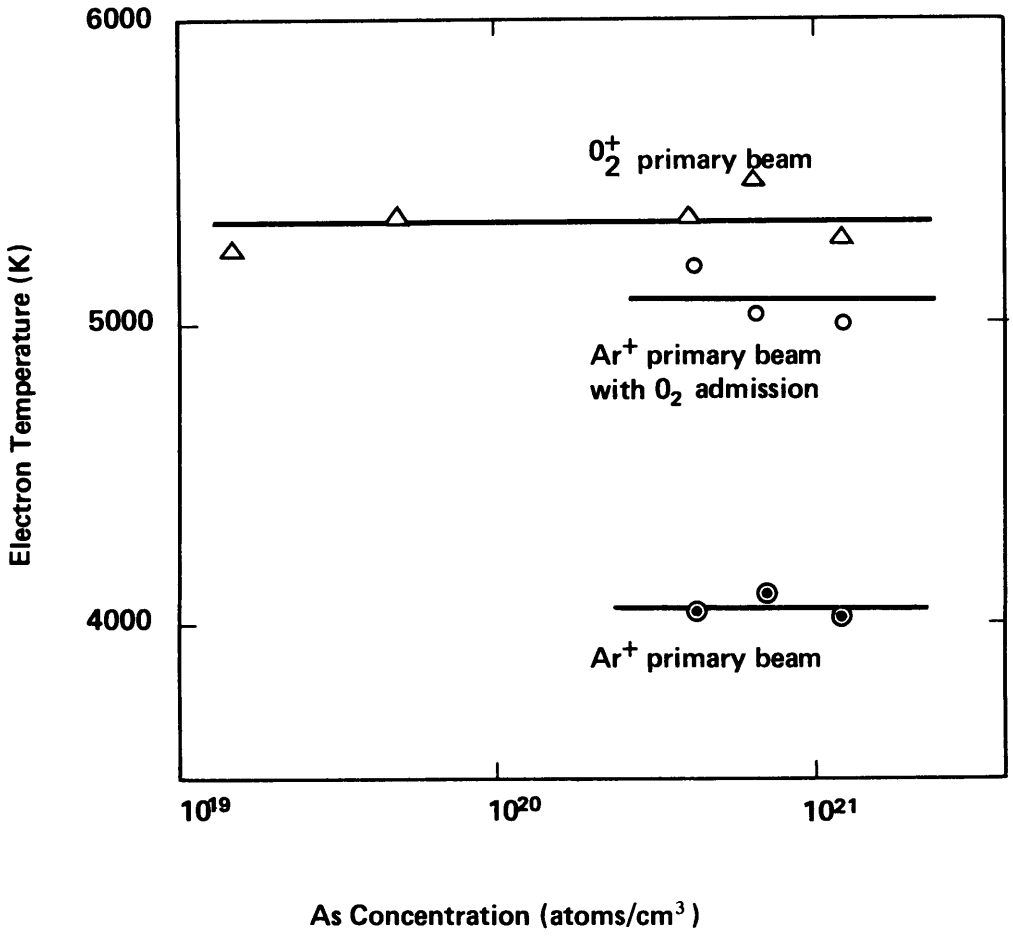

Fig.5.4 Electron temperatures determined by eq. (5.9) with Ar^+ and $O2^+$ primary beam as a function of dopant As concentration in Si.

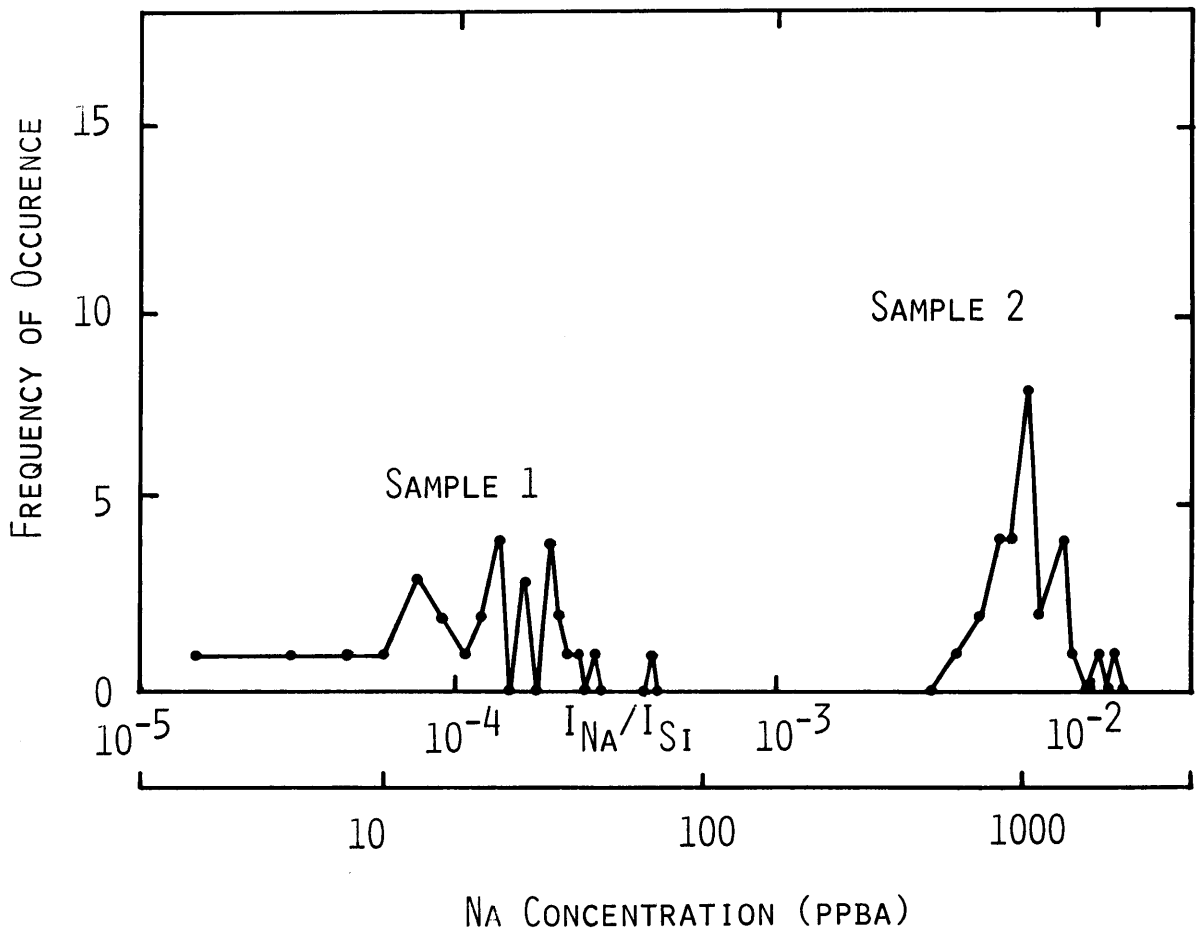

Fig.5.5 C_{Na} frequency of occurrence in the surface region of a cleaned Si wafer (Sample 1) and a contaminated one (Sample 2). SIMS condition: Ar^+ primary beam at 10kV accelerating voltage in high vacuum.

Table 5.6 Quantitative analysis of Na concentration in borosilicate glasses.

Sample (C_{Na})	No. 1 (0.80%)	No. 2 (2.1%)	No. 3 (3.8%)	No. 4 (6.9%)
Electron temperature	13110 K	12960 K	12620 K	12340 K
C_{Na} (uncorrected)	0.12%	0.26%	0.33%	0.72%
C_{Na} (corrected)	0.55%	1.2%	1.4%	2.9%

Table 5.7 Na concentration measured by SIMS, compared with TVS and AAS.

Sample	NO. 1 (Resist 0.37μm)	NO.2 (Resist 0.57 μm)	NO.3 (Resist 0.74 μm)
SIMS (integrated value)	1.3×10^{13} cm^{-2}	2.0×10^{13} cm^{-2}	2.8×10^{13} cm^{-2}
TVS	5.5×10^{13} cm^{-2}	7.4×10^{13} cm^{-2}	7.9×10^{13} cm^{-2}
AAS	5.9×10^{13} cm^{-2}	7.1×10^{13} cm^{-2}	7.7×10^{13} cm^{-2}

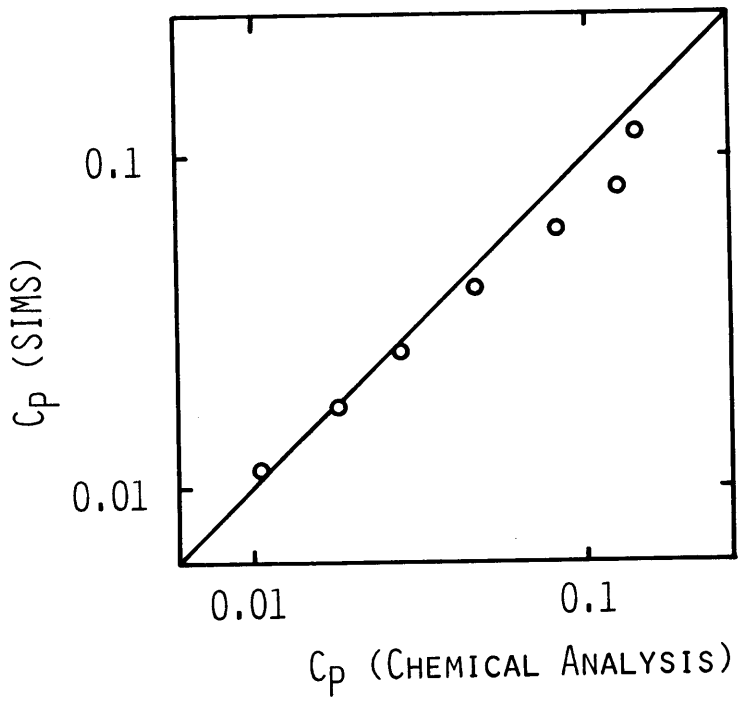

Fig.5.6 Comparison of phosphorous concentration determined by SIMS with that measured by spectrophotometry. SIMS condition is the same as Fig.5.5

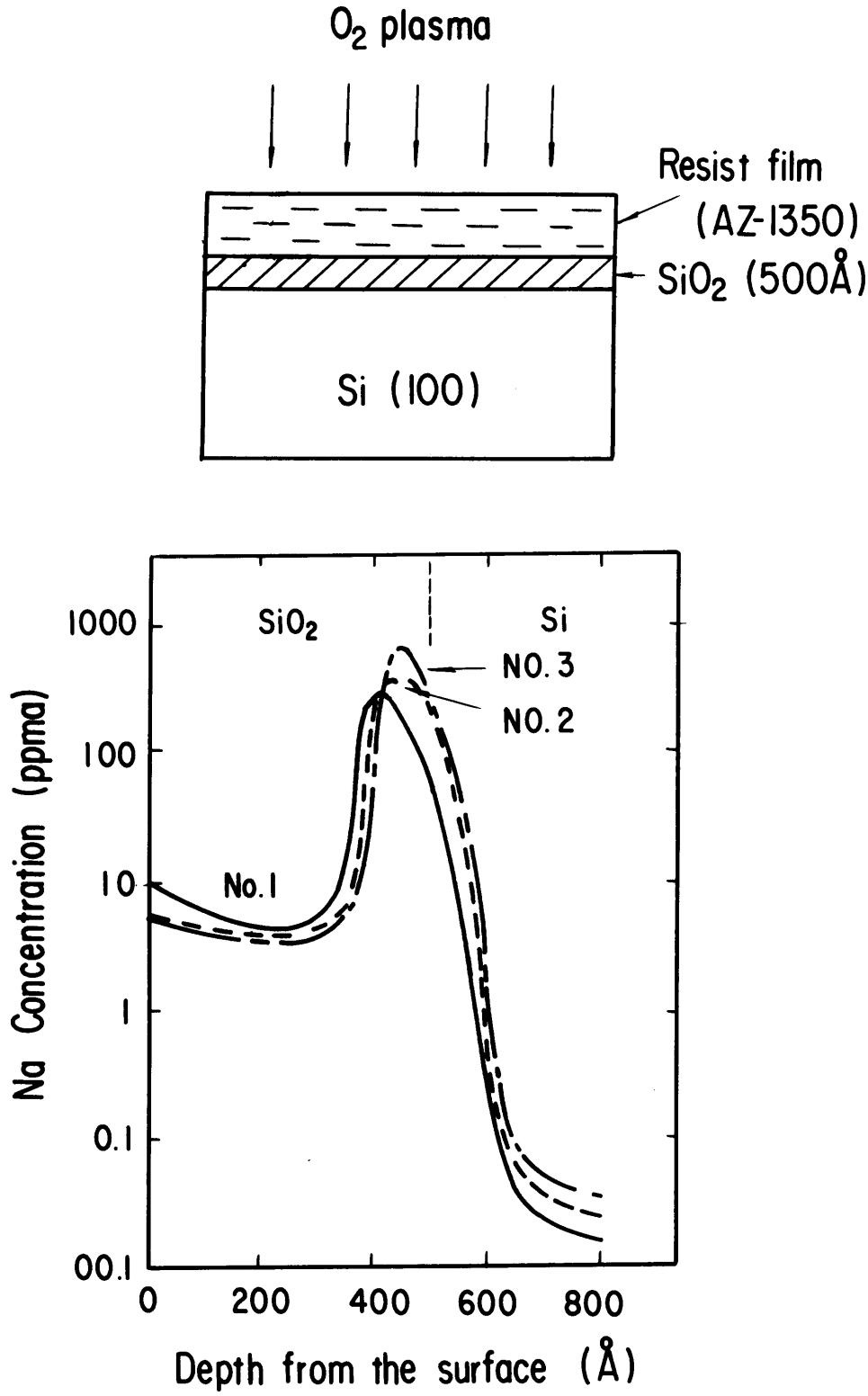

Fig. 5.7 Na distribution measured by SIMS in SiO_2 films, which were covered with photoresist films (AZ-1350) and removed by O_2 plasma ashing.

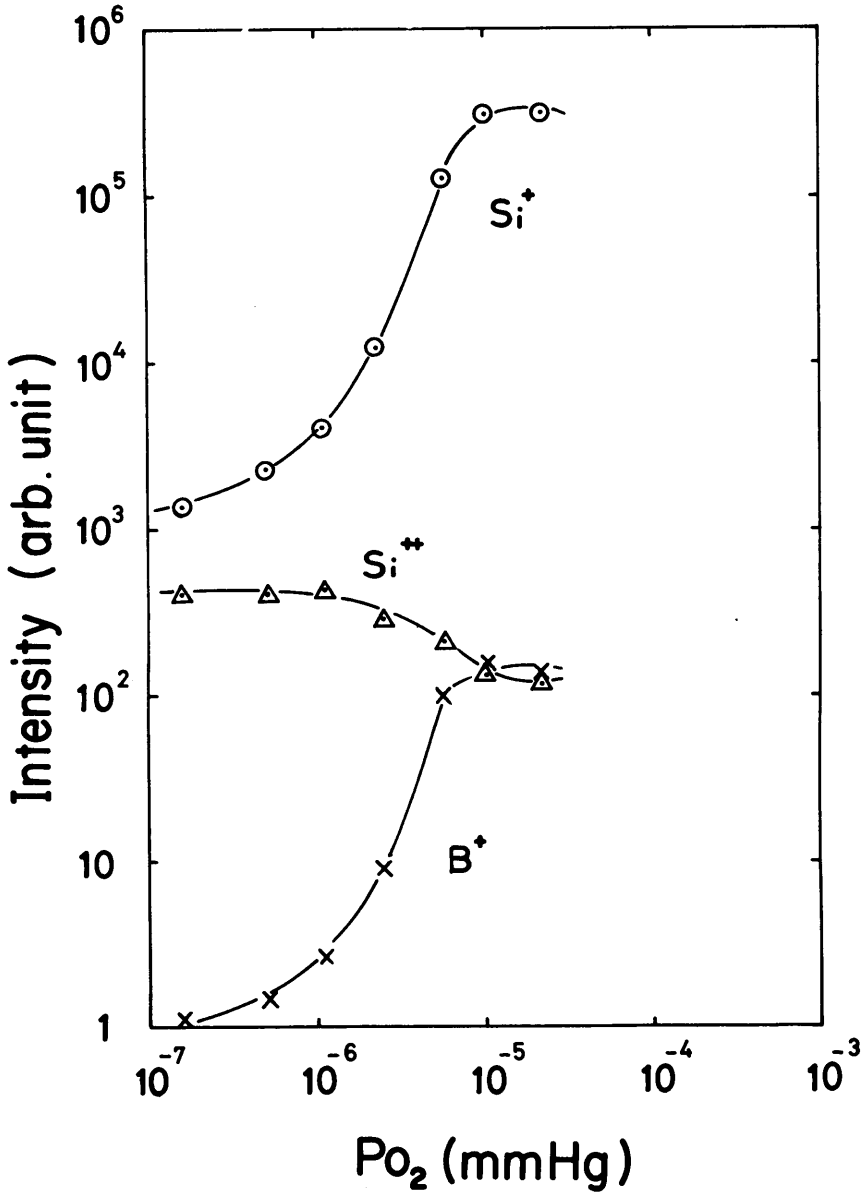

Fig.5.8 SIMS intensities of Si^+, Si^{++}, B^+ as a function of O2 partial pressure in the analysis chamber.

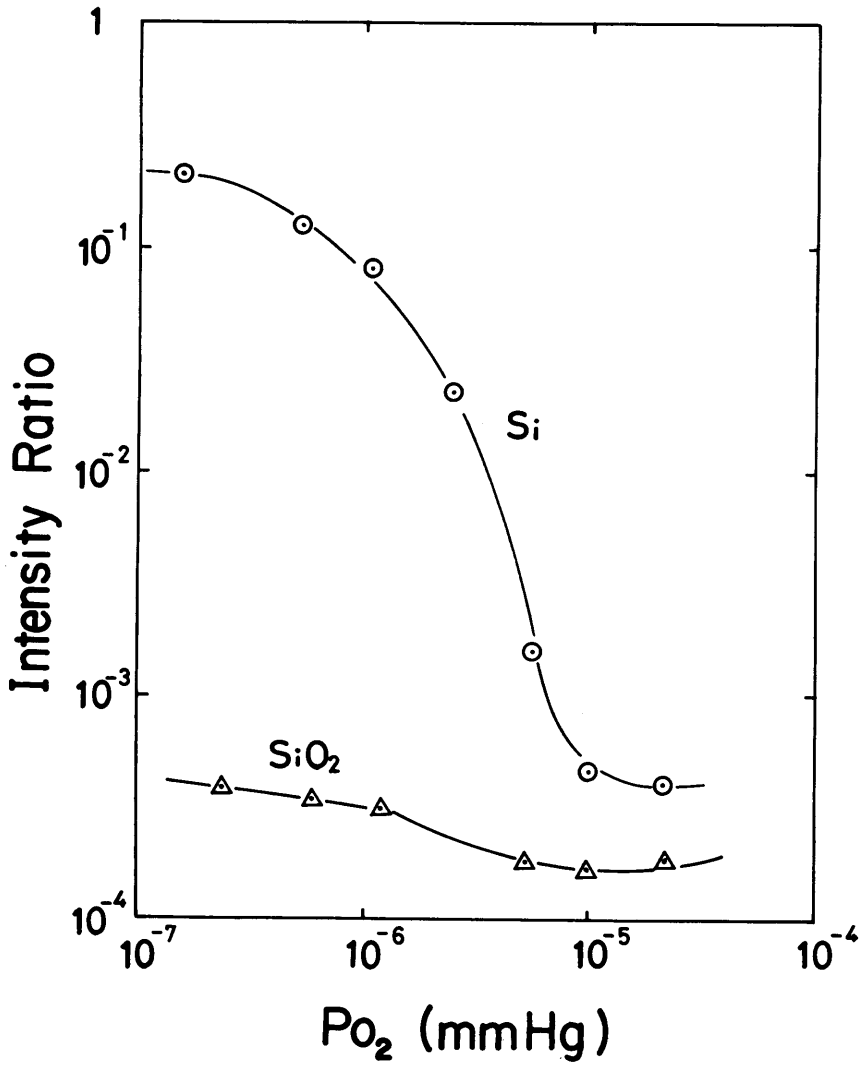

Fig. 5.9 Si^{++}/Si^{+} intensity ratios of Si and SiO2 as a function of O2 partial pressure. Si^{++}/Si^{+} of $2-4\times10^{-4}$ corresponds to the silicon oxide state.

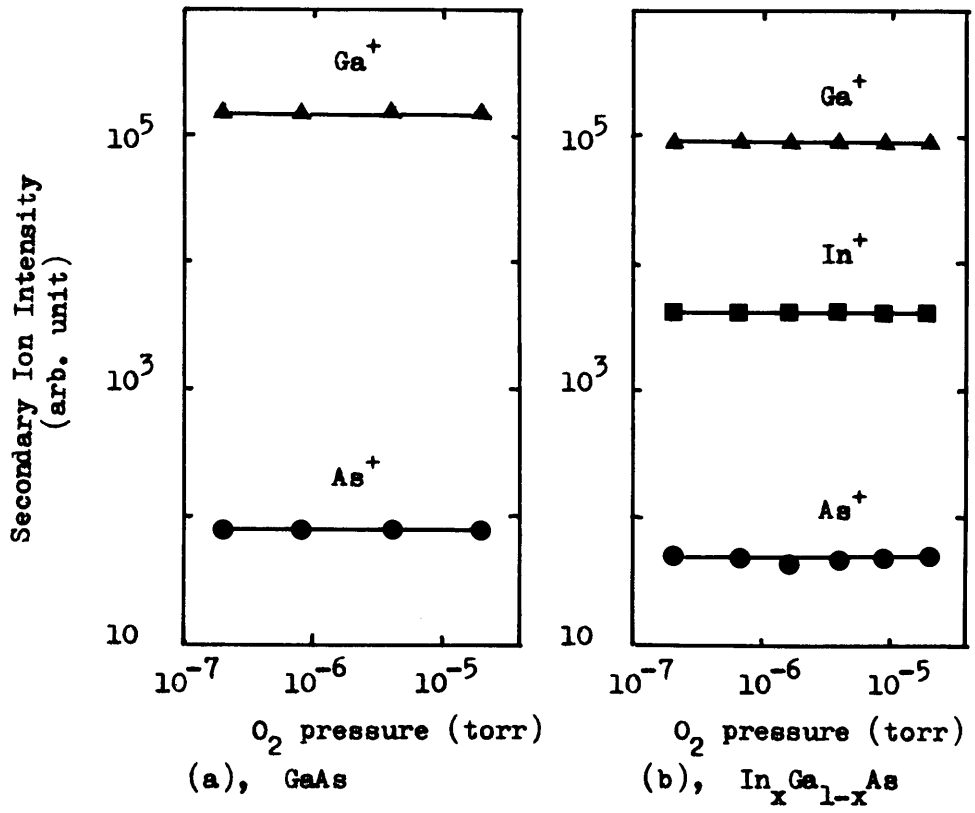

Fig.5.10 Dependence of secondary ion intensities on 02 partial pressure in the analysis chamber. Samples are GaAs and InGaAs.

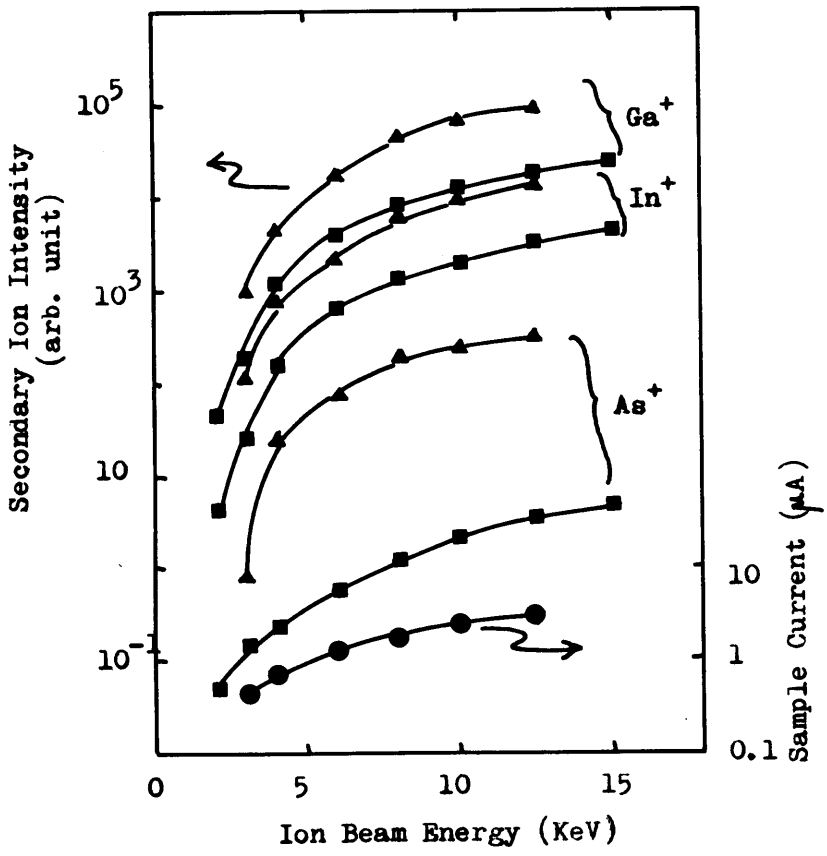

Fig.5.11 Dependence of secondary ion intensities on primary ion beam energy. Sample; In Ga As. Primary ions are Ar^+ (squares) and $O2^+$ (triangles).

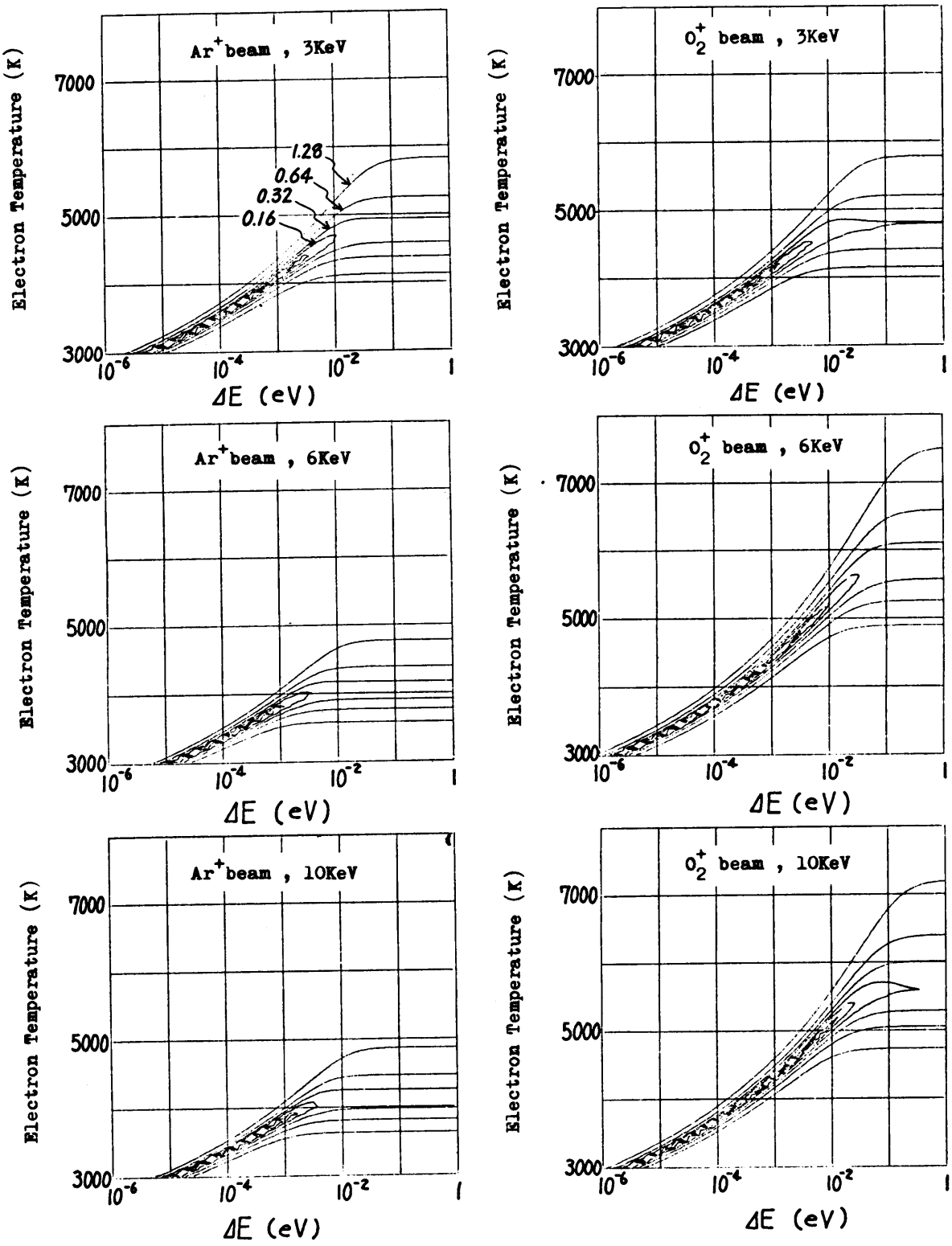

Fig.5.12 Dependence of the contour lines of F(T,ΔE) on primary ion species and accelerated voltage. Sample is $In_xGa_{1-x}As$.

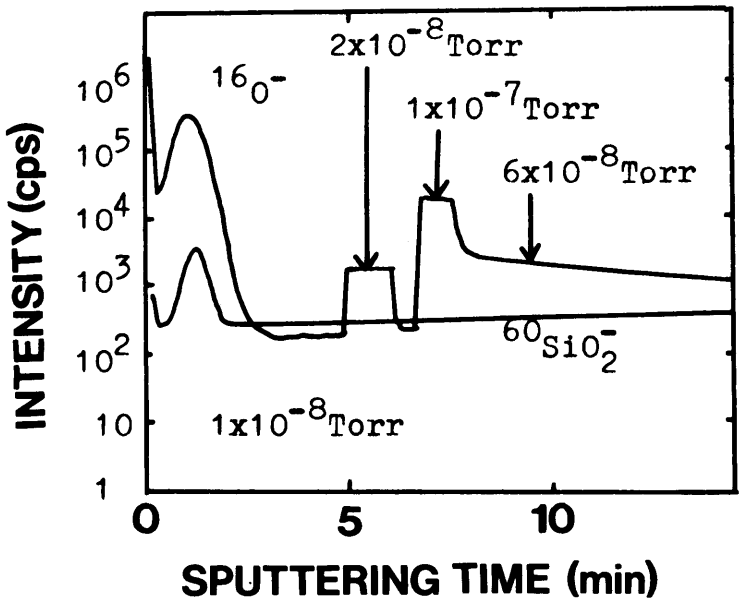

Fig. 5.13 Influence of analytical chamber pressure on O^- intensity. Primary beam; Cs^+ at 10 keV. The pressure was controlled by oxygen introduction through a variable leak valve.

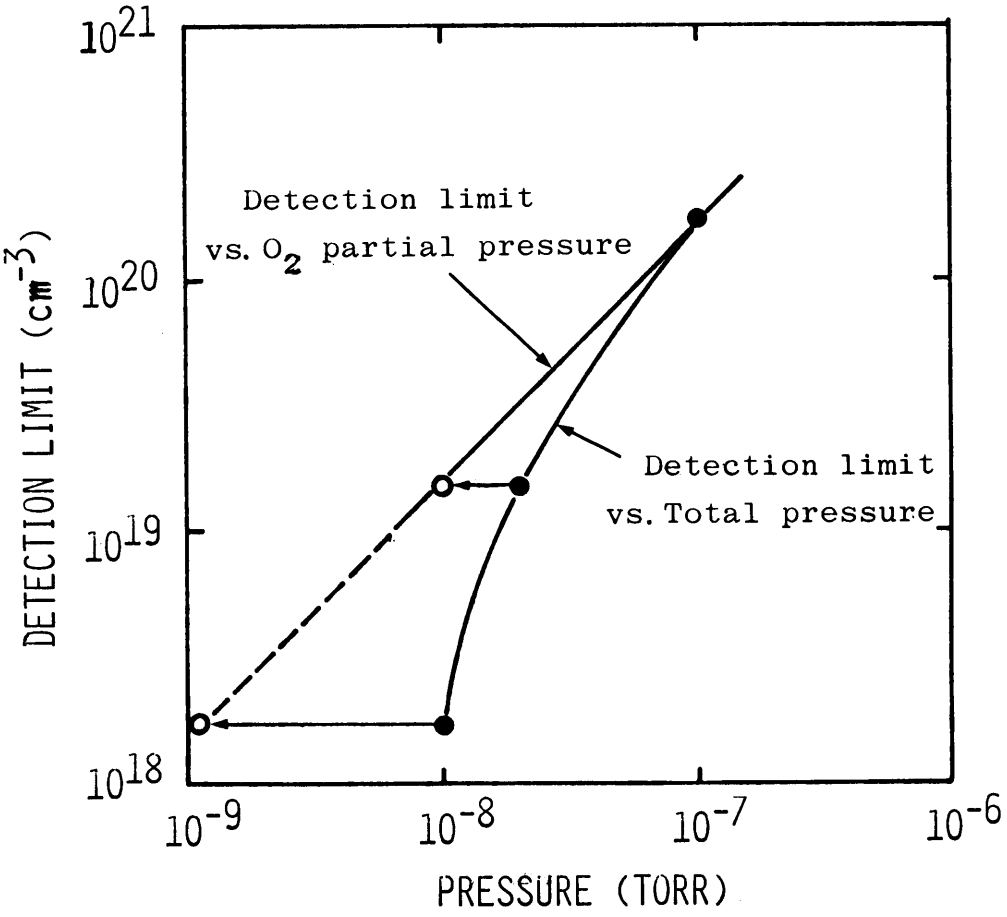

Fig.5.14 Dependence of O^- detection limit on total pressure and O2 partial pressure, which was derived from Fig.5.13.

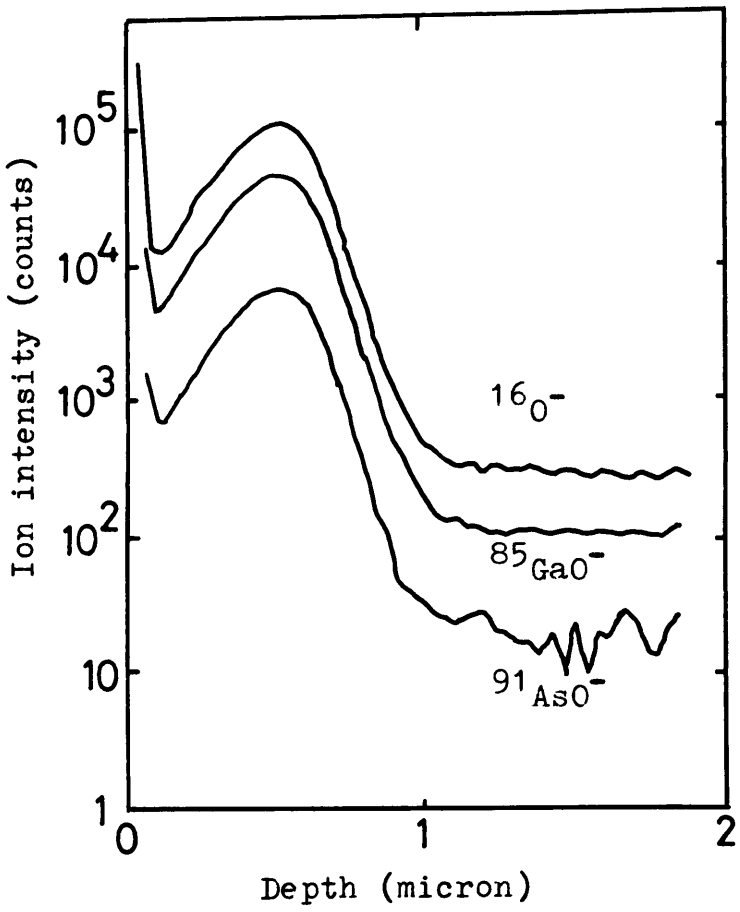

Fig.5.15 In-depth intensity profiles of $^{16}O^-$, $^{85}GaO^-$ and $^{91}AsO^-$, measured using Cs^+ primary beam at 10 keV. O implantation; 300 keV, 4×10^{15} cm^{-2}.

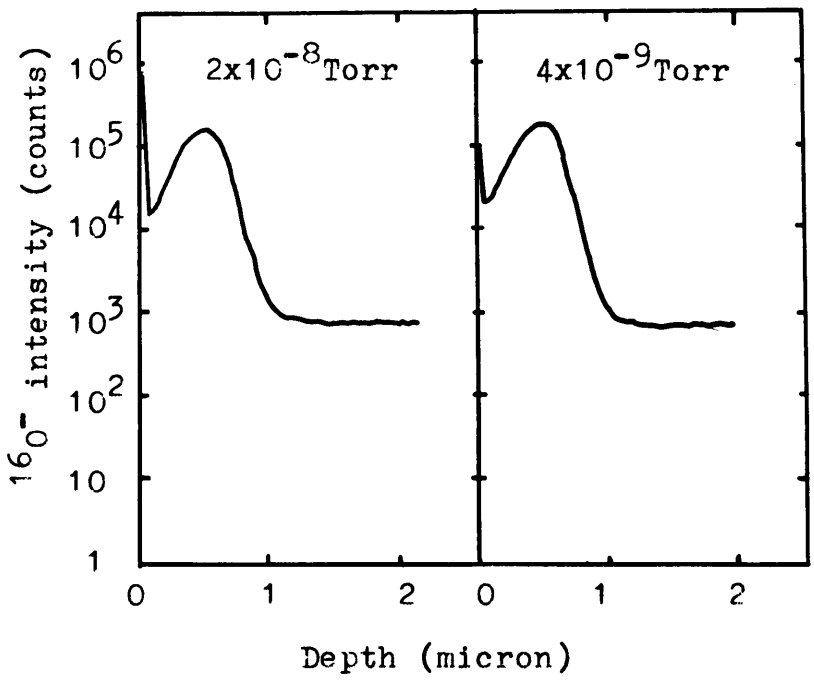

Fig.5.16 In-depth profile of O in GaAs measured using Cs^+ primary beam at the analytical chamber pressure of $2x10^{-8}$ Torr and $4x10^{-9}$ Torr. The same profile except surface oxygen concentration could be obtained under both conditions.

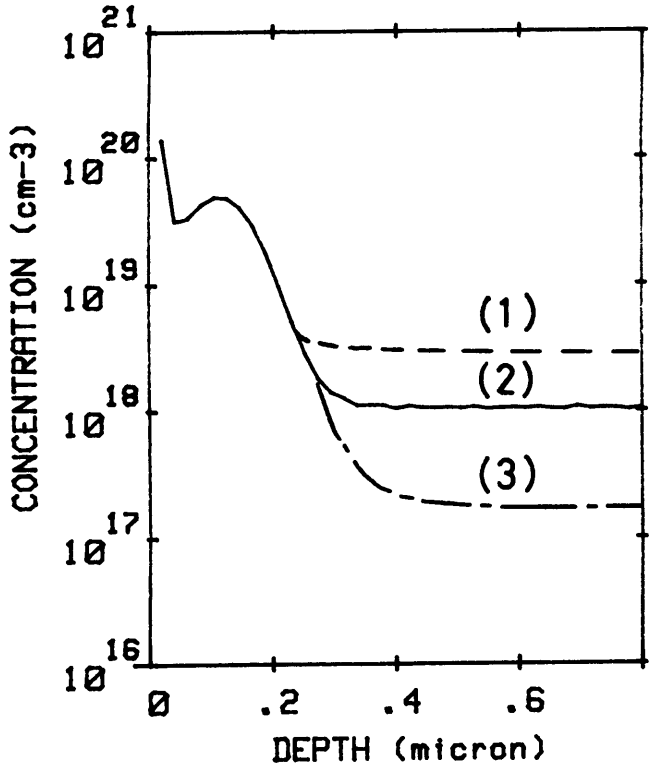

Fig.5.17 Si in-depth profiles measured using O_2^+ primary beam at 15 keV under three conditions: (1) measured just after measuring Si wafers for more than a week, (2) measured after measuring GaAs wafers for two days biasing the sample at 4.53kV, and (3) measured under the same condition as (2) biasing the sample at 4.43kV.

Chapter 6 SIMS Analysis of Thermal Conversion Layers in GaAs *

6.1 Introduction

Semi-insulating GaAs substrates provide active layers for high speed GaAs IC devices after ion implantation and annealing processes.However, it has been reported that these substrates usually doped with Cr are thermally unstable, and show type conversion during heat treatment. These phemomena (6.1-3) are reportedly due to Cr out-diffusion and Mn accumulation at the surface, where Mn serves as shallow acceptors. However, the relationship between Cr depletion and Mn accumulation has not been quantitatively discussed yet.

This chapter aims at a better understanding of this relationship during various kinds of heat treatment. Cr and Mn redistribution is discussed in terms of SIMS depth profiles from their dependence on annealing time, ambient gases, annealing temperature, Cr concentration in substrates, capping films and ion implantation. Furthermore redistribution mechanism is also discussed.

*Most of this part has been reported in ref. (A.9).

6.2 Experimental procedure

Semi-insulating, Cr-doped wafers used in this study were of (100) orientation and grown by the horizontal Bridgeman technique (HB) and the liquid encapsulation Czochralski (LEC) method. Their initial preparation was the same as that reported by Watanabe et al (6.4). Annealing was performed at 700 C to 900 C. The ambient gas was H2 purified by a Pd-diffuser. In the case of As4/H2, the mixture gas was supplied by H2 passing through a GaAs chunk strainer held at the annealing temperature. Therefore, the atmosphere is not the case of CAT (Controlled Atmosphere Technique). The estimated arsenic partial pressure is lower than 5×10^{-4} Torr at 800 C(6.5). Ion implantation of Cr was done at room temperature at 300 keV with a dose of 10^{13} to 10^{15} cm^{-2}. Sputtered SiO2 and plasma CVD Si3N4 films were used as capping layers.

An ion microanalyzer with O2 primary ion bombardment was used to obtain the Cr, Mn and other impurity depth profiles. Calibration of atomic concectration was established using standards prepared by ion implantation. The Cr detection limit was examined using an epitaxially grown undoped GaAs film on GaAs substrate. The minimum detectable concentration of Cr was 5×10^{14} cm^{-3}. Talystep was employed to measure the resultant crater depth. While an area of 250 μm square was sputtered, secondary ions were collected from the central area 60μm in diameter. The depth resolution was checked using a 8600 A Mo film on a Si substrate. From the width of the interface $\Delta d/d$ (the depth resolution) was found to be 8.7%, mainly due to knock-on effects

and sputter redeposition.

Photoluminescence measurements were carried out at 4.2 K with the sample immersed in liquid He, using an Ar laser as an excitation source.

6.3 Results and discussion

(1) Redistribution resulting from capless annealing

Figures 6.1 (a) and (b) show Cr and Mn depth profiles for samples annealed in two different furnaces at 800 C for 1 hr in H2 flow without capping layers. Both samples were from the same wafer. There is a remarkable difference in the amount of accumulated Mn, while the Cr profiles look quite similar. This is the first reason why we believe that the Mn mainly originates from the ambient gas, presumably from heaters through the quartz tube.

The second reason is the large amount of accumulated Mn in the depleted region. If all of the Mn concentrated at the surface is to have come from the bulk material, then it must have diffused distances of up to 100 times the thickness of this surface region. In order to estimate the diffusion length of Mn in GaAs at 800 C for 1 hr, we employed the diffusion coefficient with As reported by Sze(6.6). It comes to only about 2μm at most, which is too small to account for the Mn accumulation.

The third reason is that when the sample was annealed again after polishing off about 10μm from the surface, similar depth profiles of Cr and Mn were obtained. While Klein et al(6.2) reported that Mn has begun to be depleted by the sequential heating and removal of Mn that has diffused to the surface, we observed almost the same Mn accumulation after the heat/polish cycle.

Figure 6.2 shows PL spectra of the sample used in Fig.6.1 (a). Peak A is reportedly carbon-related (carbon shallow

acceptors), and peak B is due to Mn occupying Ga vacancies(6.7). Peaks at 1.375 eV and 1.34 eV are attributable to peak B's LO phonon replica and its 2 LO phonon replica, respectively. Interestingly, after being incorporated into the GaAs, Mn diffuses into the Cr-depleted region and occupies Ga vacancies during H2 annealing, although the diffusion coefficient of Mn is reportedly larger than that of Cr.

In order to understand the redistribution mechanism, the dependence of the Cr depletion depth on annealing time was investigated. Figure 6.3 shows the depth of the Cr out-diffused region, which is defined as the depth where the Cr concentration becomes 84% of the original value, as a function of annealing time. Here, 84% is the value of erf $(x/2\sqrt{Dt})$ when x is equal to $2\sqrt{Dt}$. Open circles indicate H2 ambient gas, and open squares(6.8) As4/H2 (H2 flow with a GaAs strainer). Estimated values were calculated using the reported Cr diffusion coefficient(6.9) and the first term $(\mathrm{erf}(x/2\sqrt{Dt}))$ of the equation reported by Smith et al(6.10). Although the rough estimation (solid line) shows slightly higher values than experimental results, it is evident that the diffusion process is dominant in Cr redistribution, judging from the proportionality of the depletion depth to $\sqrt{t}$. The discrepancy between estimation and experiment might be attributed to surface reactions forming volatile Cr compounds.

Kasahara et al(6.11) reported that Cr redistribution is controlled by the partial pressure of arsenic during annealing, since the "interfacial conductance" decreases with high arsenic partial pressure. However, our results show no significant

difference in Cr out-diffusion under various ambient gases up to annealing time of 1 hr. This is probably because our atmosphere of As4/H2 did not reach the sufficient arsenic pressure to prevent the loss of As and dissociation of GaAs.

Next,we investigated the dependence of Cr and Mn redistribution on the original substrate Cr concentration. Figure 4 shows Cr depth profiles in GaAs substrates with three different Cr concentrations. Curves (a) and (b) are for Cr-doped HB crystals and curve (c) for undoped LEC. Annealing was performed at 800 C for 1 hr in H2. While (a) and (b) show Cr depletion, (c) shows no change in the Cr profile. Mn accumulated in Cr-depleted regions. As a result, there was almost no Mn accumulation in the case of (c).

These results suggest two important points. One is that there might be a "minimum or critical Cr concentration" for Cr depletion. The level is about 5×10^{15} cm^{-3} which is in good agreement with other authors' results(6.12,13). Therefore, no Cr depletion takes place for lower Cr content substrates than that critical level. This critical concentration shows no dependence on annealing temperature suggesting that it might not be due to thermal equilibrium considerations. More detailed work should be done.

The other point is that Mn was incorporated mainly into Cr-depleted sites, that is Ga vacancies. Zucca(6.14) reported that Mn diffusivity is large under a condition of V_{Ga} population excess. Sze(6.6) reported a dependence of the Mn diffusion coefficient on the pressence or absence of As in the ambient gas,

which in turn would strongly effect the number of As vacancies in the lattice. The precise role of Ga and As vacancies in the redistribution of Cr and Mn is still the subject of active discussion.

(2) Redistribution resulting from Cr ion implantation

Cr ion implanted samples were annealed to investigate their Cr depletion behavior. Figures 6.5 (a), (b) and (c) are for Cr-implanted GaAs substrates with 10^{13}, 10^{14} and 10^{15} cm^{-2} doses at 300 KeV, respectively. In Fig.6.5(a), most of the implanted Cr on interstitial sites out-diffused and Mn accumulation took place to the same degree as in the unimplanted samples, indicating that the Cr on Ga site was also depleted. In this case, the accumulation of Cr at the surface and the bump located around Rp + ΔRp reported by Simondet et al(6.15) were not observed. In Fig. 6.5(b), Cr also out-diffused toward the surface and piled up with the surface concentration exceeding the solid solubility limit in GaAs ($2\text{-}3\times10^{17}$ cm^{-3}).

When the dose exceeded the amorphizing limit, a large area of Cr depletion appeared, extending to the same depth as the region of Mn accumulation, as shown in Fig.6.5(c). The Cr depth profile does not look like the "error function" as predicted by simple diffusion theory. This may be due to the existence of a critical Cr concentration which limits the minimum Cr level. Even taking into account the amorphized area that would be caused by the dosage and the energy used, this region of enhanced Cr out-diffusion seems to be too deep. As for the sample annealed at 850 C, Cr depletion extended to a depth of 9 μm. This result is quite different from that (Fig. 5) reported by Simondet(6.15). Their sample was annealed at 772 C for 15 minutes, after an implantation of 3×10^{14} Cr cm^{-2} at 190 KeV.

We consider this enhancement of Cr out-diffusion to be

mainly due to surface dissociation, while Magee et al(6.16) reported that out-diffusion was enhanced by defects created by implantation. This sample in Fig.6.5(c) showed considerable surface roughness compared to lower dosed samples, which may have been caused by surface thermal dissociation. Figure 6.6(a) shows an SIMS secondary ion image of $^{69}Ga^{+}$, and Fig.6.6(b) an image taken by a nomarski interference microscope. Although an $^{75}As^{+}$ ion image could not be obtained because of the low ionization yield of As (about 3 orders of magnitude lower than Ga), As^{+} depth profiles show that the surface region of this highly dosed sample was a little As deficient in comparison to the other samples. We consider this surface roughness to be due to Ga droplets (several microns in diameter) resulting from intense surface dissociation, which might be enhanced by the recrystalization of the amorphized region.

The difference between our results and those reported by Simondet can be attributed to this surface morphological change. Udagawa et al(6.17) reported that the agreement between calculations of Cr depletion profiles and experimental results became poor when samples were annealed for long times. This discrepancy was reportedly caused by the slightly matte surface, indicating the initiation of thermal dissociation. Further investigation will be needed to elucidate the cause of this surface morphological change.

(3) Redistribution resulting from capped annealing

Finally, in order to compare these results with capped annealing, SIMS analysis was performed on GaAs substrates capped with 3000 A SiO2 or 1600 A Si3N4 films. Here, appropriate electron bombardment during depth profiling was employed to prevent charging-up.

Figures 6.7 (a) and (b) show As, Cr and Mn depth profiles of GaAs. These samples were annealed in H2 for 1 hr at 800 C. The As^+ pile-up at the interface might be attributed to the well-known SIMS interface effect. When these samples were analyzed after removal of these films using HF + H2O solution, Cr showed the same profiles as before with a completely flat As^+ profile, and no Mn was detected in both cases. The amount of Cr piled-up at the surface proved to be equal to that depleted from the bulk within an uncertainty of 20%, indicating that Cr does not out-diffuse into capping films even when annealed at 800 C. In addition, these films were found to prevent Mn invasion from the ambient gas into the GaAs.

Note that the Cr and Mn ion intensity observed in the capping layers is anomalously high. In actual fact, the Cr and Mn concentrations are very low, but the ion intensitie are greatly enhanced in the capping layers by SIMS matrix element effects. This was experimentally verified by SIMS on Si3N4 films which had undergone the same Cr implantation.

Since the Cr-depleted regions were about 4 times as deep as those observed in capless annealing, the stress field caused by capping layers is thought to enhance Cr out-diffusion. This

strain field could arise from thermal mismach between the capping film and the GaAs.

As was the case for capless annealing, a critical Cr concentration for Cr depletion was observed. (In either case, the substrate Cr concentration was well below the solid solubility limit). Figure 6.8 shows the Cr depth profiles of GaAs subjected to capped annealing at 800 C in H2. While curve A shows Cr depletion, the Cr profile (B)(6.18) is not changed by annealing. Therefore, it can be said that substrates with a Cr concentration lower than the critical level (about 5×10^{15} cm^{-3}) do not suffer from Cr depletion in capped annealing.

The Cr depletion depth is plotted in Fig.6.9 as a function of 1/T (annealing temperature). The solid line indicates the estimated value from simple diffusion theory. Here we used $D = 4.3 \times 10^{3} \exp(-3.4/kT)$(6.7). The circles indicate capless annealing, the triangles ion-implantation (with a 10^{15} cm^{-2} dose), and the squares capped annealing. With regard to the diffusion coefficient of Cr in GaAs, there have been many different values reported in the literature. Sato(6.21) reported 1.6×10^{-12} cm^2/sec at 800 C, determined by an analysis of the conductive layer thickness resulting from capped annealing of Cr-doped GaAs. Wilson et al(6.22) reported $D_{800\ C}$ to be 6.7×10^{-12} cm^2/sec from an depth analysis of Cr-doped GaAs with an epitaxially grown GaAs layer, which is large compared to other values. Kasahara et al reported $D = 6.3 \times 10^{5} \exp(-3.4/kT)$ using the diffusion equation with the interfacial conductance(6.23). Judging from Fig.4 by Kasahara, the pre-exponential term might be 6.3×10^{3}, which fixes

$D_{800\,C}$ at 6×10^{-13} cm^2/sec. Simondet et al reported $D=2\times10^{-14}$ cm^2/sec at 772 C from a "crude calculation" using SIMS depth profiles of Cr in-diffusion in implanted and annealed GaAs. This seems too small, if defect-enhanced diffusion caused by ion implantation is taken into account. Therefore, the value given by ref.6.7 is adopted in this work.

From this graph (Fig.6.9), three important results can be pointed out. First, capless annealing causes Cr depletion which can be explained by simple diffusion theory in both HB and LEC crystals. However, in annealing at 750 C, Cr depletion and Mn accumulation are limited only to a shallow region. Kasahara et al reported that almost no Cr out-diffusion was observed after annealing at 700 C. At these low temperatures, the surface reaction necessary to allow Cr to evaporate might be the rate determining process for Cr depletion. In contrast, in the case of capped annealing, a deep depleted region was observed even for 700 C annealing because no surface reaction may be necessary.

The second point to note is the enhancement of Cr out-diffusion by ion implantation-induced defects. Deveaud et al (6.24) reported that implanted (600keV) Cr diffuses rapidly when annealed at 800 C ($D_{800\,C} > 10^{-12}$ cm^2/sec). Since our result at 800 C roughly coresponds to $D=5\times10^{-12}$ cm^2/sec, defects by ion implantation definitely act to enhance Cr out-diffusion. Perhaps the large activation energy (about 5 eV) is due to surface dissociation reactions in addition to defect-enhanced diffusion.

Finally, in capless annealing, Cr depletion is also enhanced

with a similar activation energy to that observed after capless annealing.

6.4 Conclusion

Cr and Mn redistribution during heat treatment has been investigated using SIMS and PL. Mn was found to be incorporated mainly from the ambient gas into Cr-depleted sites, namely Ga vacancies. Cr out-diffusion can be explained by simple diffusion theory except for low temperature annealing where surface reaction effects might dominate behavior. Cr out-diffusion is strongly enhanced in samples undergoing capped annealing or high dose ion implantation. This enhancement is attributed to stress fields in the former case, defects and surface dissociation in the latter. There might exist a "critical Cr concentration" for Cr depletion. GaAs substrates with lower Cr content than this concentration do not exhibit Cr depletion regardless of whether they have undergone capless or capped annealing.

References for Chapter 6

6.1) J. B. Clegg, G. B. Scott, J. Hallais and A. Mircea-Roussel, J. Appl.Phys. 52 (1981) 1110.

6.2) P. B. Klein, P. E. R. Nordquist and P. G. Siebenmann, J. Appl. Phys. 51 (1980) 4861.

6.3) H. Kanber, M. Feng and J. M. Whelan, Appl. Phys. Lett. 40 (1982) 960.

6.4) K. Watanabe, Y. Matsuoka, Y. Imamura and T. Ito, 1981 Gallium Arsenide and Related Compounds.

6.5) J. R. Arthur, J. phys. and Chem. of Solids, 28 (1967) 2257.

6.6) S. M. Sze, 1969 Physics of Semiconductor Devices (New York: Wiley Interscience) P.31.

6.7) W. E. Lum and H. H. Wieder, Appl. Phys. Lett. 31 (1977)213.

6.8) K. Watanabe, Private communication.

6.9) J. H. Crawford and L. M. Slifkin, Point Defects in Solods, 2 (1975) p.224.

6.10) F. M. Smith and R. C. Miller, Phys. Rev. 104 (1956) 1242.

6.11) J. Kasahara and N. Watanabe, Jpn. J. Appl. Phys. 19 (1980) L151.

6.12) A. M. Huber, G. Morillot, N. T. Linh, P. N. Favennec, B. Deveaud and B. Toulouse, Appl. Phys. Lett. 34 (1979) 858.

6.13) T.J.Magee, R.D.Ormond, C.A.Evans, Jr, R.J.Blattner, R.M.Malbon, D.S.Day and R.Sankaran, Appl. Phys. Lett. 38 (1981) 559.

6.14) R.Zucca, Inst. Phys. Conf. Ser. No.33b, 1977: Chapter 4, p.228.

6.15) F. Simondet, C.Venger, G.M.Martin and J.Chaumont, Inst. Phys. Conf. Ser. No45: Chapter 2, 1980, p.100.

6.16) T.J.Magee, H.Kawayoshi, R.D.Ormond, L.A.Christel, J.F.Gibbons, C.G.Hopkins, C.A.Evans Jr, and D.S.Day, Appl. Phys. Lett.39 (1981) 906.

6.17) T.Udagawa, M.Higashiura and T.Nakanishi, Semi-Insulating Materials, Nottingh 1980 Ed. G.J.Rees, Shiva, Kent, (1980) p.108.

6.18) S.Nojima, private communication.

6.19) P.K.Vasudeu, R.G.Wilson and C.A.Evans, Jr, Appl. Phys. Lett. 36 (1980) 837.

6.20) G.G.Hopkins et al, Appl. Phys. Lett. 36 (1980) 989.

6.21) Y.Sato, Jpn. J. Appl. Phys. 12 (1973) 242.

6.22) R.G.Wilson, P.K. Vasudeu, D.M.Jamba, C.A.Evans, Jr. and V.R.Deline, Appl. Phys. Lett. 36 (1980) 215.

6.23) R.C.Miller and F.M.Smith, Phys. Rev. 107 (1957) 65.

6.24) B.Deveaud and P.N.Favennec, Solid State Communication, 24 (1977) 473.

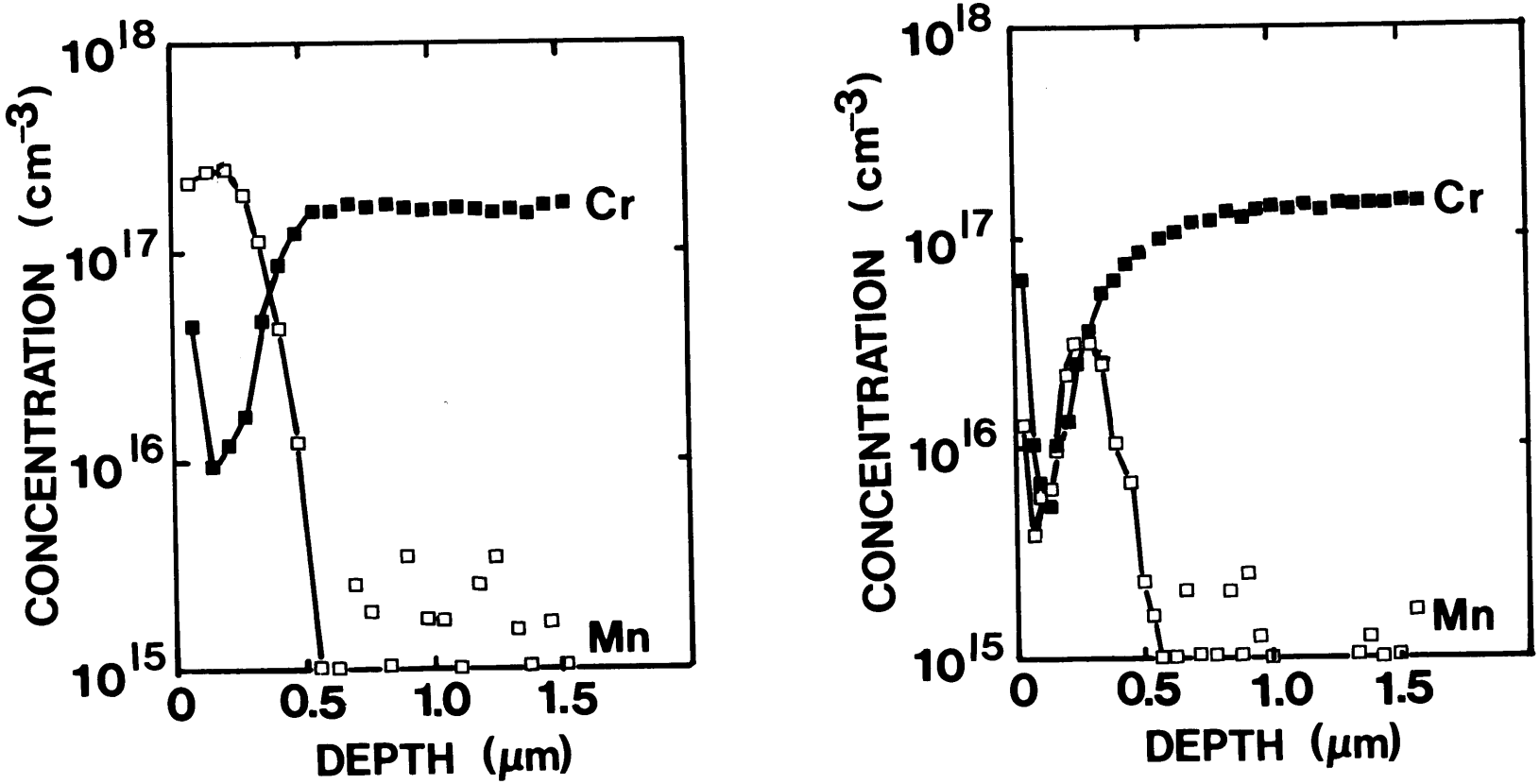

Fig.6.1 Cr and Mn redistribution of GaAs substrates annealed in two different furnaces at 800 C for 1 hr in H2 without encapsulation.

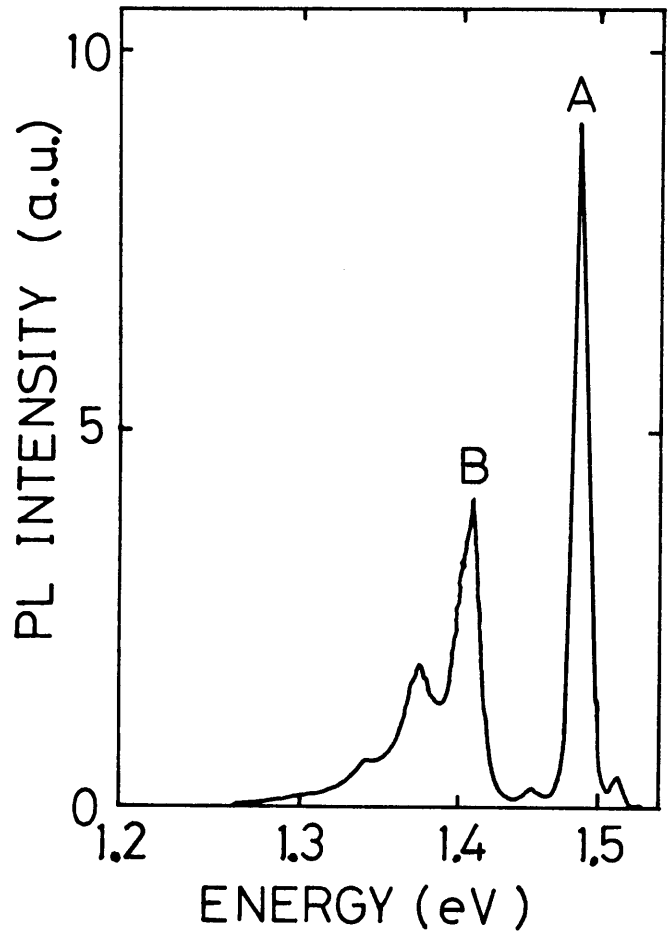

Fig.6.2 GaAs photoluminescence spectra at 4.2 K. Sample is the same as Fig.6.1 (a).

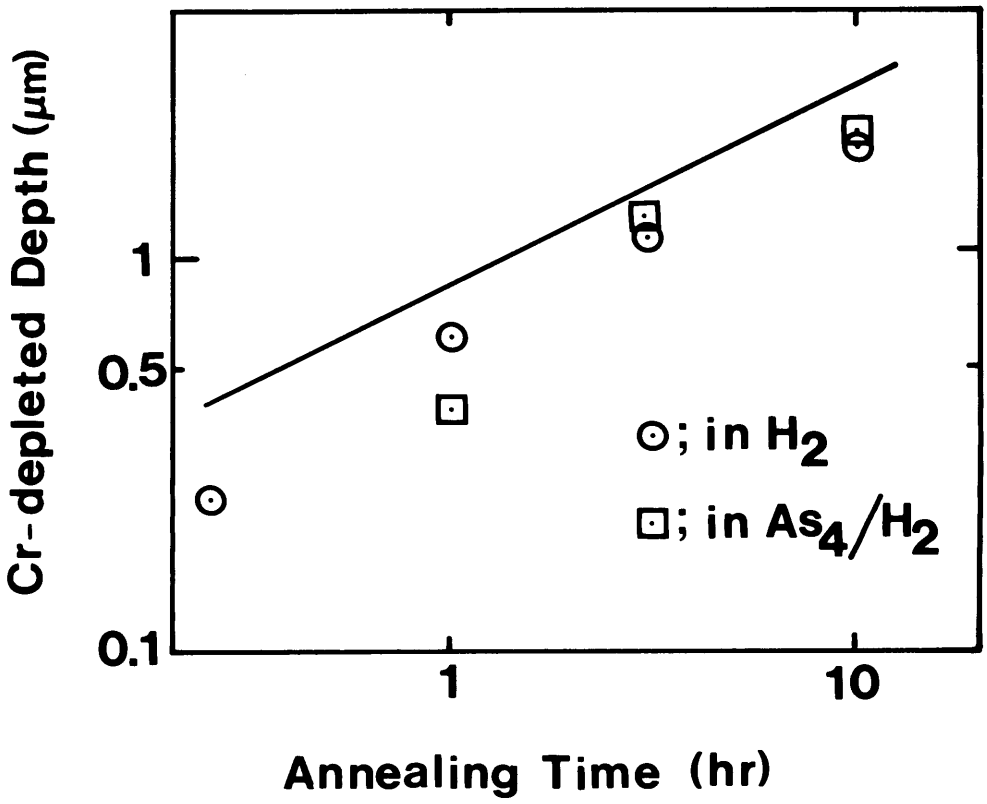

Fig.6.3 Cr depleted depth as a function of annealing time. Samples are annealed at 800 C in H2 (circles) and in As4/H2 (squares) without encapsulation. Solid line indicates the estimated value from the reported Cr diffusion coefficient in GaAs.

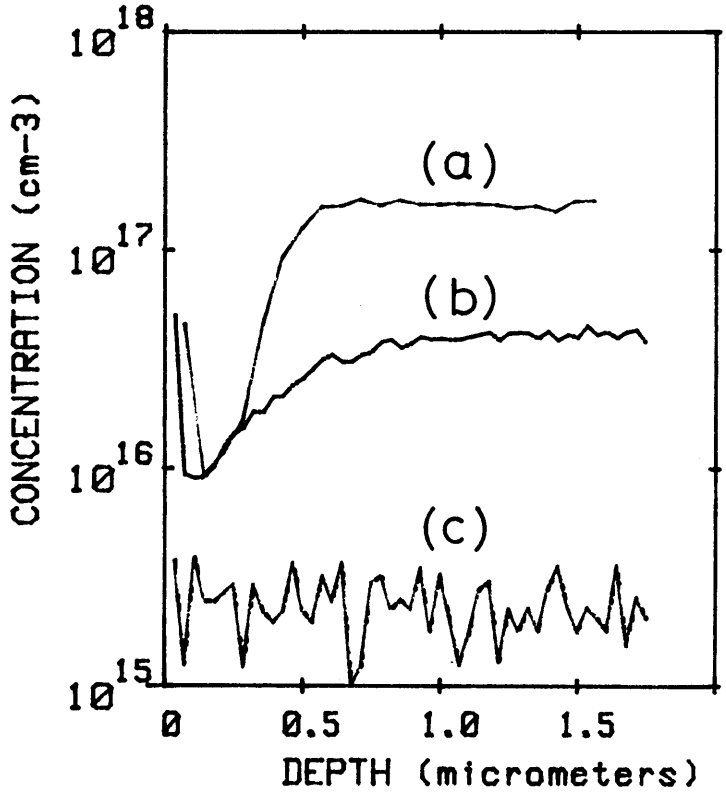

Fig.6.4 Cr depth profiles as a function of Cr concentration in GaAs. (a) and (b) indicate HB Cr-doped substrates and (c) LEC. Annealing was perfomed at 800 C for 1 hr without encapsulation. Mn profiles which are not shown here are located just in the Cr-depleted region.

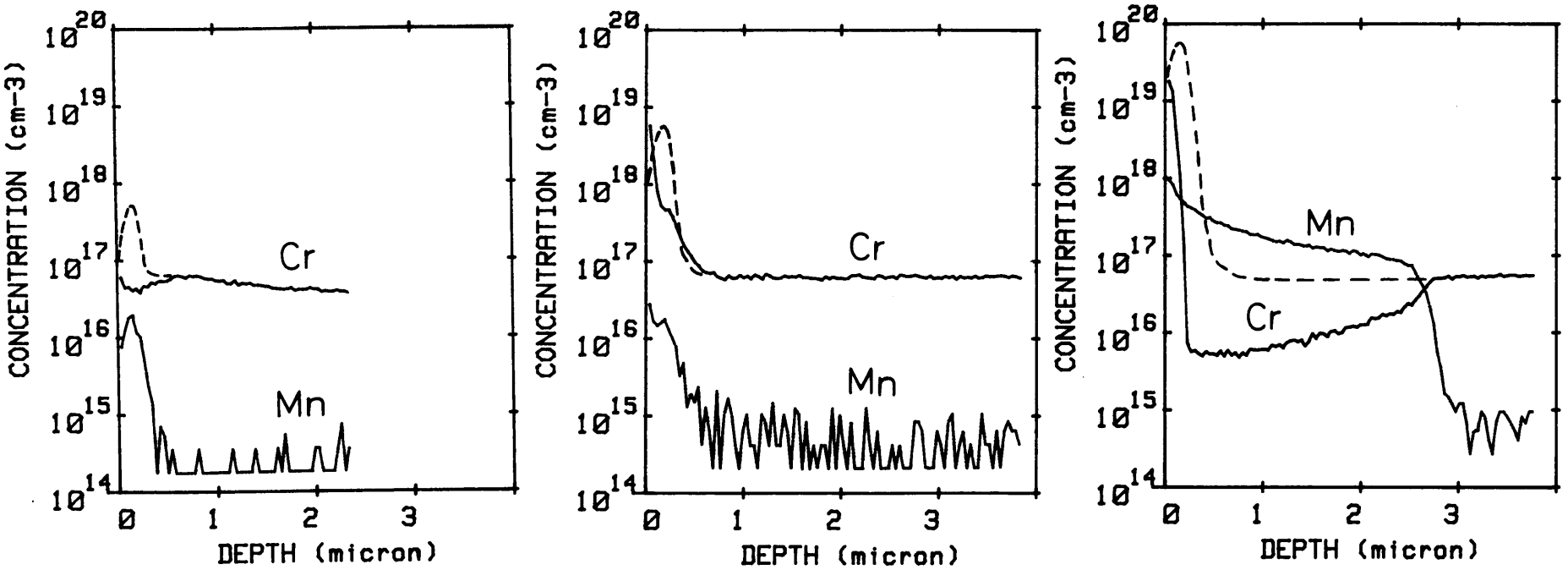

Fig.6.5 Cr and Mn redistribution in GaAs substrates annealed at 800 C for 1 hr in H2 without encapsulation after ion-implanted at 300 keV with 10^{13}, 10^{14} and 10^{15} Cr cm^{-2} doses; (a), (b) and (c), respectively. The dotted line indicates Cr in-depth profile of as-implanted substrates.

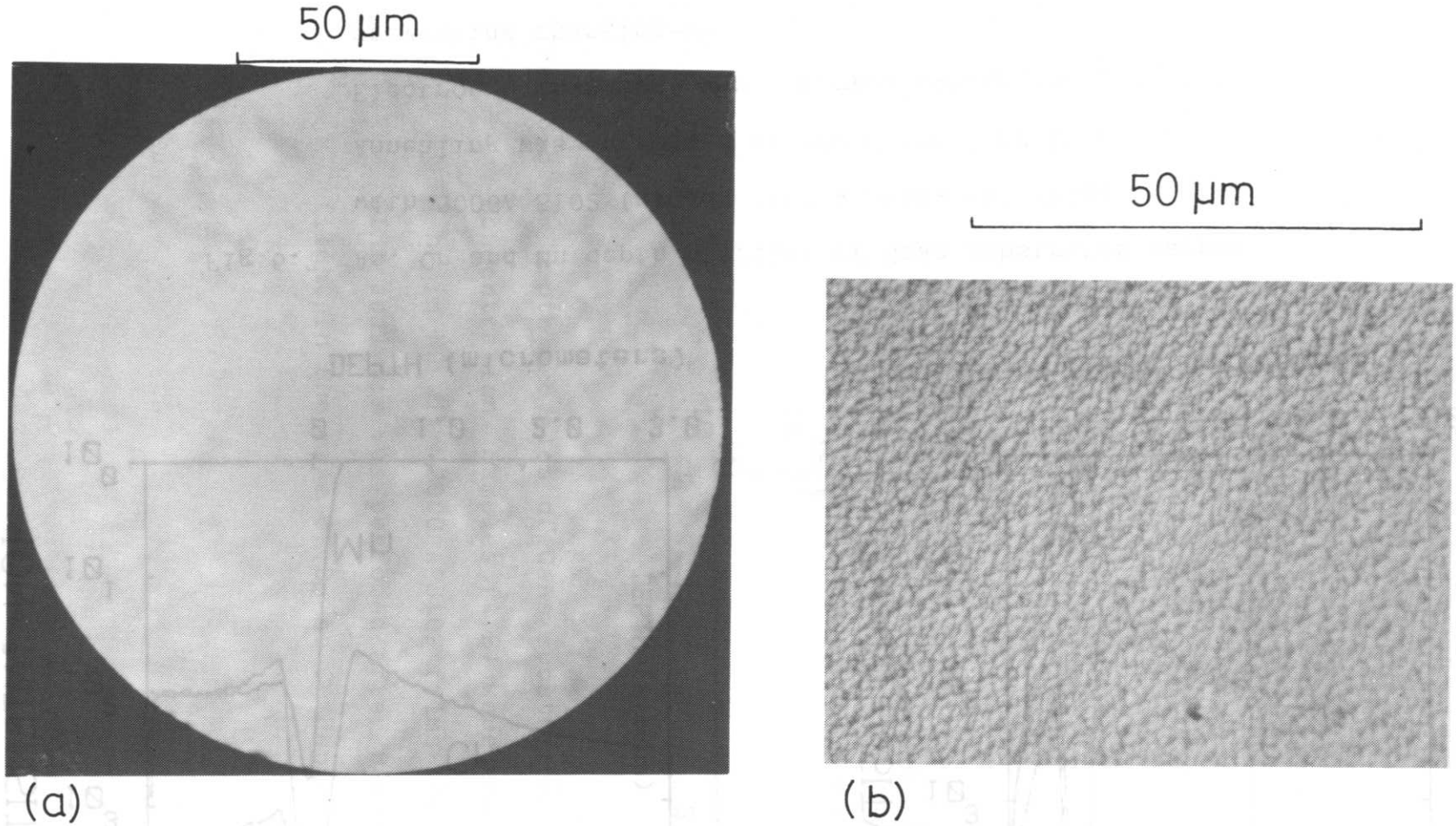

Fig.6.6 $^{69}Ga^{+}$ secondary ion image by SIMS (a) and photograph by Nomarski differential interference microscope (b). Sample is the same as Fig.6.5 (c). In this case, SIMS spacial resolution was about 1 μm which was verified using 1 μm line and space patterns.

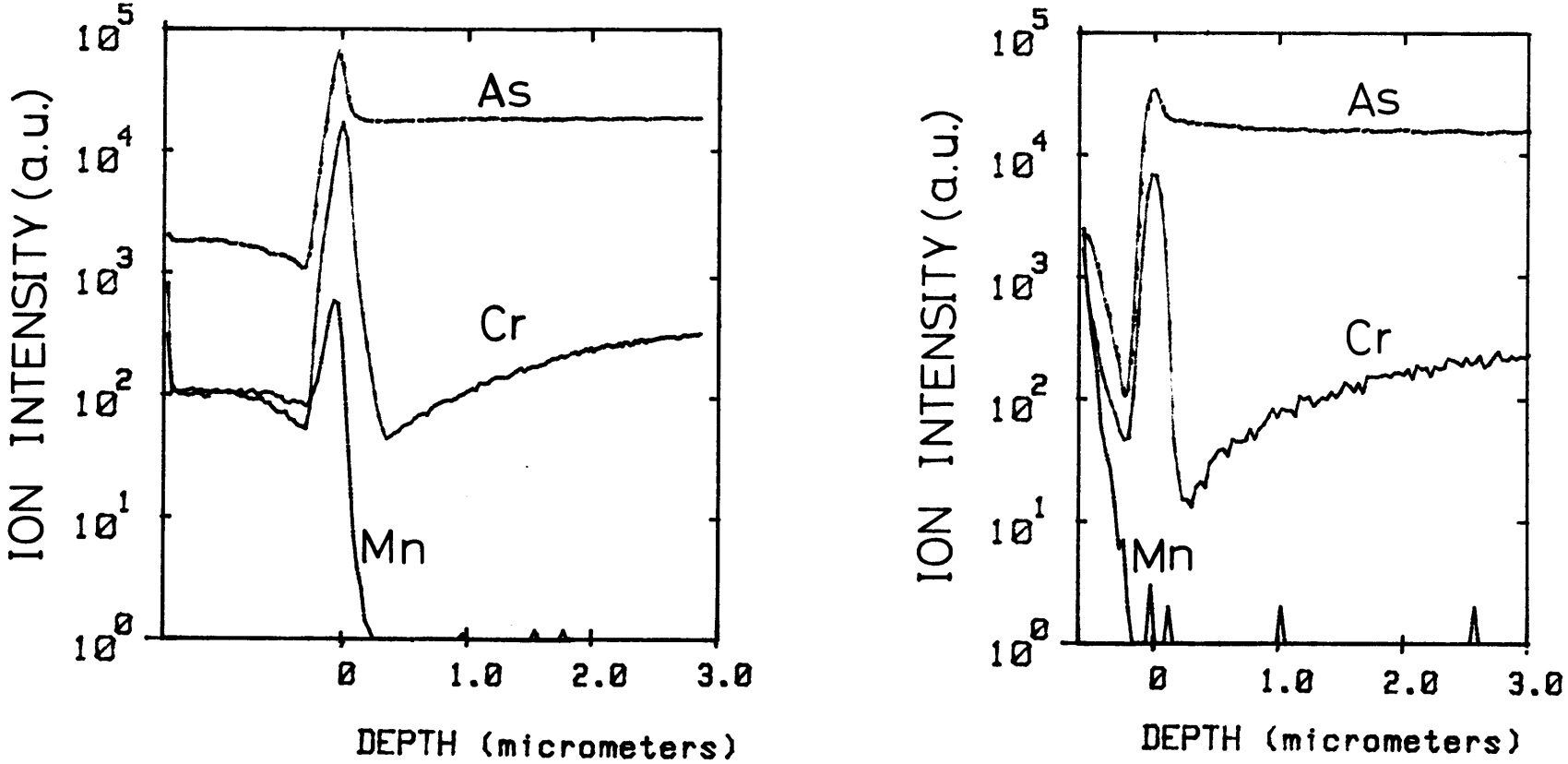

Fig.6.7 As, Cr and Mn depth profiles of GaAs substrates capped with 3000A SiO2 (a) and 1600 A Si3N4 (b) films. Annealing was performed at 800 C for 1 hr in H2. Electron bombardment was employed during analysis for preventing charging-up.

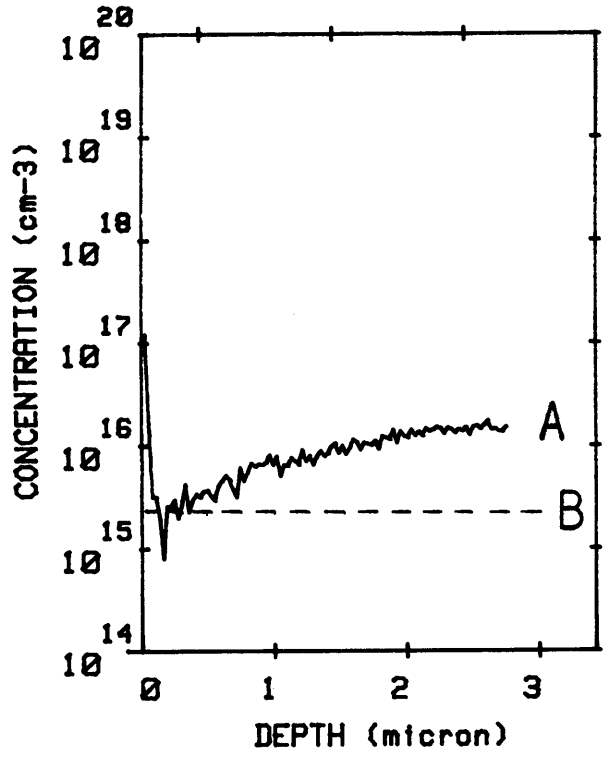

Fig.6.8 Cr depth profiles of GaAs substrates with different Cr concentration. Samples (A,B) were annealed at 800 C for 1 hr in H2 with 3000 A SiO2 films for encapsulation. SIMS analysis was perfomed after removal of capping films. In the case of B, no Cr depletion was observed.

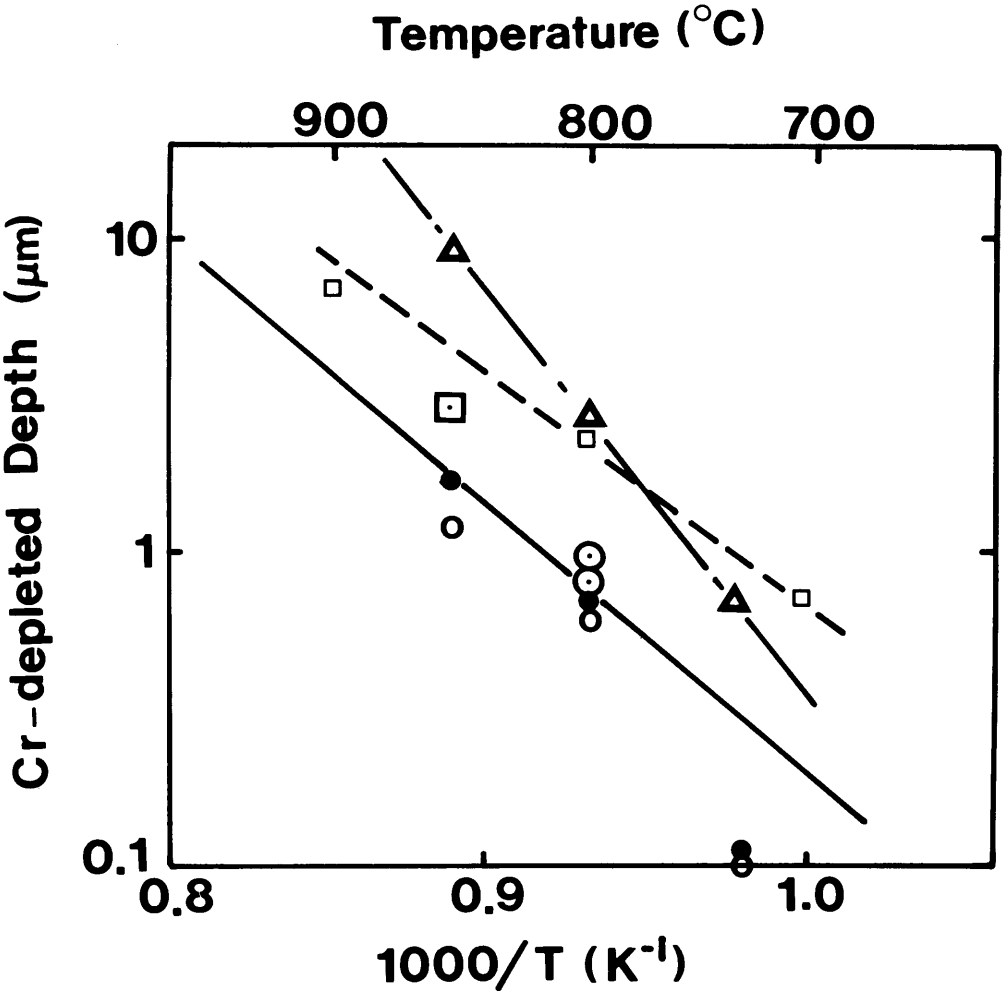

Fig.6.9 Cr-depleted depth as a function of 1/T. T stands for annealing temperature. Solid line indicates the estimated value from Cr diffusion coefficient in GaAs.

1) Capless annealing; open circles-HB crystal (1.4×10^{17} cm^{-3}), solid circles-LEC crystal (4×10^{16} cm^{-3}), circles with dot-after Vasudue et al (6.19), triangles-ion implanted with 10^{15} cm^{-2} dose.

2) Capped annealing; squares-HB crystal, squares with dot-after Hopkins (6.20).

Chapter 7 Photoemission Spectroscopy of a Clean and Oxidized Nb-Al Alloy using Synchrotron Radiation*

7.1 Introduction

Considerably attention has been given to the A-15 superconducting compounds, especiially Nb3X (X=Al, Ge, Si, etc.), because of thier high transition temperature (Tc). Although there have been many attempts aimed at realizing high Tc materials, only a few studies have been reported in which the oxidatiion of materials relevant to practical devices (such as Josephson junction(JJ) logic elements) is discussed using photoemission spectroscopy. Since JJ devices depend on the electronic properties of surfaces and interfaces for proper operation, it is of great practical importance to investigate the oxidatiion properties of Nb3X compounds.

While Miller et al (7.1) reported the oxidation properties of Nb3Sn, no results have been reported to our knowledge of Nb3X (X=Al, Ge and Si) using soft X-ray photoemission spectroscopy. This might be due to the difficulty in producing atomically clean A-15 Nb compounds in situ in the UHV (ultra-high vacuum) chamber. In this chapter, we selected Nb3Al from the series of Nb3X compounds, because of the extensive existing knowledge of the oxidation properties of both pure Al(7.2,3) and Nb(7.4).

The purpose of this chapter is to investigate the oxidation properties (via core level shifts) of the Nb-Al alloy surfaces in comparison to Al, Nb and Nb3Sn. Furthermore, comparison of Auger electron spectroscopy data with XPS results has been made for

*Most of this part has been reported in ref. (A.10).

oxidized Nb-Al alloys in order to get a better understanding about the chemical shifts due to oxidation. Special attention was paid to the elucidation of Auger chemical shifts, in particular of Al LVV and O KLL,by means PES chemical shifts, aiming at the application of AES to chemical state analysis at a small region (for example, several μm) on the surface.

7.2 Experimental procedures

The experiments were performed on the 4° beam line(7.5) at the Stanford Synchrotron Radiation Laboratory using monochromatized synchrotron radiation emitted by the storage ring SPEAR. In this photoemission spectroscopy study, a photon energy of 110 eV was chosen in order to minimize their escape length of the electrons ejected from the Nb 4p and Al 2p core levels. In this way, only the uppermost atomic layers are studied. Electron energy analysis was accomplished using a double pass cylindrical mirror analyzer at a resolusion of 0.5 eV. The photon energy resolusion was 0.1 eV. All experiments were performed in a UHV ion pumped chamber with a base pressure of 7×10^{-11} Torr.

XPS with Al K_α and Mg K_α X-ray sources was also employed as well as AES to analyze the Nb-Al alloy surfaces which were exposed to the air.

An atomically clean Nb(110) surface was prepared from a Nb foil using the same technique (high temperature heat treatment) as Miller et al(7.6). The Nb substrate melted during the highest temperature heating and developed a creater (5 mm in diameter) at the center. After the heat treatment, a large single crystal grain was found(7.7) to have grown with a (110) orientation in the cratered region. This single crystal region of Nb was used as a substrate in this experiment. Al was then evaporated upon the clean Nb surface and annealed at 900 °C for 10 min. Although Nb3Sn is reported to be easily produced by an analogous method(7.8), their A-15 phase of Nb3Al was not verified to exist in this experiment. The clean Nb-Al alloy was then exposed to a range

from 10 to 300 Langmuir(L) of oxygen and annealed in order to study the oxidation properties of both the Al and Nb.

The Nb-Al alloys with different compositions for XPS and AES studies were made using high vacuum E-beam co-evaporation system with two quartz thickness monitors , where the base pressure was 2×10^{-9} Torr. In this case, A-15 structure was obviously confirmed using X-ray diffractmeter, and their Tc's were from 9 to 15 K. For these compounds, air-oxidized surfaces were analyzed because samples had to be transfered via air after the film growth.

7.3 Experimental results

(1) SR-PES of a clean and oxidized Nb-Al alloy

Figure 7.1 shows photoemission spectra of Al 2p for an Al metal and a clean and oxygen-exposed Nb-Al alloy. The curves are not normalized with respect to one another. The Al 2p core level is shifted by -0.9eV (i.e., towards lower binding energy) after depositing less than 1 monolayer of Al on the clean Nb. The Nb-Al alloy was produced by annealing a thick (>10A) Al layer on Nb at 900 C. Although the surface composition is difficult to determine due to the lack of available photoionization cross-section data at 110eV, a rough estimate (7.9) of the composition of both surfaces turned out to be Nb Al (x=4 to 5). Furthermore, the chemical shift of Al 2p in the submonolayer Al deposition on Nb is found to be the same as that in the alloy, indicating that both surfaces have the similar structure.

At 30L oxygen exposure, the "intermediate oxidation state"(7.3) of Al appeared in addition to its metallic peak. After both the 100 and 300 L exposure, an Al 2p peak characteristic (+2.6eV shift in binding energy) of the Al 2p level of Al2O3 was observed without the metallic Al 2p peak. However, in the case of the oxidation of pure Al metal, the "Al2O3" Al 2p peak, together with the metallic peak was reported (7.2). This result suggests that, in the uppermost two layers of Nb-Al alloy, most of Al atoms are located in the first layer. Therefore, at only a 100 L oxygen exposure, all Al atoms in the region sampled were completely oxidized.

By heating the 300 L exposed sample at 500 C for 10 min, we

obtained an Al 2p peak, chemically shifted by 2.8eV, which has previously been reported as a peak which appears after 200 C annealing of oxidized pure Al(7.3). After 900 C annealing, the peak height ratio of Al 2p to Nb 4p decreased drastically (by a factor of 3), and Al 2p position returned to the original position (metallic state).

Figure 7.2 shows photoemission spectra of the Nb 4p for Nb metal and a clean and oxygen-exposed Nb-Al alloy. The asymmetry of the Nb 4p peak in the case of the "pure metal" may be due to partial oxidation (although no O 2p emission was detected) or may be an inherent features of the Nb 4p lineshape. There is a -0.1eV chemical shift (towards lower binding energy) of the Nb 4p and a -0.9eV chemical shift of Al 2p (as previously discussed) after alloy formation in comparison with the pure metals. It should be noted, therefore, that more important than charge transfer between the Nb and Al, there are alloying effect similar to those seen (for example) by Freidman(7.10). Freidman et al reported the core-level shifts of Au 4f and Sn 3d in the Sn_xAu_y system. With increasing the composition of Sn in that system, the chemical shift of Au 4f increased, while that of Sn 3d decreased. In the comparison of the Sn4Au alloy to the pure metals, they found that ΔE(Sn 3d) was -0.1eV and ΔE(Au 4f) was -1.1eV, which is analogous to our results in Nb4Al.

Our results show that the oxidation properties of Nb in the Nb-Al alloy are quite different from that of Nb metal, as shown in Fig. 7.3. We find that the oxidation of Nb proceeds much slower in the alloy. While the metallic Nb 4p peak disappeared

after only a 3 L oxygen exposure to the pure metal, it still remained even after 30 L exposure to the Nb-Al alloy. In both cases, heavy oxidation of the Nb results in drastically broadened Nb 4p emission. The inhibited Nb oxidation of the alloy can be explained in terms of the Al uppermost layer structure. The Nb 4p chemical shift after the 100 L exposure implies that oxygen atoms penetrate into the second layer and form "Nb-O-Al"-like bonding. Furthermore, the Nb2O5 compound (about 5eV chemical shift) is mainly formed after a 300 L oxygen exposure, indicating that when the oxidation barrier by the top Al layer is broken, the oxidation of Nb in the second layer proceeds very fast because of the large reactivity of Nb. The relative Al 2p/Nb 4p intensity ratio remained unchanged until 30 L oxygen exposure. The ratio increased by a factor of two at 100 L and increased further to an overall factor of four at 300 L. This result indicates that there might be surface segregation of Al (due, most likely, to the formation of thermal stable Al_2O_3).

It is also interesting that Nb 4p was reduced from the Nb_2O_5 state into NbO and metallic Nb, while Al 2p was completely oxidized by 500 C heating. The oxygen used to form Nb_2O_5 is thought to diffuse out to the surface and to oxidize the uppermost Al atoms. After 900 C heating, the Nb 4p returned predominantly to the original metallic state, which might be due to the evaporation of surface oxygen with Al in the form of volatile Al-O molecules and so on. The comparatively noisy 900 C Nb 4p spectra (with respect to the pure Nb spectra) is due to a decrease in statistics brought about by a significant drop in the

photon source intensity.

The composition change due to oxidation was investigated by making Fig. 7.4 from the oxidation features in Figs. 7.1 and 7.2, and XPS results obtained using Mg K_{α} X-ray. Since Al 2p peak by Mg K_{α} is not very intense compared to that by 110eV light, much more amount of Al was deposited on the clean Nb metal and heated at 900 C for alloying. Therefore, the surface composition (NbAl2) determined using X-ray photoionization cross-section was Al-rich , while that by SR-UPS was about Nb4Al, that is Nb-rich.

The escape depth for Nb-Al alloy when Mg K_{α} X-ray and 110eV light are used was calculated of Al 2p and Nb 4p on the basis of Penn's epuation (7.11) as shown in Fig. 7.5. Al 2p and Nb 4p by 110eV are very surface sensitive, while those by X-ray have the escape depth of 20 to 30 A.

When oxygen was exposed on the Nb4Al, the Al 2p/Nb 4p ratio increased and reached about 5 times as large value as the metallic alloy atate at the very surface layer. On the other hand, the NbAl2 showed a decrease in metallic Al 2p/Nb 4p ratio and an increase in oxide Al 2p/Nb 4p ratio. Since XPS spectra come from deeper region (more than 20 A), total Al 2p/Nb 4p ratio remained almost constant after oxygen exposure, even if only the very surface region became Al rich. Therefore, it can be said that surface segregation of Al by oxidation takes place only at the uppermost layer, while the composition in the 20 to 30 A depth region (we call "surface region") remains almost unchanged.

Figures 7.6 (a) and (b) show photoemission spectra of O 2p at 30 L and 300 L of oxygen exposure for the Nb-Al alloy in

comparison to Nb and Al metals. While the O 2p peak appeared on the Nb-Al alloy at -6.4eV of binding energy(Eb) up to 30 L exposure, the Al metal has the O 2p peak at -6.9eV and the Nb metal at -5.8eV. Therefore, the oxygen on the alloy is considered to have the intermediate state between Al-O and Nb-O bondings. However, when 300 L of oxygen was exposed to these surfaces, the O 2p positions of Nb and Al metals remained almost unchanged (exactly,O 2p on Al:from -6.9 to -7.1eV, and O 2p on Nb: from -5.8 to -5.7eV), while the O 2p peak of the alloy came to coincide with that of Nb metal. The small difference between these spectra at about -7eV might be attributed to the Al2O3 state in the alloy.

(2) Auger electron spectroscopy of oxidized Nb-Al alloy

Auger electron is widely used not only for surface composition analysis, but also for chemical state analysis like XPS. Auger chemical effects of many elements have been reported so far on metallic and oxidized states. In this section, AES has been applied for the chemical-state analysis of oxidized Nb-Al alloys with different composition.

Figures 7.7 (a) and (b) show Al LVV and Al KLL shapes of oxidized Al and NbAl3 alloy. Surface sensitive Al LVV peak which has about 2.5 A escape depth shows about 1.5eV chemical shift from Al natural oxide to NbAl natural oxide, which might be due to the charge transfer from Nb atoms to Al atoms, like Fig. 7.1. In this AES chamber, the base pressure was about 1×10^{-9} Torr which is not good vacuum for reactive metals such as Al and Nb. It is interesting that the metallic Al peak was observed after Ar sputtering in the case of Al, while the sputtered NbAl3 alloy surface showed partially oxidized state, which might be because Al atoms in the alloy are more activated by the charge transfer from Nb atoms.

When oxygen of 5×10^{11} L was exposed on the sputtered NbAl3 surface, the Al LVV peak showed the larger chemical shift than the natural oxide, suggesting that the surface was not completely oxidized.

On the other hand, Al KLL peak which has about 23 A escape depth also showed larger chemical shift from the oxide to the NbAl3 oxide than the Al LVV. This can be explained by the fact that the Al KLL Auger electrons come from deeper region

(remaining metallic) than the natural oxide. On the Ar sputtered surface, almost metallic peak was observed, that means only very surface layer was oxidized after Ar sputtering, and probed by surface sensitive Al LVV Auger electrons.

In this way, Auger chemical shift is found to be useful even for the chemical-state discussion. However we have to be very careful about it, because Auger transition is two electon process, and spectra are the derivative form, that is dN/dE.

Secondly, Nb MNN Auger peak which is also very surface sensitive was measured from oxidized Nb-Al alloys. As shown in Fig. 7.8, Nb MNN peaks have almost the same peak position dependent on Al content in Nb-Al alloys. Surface sensitive Nb MNN peak from sputtered NbAl3 surface showed the metallic state, while Al LVV peak was partly oxidized (see Fig.7.7), indicating that slightly oxidized NbAl3 surface consists of oxidized Al and metallic Nb. This result coincides with the SR-PES.

After oxygen exposure of 5×10^{11} L to the sputtered surfaces, two Auger peaks appeared. The higher kinetic energy peak stands for the metallic state and the lower one for the oxidized state. The ratio of the oxidized state to the metallic one has a tendency that Nb in Nb-Al alloy with more Al content is likely to be oxidized. Since Al is easier to be oxidized than Nb, Nb with more Al might be more likely to be oxidized than Nb with less Al.

O KLL peak also showed chemical shift as shown in Fig.7.9. In the derivative form (dN/dE), O KLL peak position shifted from about 507eV of Al metal to 513eV of Nb metal, dependent on the Al content in Nb-Al alloy. This tendency was also confirmed in the

form of electron number (N) which was numerically integrated from (a).

This chemical shift might be due to the difference of chemical bonding from Al-O to Nb-O. As shown in Fig.7.6, O 2p of Al-O has quite different binding energy from that of Nb-O. The tendency of O KLL shift can be explained qualitatively by means of this O 2p shift. However, since O KLL peak is from two electron transition process, we have to see the shift of O 1s peak.

Figure 7.10 is the summary of Al LVV, Nb MNN and O KLL peak positions as a function of Al content in Nb-Al alloys. While Nb MNN shows no shift, Al LVV and O KLL have large chemical shift, which might be attributable to the fact that Nb has so many electrons that it is unlikely affected by charge transfer. On the contrary, Al and O are easy to be shifted because the number of electrons are small. This is the reason why O which has only 8 electrons suffered from the large amount of chemical shift.

7.4 Discussion

In order to elucidate these chemical shifts in Auger peaks, photoelectron spectra of Al 2p, O 2p and O 1s were taken on the same sample surfaces.

Figure 7.11 shows the schematic diagram of Al LVV Auger transition process from Al oxide and Nb-Al oxide. In this case, Al LVV from oxide is considered to be Al(2p)O(2p)O(2p) interatomic transition. As shown in Fig. 7.1, Al 2p from NbAl-O has -0.9eV shift from Al-O. O 2p has also -1.4eV shift from Al-O to NbAl-O (Fig. 7.6). Therefore, the transition from O 2p to Al 2p creates 68.3eV with which the electron of O 2p level is ejected from Al-O surface, while the transition in NbAl-O creates 68.8eV.

Thus, the Auger electron from Al-O should have the kinetic energy E_K =68.3-Φ-7.1eV, where Φ is work function, while that from NbAl-O should have E_K =68.8-Φ-5.7eV. So, we can expect 1.9eV chemical shift between NbAl-O and Al-O. The experimental Al LVV shift (1.5eV; Fig. 7.7) can be said to be comparatively in good agreement with this predicted value, taking into account that Al LVV is from natural oxide, while Al 2p and O 2p are from 300 L oxygen exposed surface.

Figures 7.13 and 7.14 show O 2p (valence band) and O 1s spectra of natural oxides of Nb, NbAl alloys and Al measured using Al K_α (1486.6eV) X-ray. Fermi energy was determined by making C 1s binding energy equal to 284.6eV. Among these spectra, we have sharp O 2p and O 1s peaks on the Nb natural oxide, which enable us to determine the work function also by using

X-ray-excited O KLL Auger peak in the N(E) form. Since the O KLL peak was at 512.2eV, the work function comes to 5.9eV from the following equation,

$$\Phi = (Eb(O\ 1s) - Eb(O\ 2p)) - Eb(O\ 2p) - E_K(O\ KLL). \qquad (7.1)$$

In this way, the O 2p peak position of Al-O bonding was determined to be 8.3eV using this work function, and indicated as the dot-and-dashed line in Fig. 7.13. It should be noted that O 2p peak positions of Nb-O and Al-O shifted from from 30 L oxygen-exposed surfaces to natural oxides via 300 L oxygen-exposed surfaces as follows;

Nb-O:5.8eV→5.7eV→5.9eV

Al-O:6.9eV→7.1eV→8.3eV

These results suggest that electron transfer from Nb to O is completed at the very first stage of oxidation, while that from Al to O requires plenty of oxygen.

Another point to be noted is that O 1s on NbAl alloys shows Nb-O and Al-O bondings dependent on the Al content in alloys, while O 2p has only Nb-O bonding, which coincides with 300 L oxygen-exposed alloy surface (Fig. 7.6). This may be due to the fact that outershell electrons are very sensitive to the bonding properties compared to core level such as O 1s.

In this way, O KLL Auger peaks prove useful for chemical state analysis of NbAl alloy oxides.

7.5 Conclusion

Alloy formation and the oxidation properties of a Nb-rich Nb-Al alloy have been studied using the surface sensitive technique of soft X-ray photoemission spectroscopy. We find that the chemical shift and oxidation behavior of the alloy produced by annealing is very similar to the submonolayer Al-deposited Nb surface. We also find the Al overlayer acts to decrease the oxidation rate of the Nb by about two orders of magnitude as compared to pure Nb or Nb3Sn.

There are two stages in the oxidation process of the Nb-Al alloy; namely, (1) Al-O and Nb-O formation at several 10 L, and (2) Al2O3 and Nb2O5 formation at more than 100 L. These stages are distinguished clearly in terms of Al 2p, Nb 4p and O 2p chemical shifts.

Auger electron chemical shifts of Al LVV, Nb MNN and O KLL have been studied on Nb-Al alloys with different Al content. It is found that these chemical shifts are very useful to evaluate the oxidized states of alloys. Furthermore, the tendency that the order of the extent of chemical shifts is O KLL, Al LVV and Nb MNN might be due to the electron number of elements.

These chemical shifts of Auger electrons are explained by means of two electron transition from chemically shifted higher level to lower level, which are confirmed using photoemission spectroscopy.

References for Chapter 7

7.1) J. N. Miller, I. Lindau and W. E. Spicer, Phys. Lett. 88(1982) 97.

7.2) S. A. Flodstrom, R. Z. Bachrach, R. S. Bauer and S. B. M. Hagstrom, Phys. Rev. Lett. 37(1976) 1282.

7.3) A. Bianconi, R. Z. Bachrach, S. B. M. Hagstrom and S. A. Flodstrom, Phys. Rev. B19(1979) 2837.

7.4) J. N. Miller, I. Lindau and W. E. Spicer, Inst. Phys. Conf. Ser. No. 39(1978) 244.

7.5) F. C. Brown, R. Z. Bachrach and N. Lien, Nucl. Instrum. Methods 152(1978) 73.

7.6) J. N. Miller, I. Lindau, P. M. Stefan, D. L. Weissman, M. L. Shek and W. E. Spicer, J. Appl. Phys. 53(1982) 3267.

7.7) Laue back-diffraction, performed on the Nb foil after completion of the synchrotron radiation experiments, indicated a (110) single crystal had formed.

7.8) J. A. Strozier, D. L. Miller, O. F. Kammerer and M. Strongin, J. Appl. Phys. 47(1976) 1611.

7.9) The cross sections at 110 eV were estimated from the calculated cross section at 120 eV found in:S. M. Goldberg, C. S. Fadley and S. Kono, J.Electron Spectroscopy and Related Phenomena 21(1981) 285.

7.10) R. M. Freidman, J. Hudis, M. L. Perlman and R. E. Watson, Phys. Rev. B8(1973) 2433.

7.11) D. A. Penn, J. Electron Spectrosc. Relat. Phenom. 9 (1976) 29.

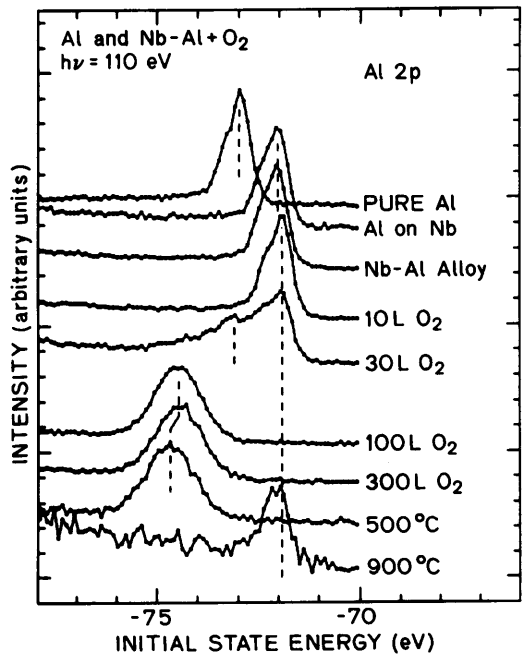

Fig. 7.1. Al 2*p* photoemission spectra from a thick Al evaporation (pure Al), a submonolayer evaporation of Al on Nb, and the Nb–Al alloy at various stages of oxidation. The spectra are *not* normalized with respect to each other.

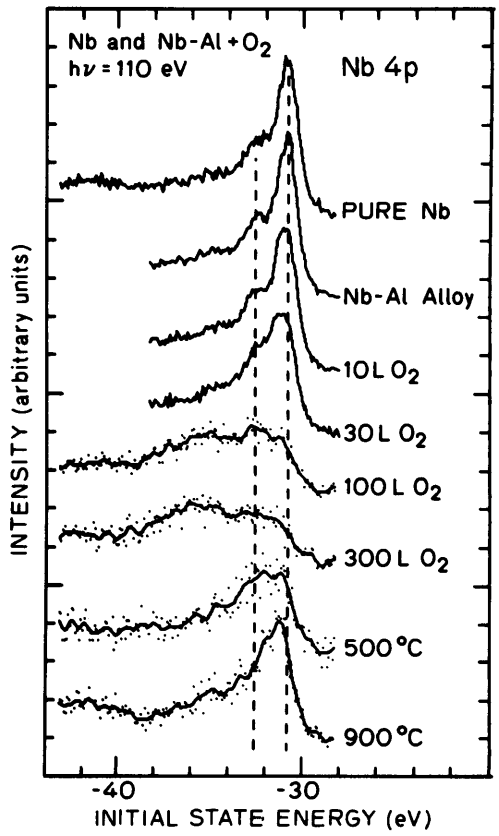

Fig. 7.2 Nb 4*p* photoemission spectra from clean Nb and the Nb–Al alloy at various stages of oxidation. The features at approximately 1.5 and 5 eV higher binding energy than the metallic peak position are attributed to NbO and Nb_2O_5 respectively. The spectra are *not* normalized with respect to each other. In the lower four curves, the solid line represents a 15 point smooth of the raw data (dots).

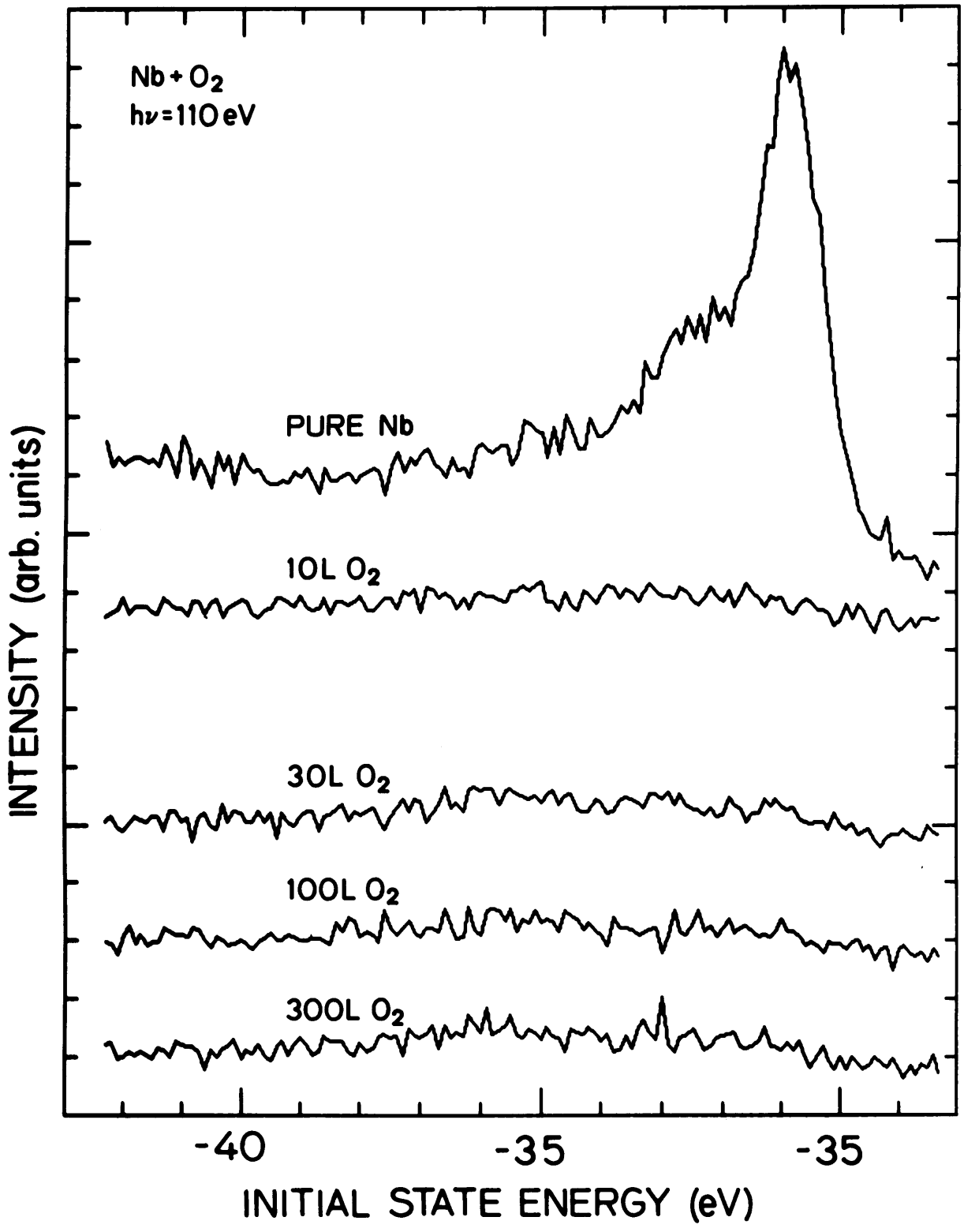

Fig. 7.3 Nb 4p photoemission spectra from clean Nb metal at various stages of oxidation.

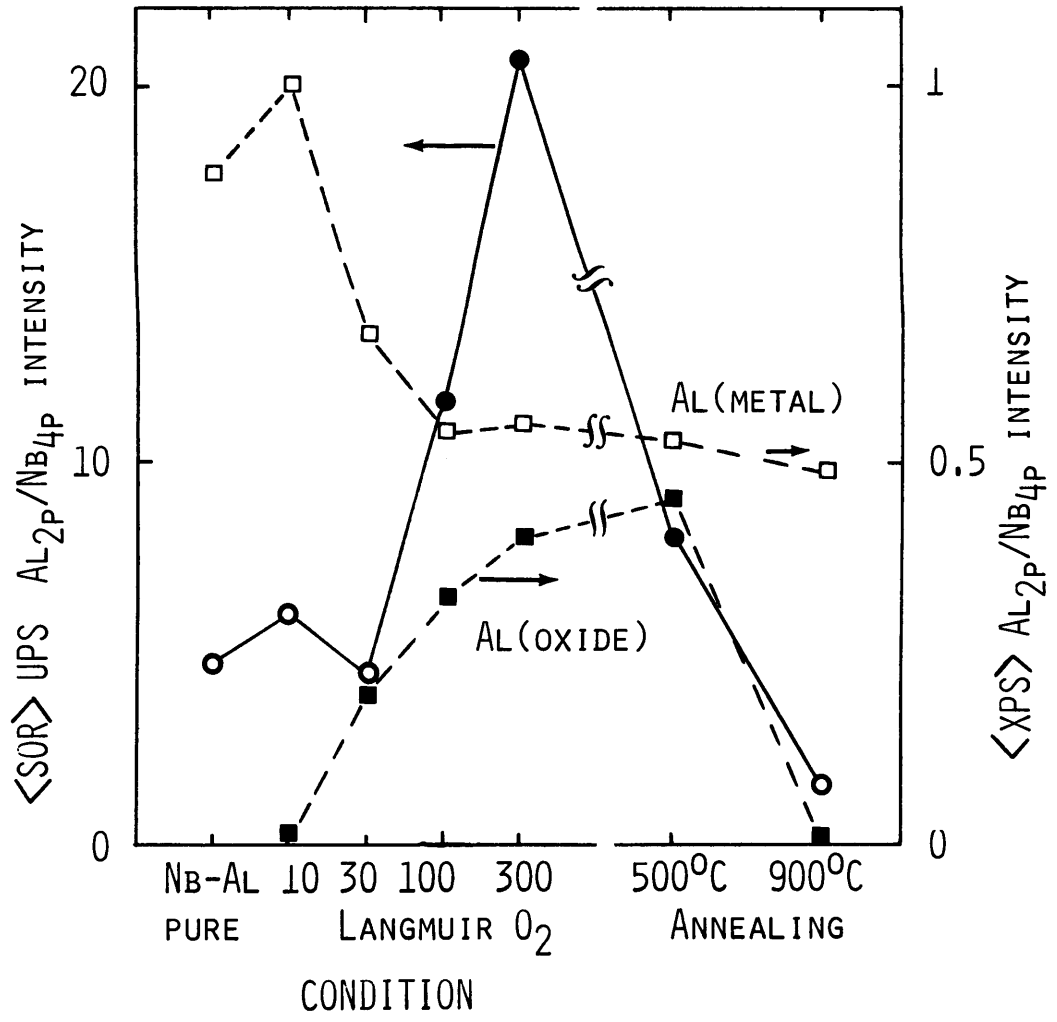

Fig. 7.4 Al 2p/Nb 4p intensity ratio by SR-UPS and XPS as a function of oxygen exposure and annealing temperature.

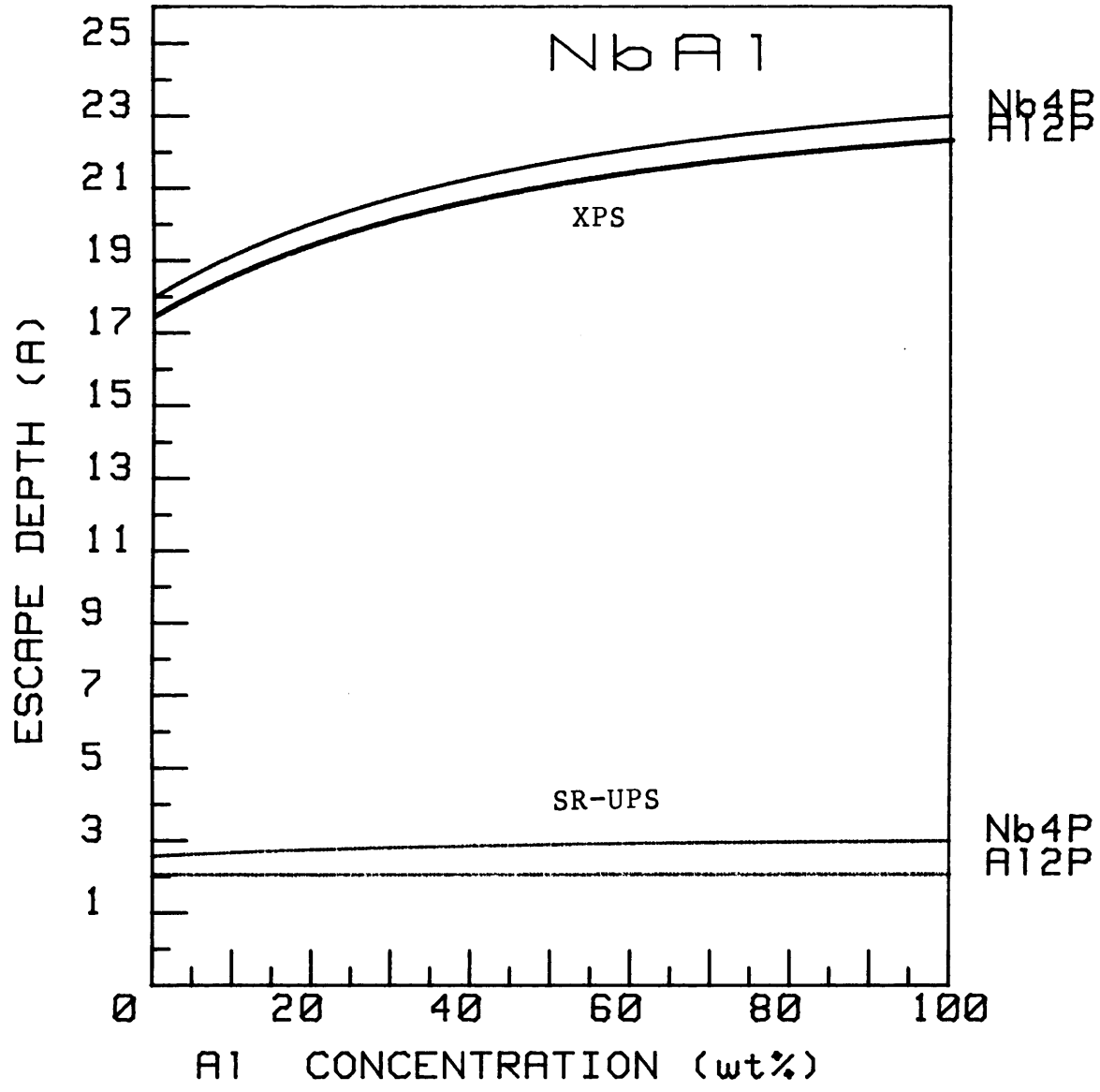

Fig. 7.5 Escape depths of Al 2p and Nb 4p as a function of Al concentration in Nb-Al alloy, measured by SR-UPS and XPS.

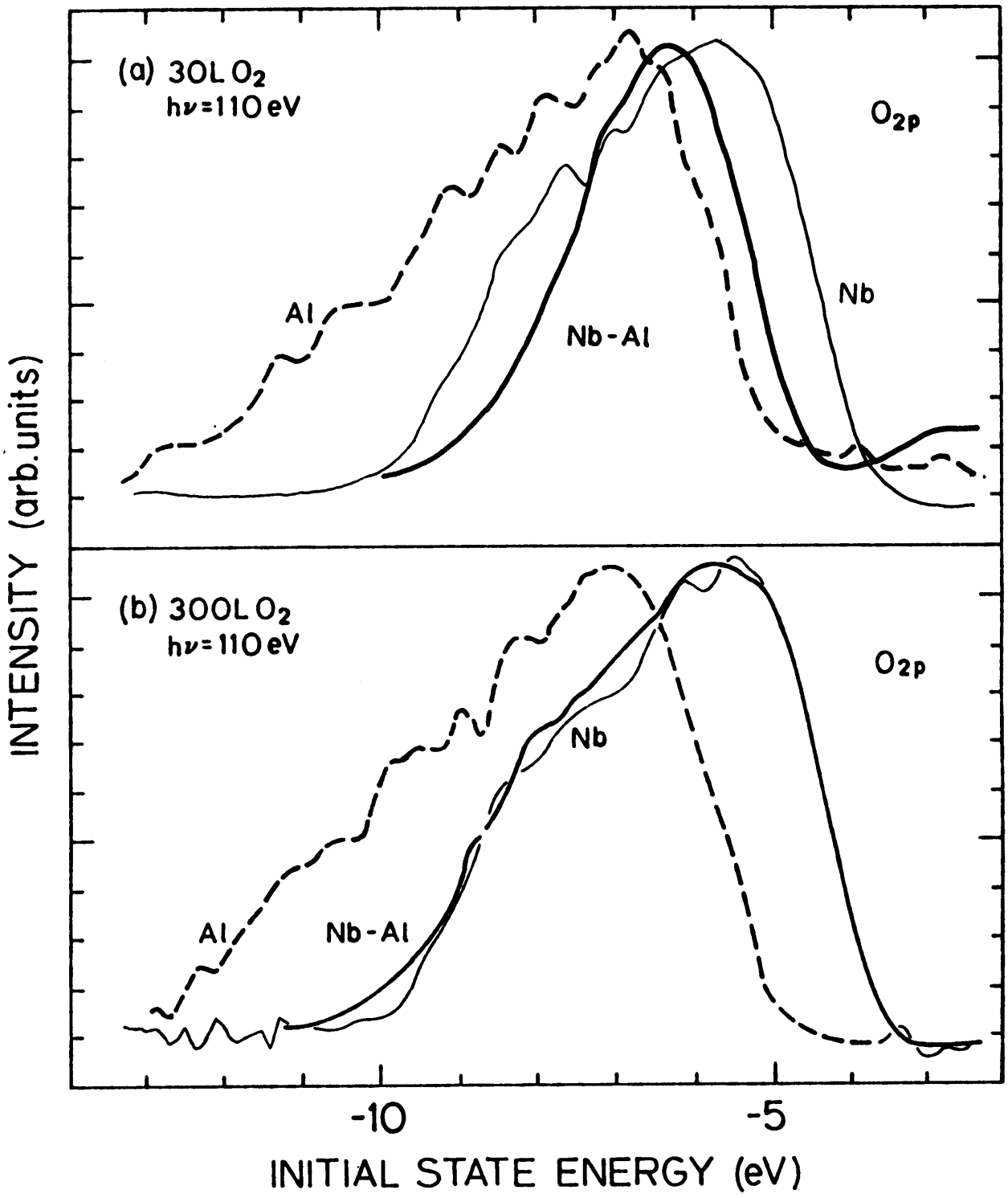

Fig. 7.6 O 2p photoemission spectra from Al, Nb, and the Nb-Al alloy at (a) 30 L, and (b) 300 L oxygen exposure.

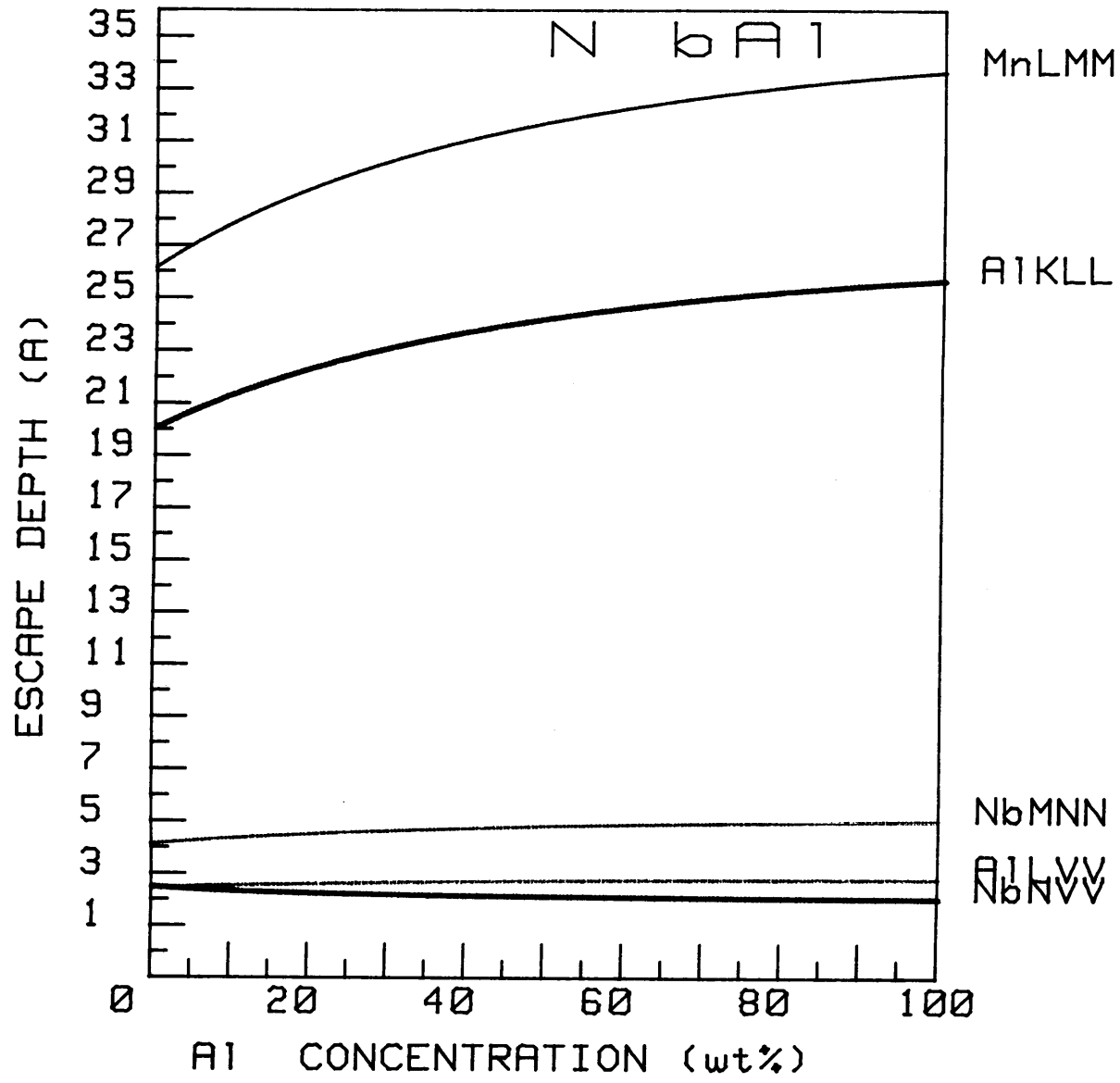

Fig. 7.7 Escape depths of Al and Nb Auger electrons as a function of Al content in Nb-Al alloys.

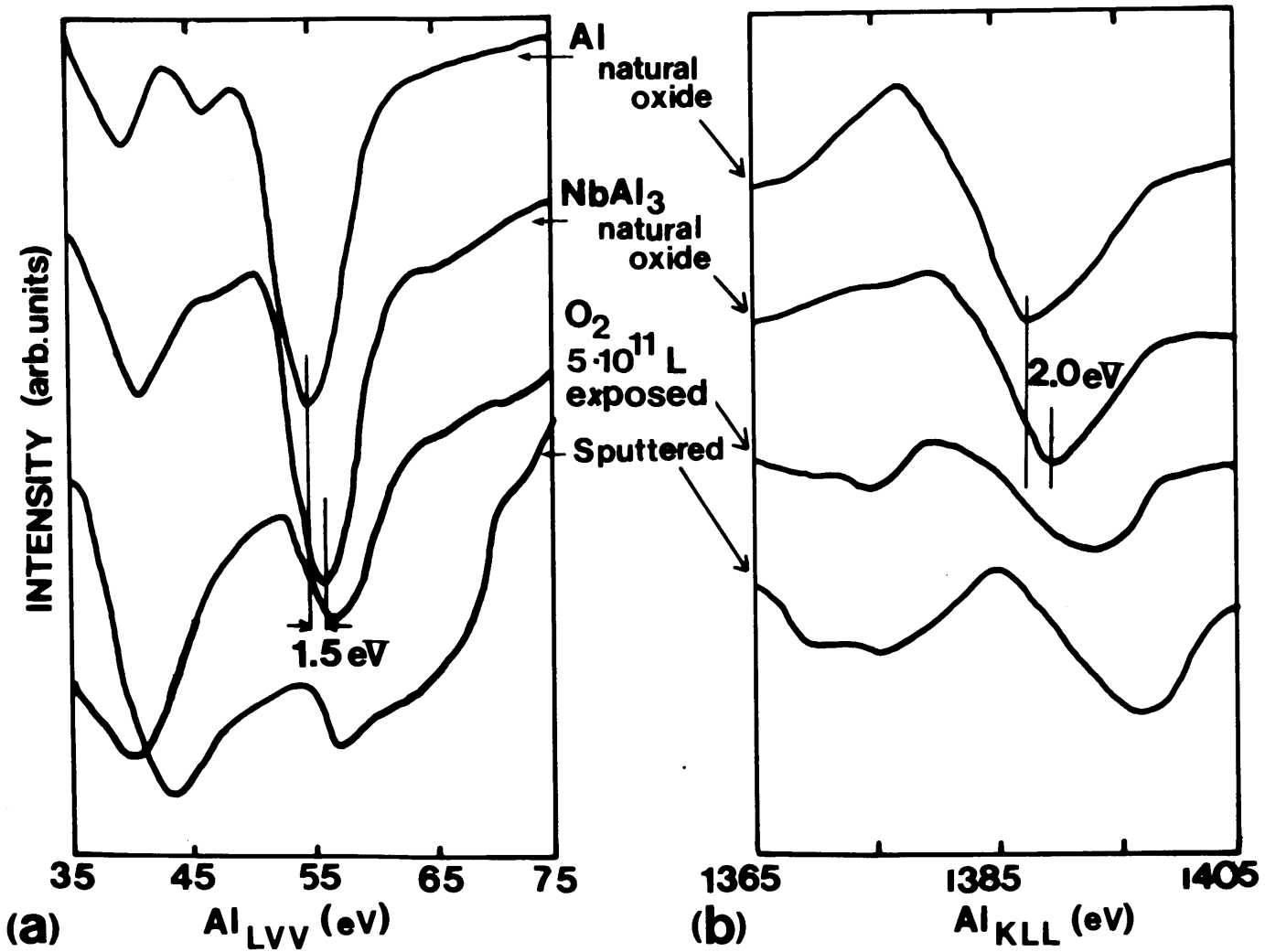

Fig. 7.8 Al LVV(a) and Al KLL(b) Auger peaks in dN/dE form from Al andNbAl3 oxides. Al LVV has about 2.5 A escape depth, while Al KLL has 23 A.

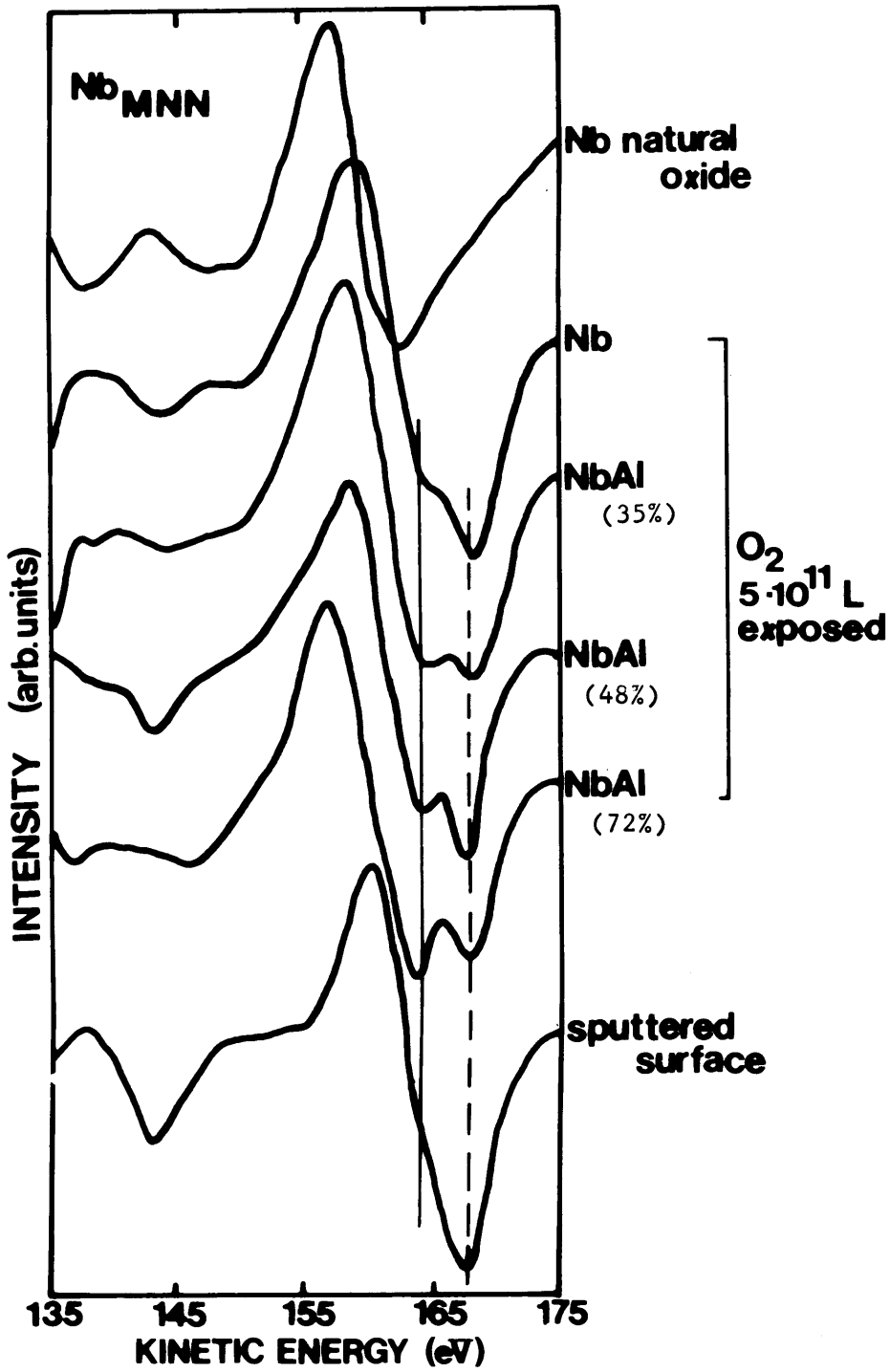

Fig. 7.9 Nb MNN Auger peaks in dN/dE form from oxides of Nb and Nb-Al alloys with different Al content. Dashed position corresponds to metallic state, while solid line position to oxide state.

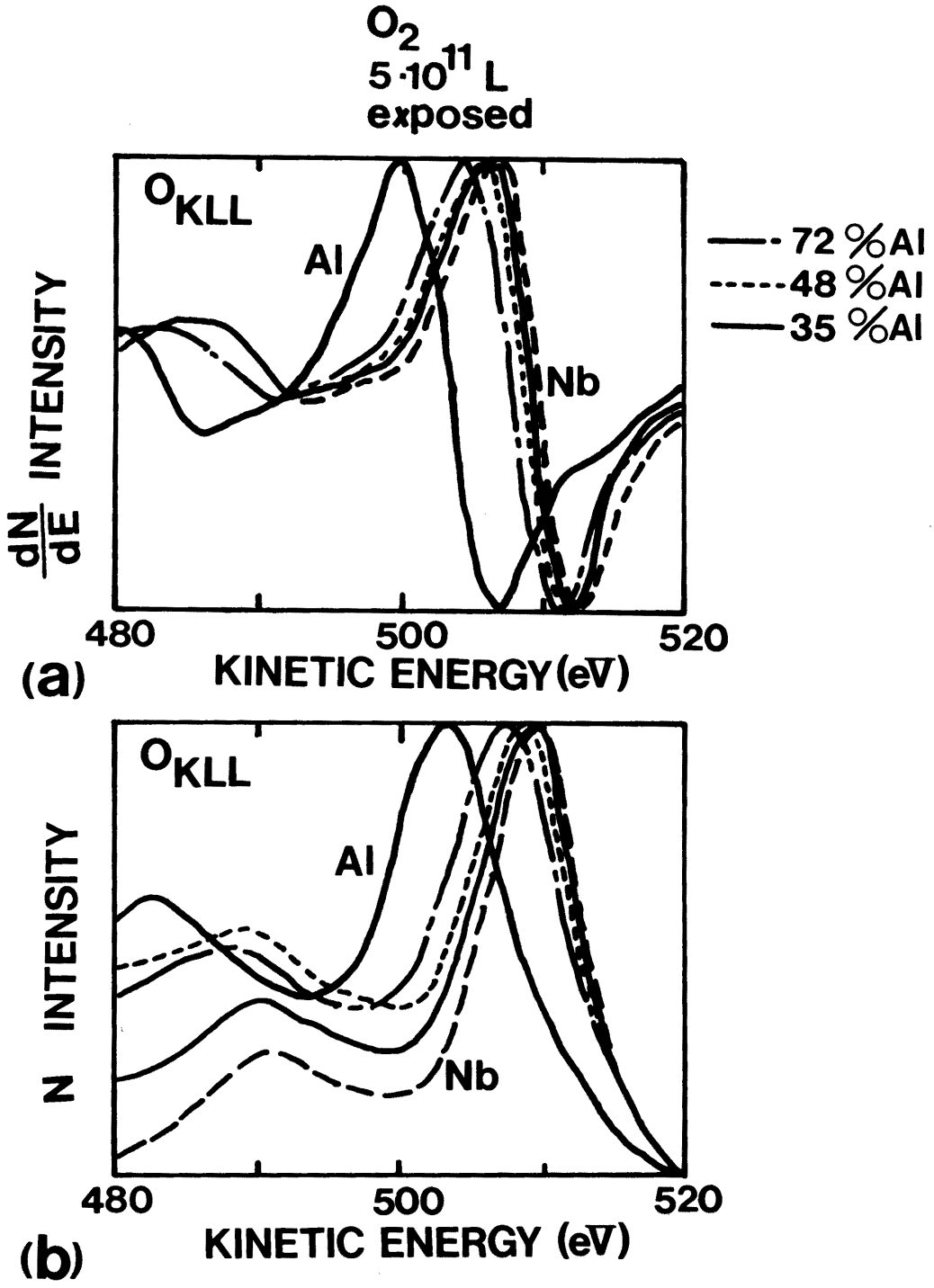

Fig.7.10 O KLL Auger peaks in dN/dE (a) and N (b) forms from oxides of Nb, Al and Nb-Al alloys with different Al content. O KLL peak moves towards higher kinetic energy with increasing Nb content in Nb-Al alloy.

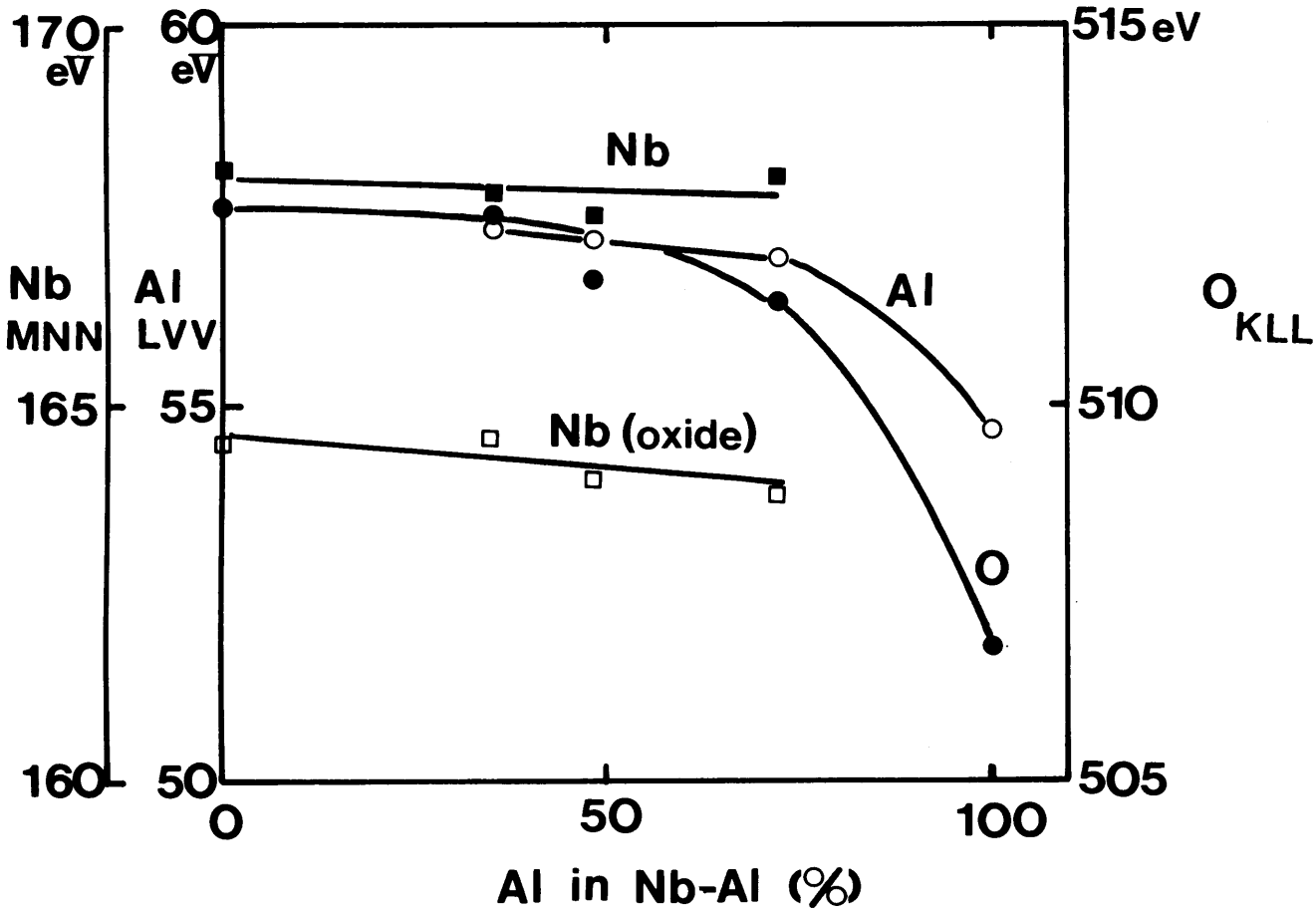

Fig.7.11 Auger peak position of Al KLL, Nb MNN and O KLL of Nb-Al alloy oxides as a function of Al content.

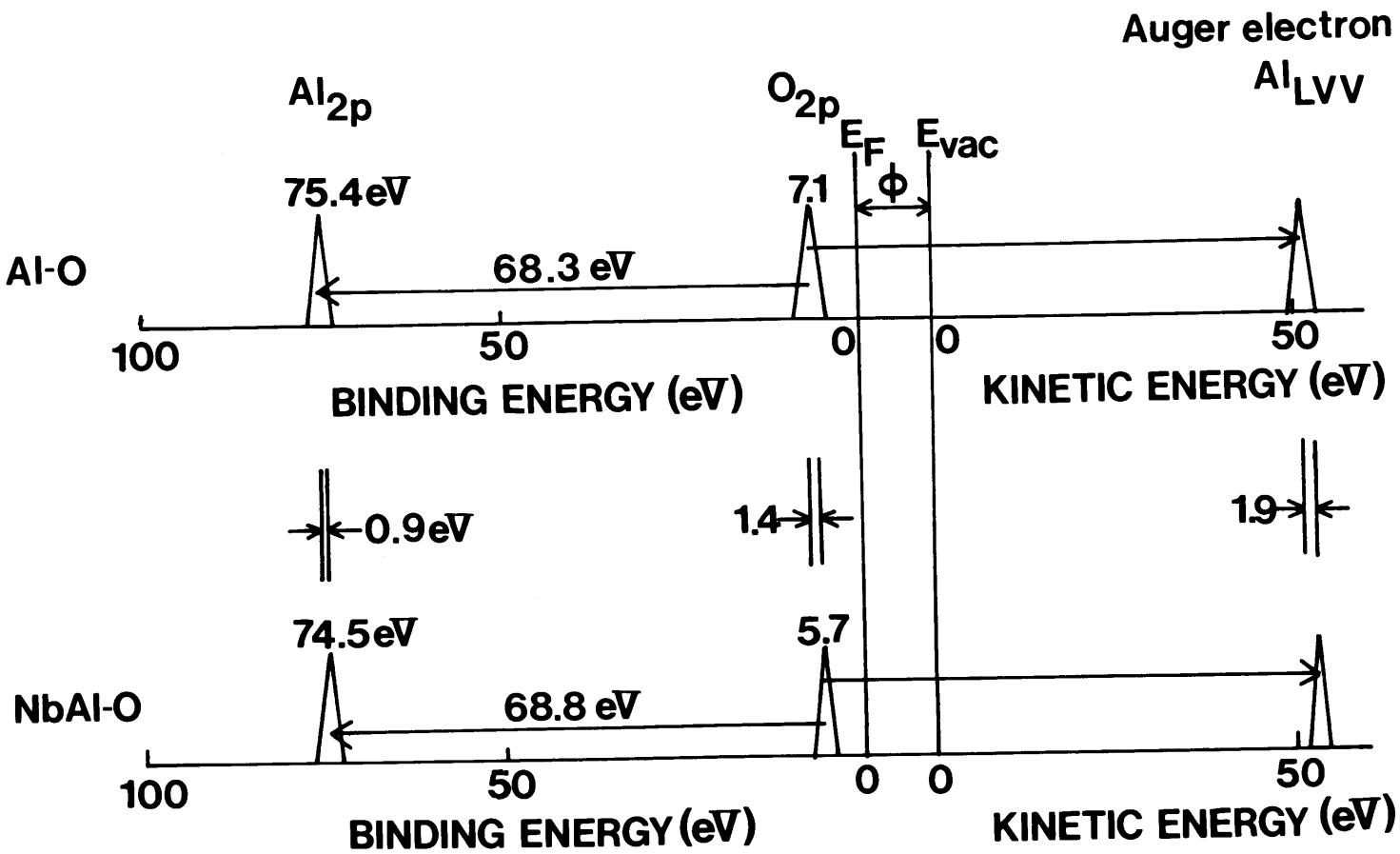

Fig. 7.12 Schematic diagram of Al LVV Auger transition process from the Al oxide and the Nb-Al oxide. Al LVV of oxide is considered to be Al(2p)O(2p)O(2p) interatomic transition.

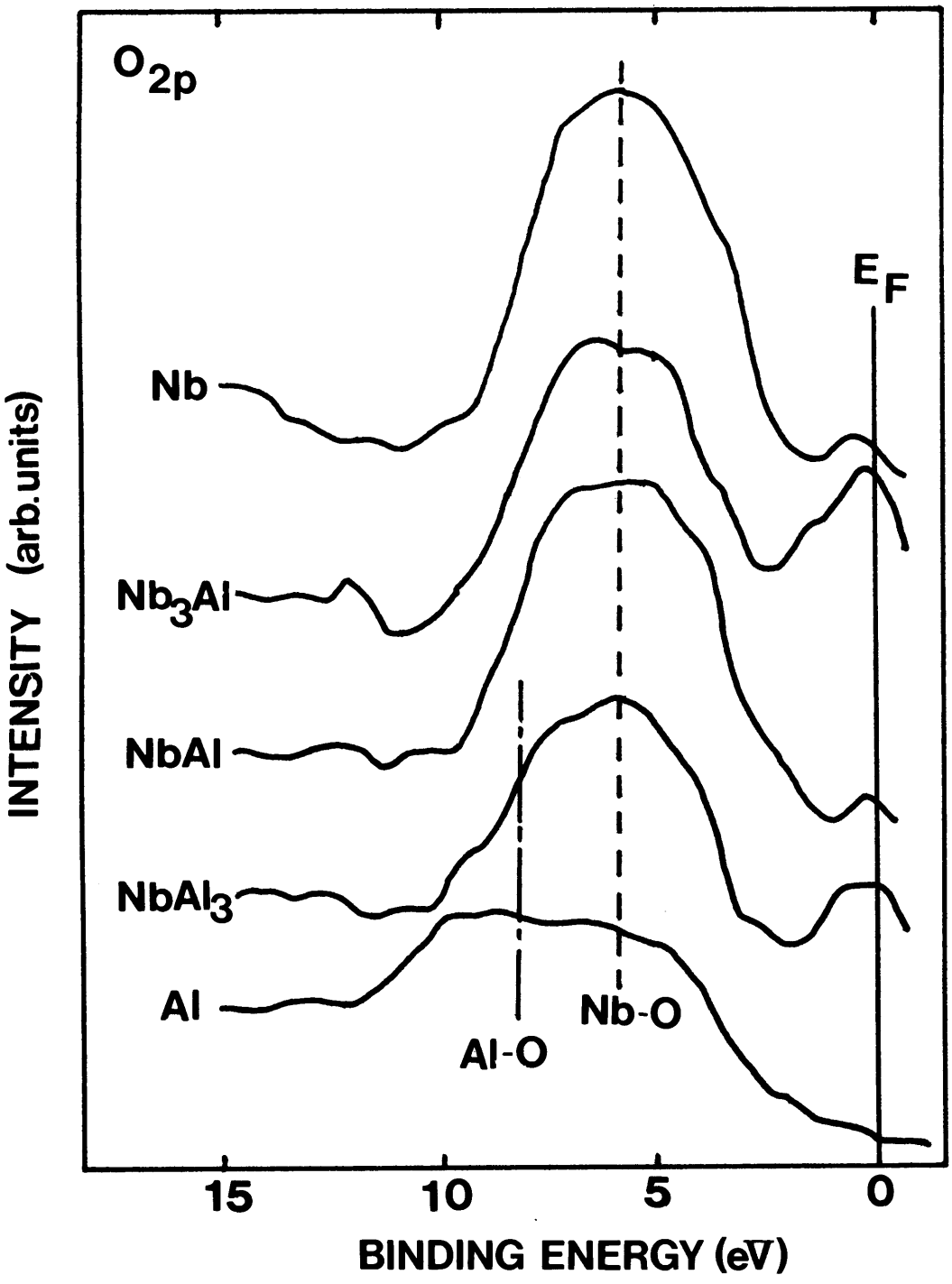

Fig. 7.13 O 2p photoemission spectra from Nb, Nb-Al and Al natural oxides, measured by XPS (Al K_α).

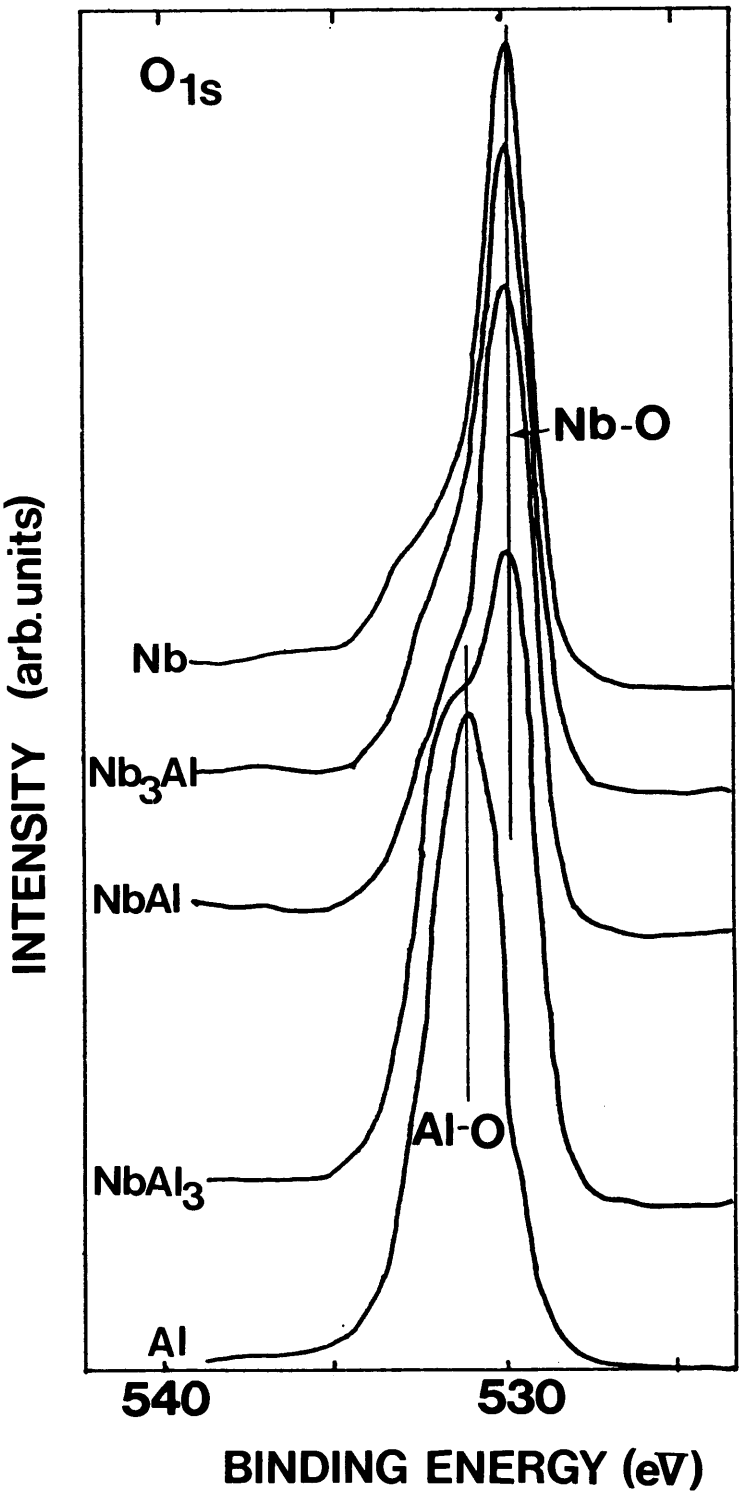

Fig. 7.14 O 1s photoemission spectra from Nb, Nb-Al and Al natural oxides, measured by XPS (Al K_α).

Chapter 8 Conclusions and Suggestions for Further Study

The surface analytical techniques, in particular SIMS, AES, and XPS have been applied to evaluation of Si, GaAs and superconducting materials.

SIMS has been employed to determine ultra-trace impurity distribution in semiconductors such as Si and GaAs for device fabrication designing with fine resolusion. Although calibration curves have been used for quantification of various impurity elements in Si and GaAs, the calculation technique based on the LTE plasma model was established and successfully applied to impurity concentration determination such as Si in GaAs, Na in Si or SiO2 etc.

High in-depth resolution SIMS technique was employed to evaluate the thermal conversion mechanism in semi-insulating GaAs substrates. The Chromium and Manganese redistribution was explained by using the simple diffusion theory and the enhanced diffusion by defects.

AES is a very surface sensitive and convenient technique to evaluate the contaminated surfaces.

For the evaluation of RSE Si surfaces, in situ AES system which consists of AES chamber, sample transfer chamber and RSE apparatus was designed to see the real contaminated surfaces. The relationship between the etching condition and C and F contamination content on the surfaces was investigated.

XPS is one of well-established tools for surface chemical state analysis. The chemical shift works provide us with the surface chemical bonding between substrate atoms and contaminants or oxygen.

This technique has been applied to the evaluation of RSE Si surfaces and oxidized Nb-Al alloys. On the RSE surfaces, CF,CF2 and CF3 bonds in addition to SiC bond were observed, which implied the RSE mechanism.

On the Nb-Al alloy, Al2p chemical shift due to alloying with Nb was observed which might be due to the charge transfer from Nb to Al. Surface oxidized structure was also investigated using Synchrotron Radiation which provides us with extremely surface sensitive information. Then, the initial oxidation process of Nb-Al alloy was elucidated. Furthermore , the chemically shifted Auger peaks of Al LVV and O KLL were explained by using two electron transitions between chemically shifted levels which were revealed with Photoemission Spectroscopy.

In addition to these surface analytical tools, mass spectrometry and emission spectroscopy have been used to see the plasma in RSE directly to find useful process monitoring signals and elucidate the etching mechanism. These techniques can be regarded as probes to investigate the surface reaction between gas and solid. For RSE of SiO2 and Si3N4 films useful moritoring signals were found. Furthermore, the dominant reactant in RSE of these films proved to be CFx ions, by which the fine pattern

delineation, namely directional etching can be realized.

TEM has been also utilized for surface analysis of gas-solid interaction-caused damages. The formation mechanism of the RSE-caused defects on Si substrates was elucidated for the first time. Furthermore, the relationship between defects and electrical characteristics was investigated.

For the further studies, (1) development of high sensitivity SIMS especially for carbon and oxygen , and (2) in situ plasma-processed surface analysis in conjunction with Synchrotron Radiation are required.

For the detail analysis of insulation and activation mechanism in GaAs devices, much higher sensitivity for C and O which act as deep acceptors and deep donors, respectively, are inevitable. In order to realize this low detection limit (less than 10^{15} cm^{-3}), clean working pressure as low as 10^{-10} Torr and Cs^{+} beam current as large as several tens μA should be obtained.

Synchrotron radiation is a promising light source to facilitate very surface sensitive PES and surface structural analysis such as SEXAFS (Surface Extended X-ray Absorption Fine Structure) and NPD (Normal Photoelectron Diffraction). On the other hand, plasma technology is widely employed for device fabrication. For future technologies such as GaAs IC with plasma -oxidized insulating film and Josephson junction devices with plasma-oxidized tunneling layer, the surface analysis of the plasma oxides would be definitely necessary. Therefore, the conjunction of SR and plasma process which is our next target

will be very powerful to provide us with useful information for new materials.

I believe these techniques would play a key role in developing new devices such as very high speed GaAs or Josephson Junction devices.

Acknowledgement

The author expresses his deepest gratitude to Professor Kazuo Fueki of University of Tokyo for his guidance, encouragement, and support during this work. The continuous encouragement of Prof. Takashi Mukaibo is sincerely appreciated. The author has also come to appreciate Professor W. E. Spicer and Professor I. Lindau of Stanford University for their many useful suggestions and their insight into physical problems.

He would like to express special thanks to his supervisors, Dr. M. Tokuyoshi, Dr. K. Aoyagi, Dr. R. Kanaoya, Mr. T. Hayashi, Dr. I. Ida, Mr. S. Hattori, Mr. M. Yamaguchi, Mr.S. Yoshii, and Mr. H. Araki for their guidance and encouragement, as well as useful discussions.

The author has been very fortunate to have collaborated with many members of the Material Evaluation Section of Technology Division, Mr. N. Yabumoto, Mr. Y. Homma, Dr. O. Michikami, Mr. I. Kawashima, Mr. T. Hayashi, Mr. H. Okamoto, Mr. M. Suzuki and Dr. Y. Ishii and he has enjoyed working with all of them. Thanks are extended to members in the Electrical Communication Laboratories, Mr. Y. Ozaki, Mr. K. Hirata, Mr. K. Watanabe, Dr. S. Miyazawa, and Dr. S. Matsuo, for their valuable discussions and support to this work.

Special thanks also go to Dr. B. B. Pate, Prof. Z. M. Lu (People Republic of China) and Mr. P. J. Jupiter for their friendship and discussions in the course of synchrotron radiation work at Stanford University.

VITA

Masaharu Oshima was born on March 17, 1949 in Izushi-gun Hyogo, and attended Kohdoh grade school, Izushi Junior High School, Toyooka High School. He received a Bachelor of Engineering degree in Industrial Chemistry from University of Tokyo in April 1972, and a Master of Engineering degree in Industrial Chemistry also from University of Tokyo in March 1974, both through Professor Takashi Mukaibo's and Professor Kazuo Fueki's guidances. Since April 1974, he has been engaged in the research and development of surface analytical technology. From October 1981 to September 1982, he had been studying synchrotron radiation photoemission spectroscopy under Professor W. E. Spicer's and Professor I. Lindau's directions at Stanford University.

List of Publications

(A.1) M. Oshima

"Use of Mass Spectra for End Point Detection in Etching SiO2 Films on Si"

Jpn. J. Appl. Phys. 20(7) (1981) 1255.

(A.2) M. Oshima

"Optical Spectroscopy in Reactive Sputter Etching and Its Application to Process Control"

Jpn. J. Appl. Phys. 20(4) (1981) 683.

(A.3) M. Oshima

"A Study of Dry Etching-Related Contamination on Si and SiO2"

Surf. Sci. 86 (1979) 858.

(A.4) N. Yabumoto, M. Oshima, Y. Ozaki and K. Hirata

"Investigation on the Damage Caused by Reactive Sputter Etching of Silicon Substrates"

Int. Phys. Conf. Ser. No 59:Chapter 8 (1981) 425.

(A.5) Y. Homma, M. Oshima and T. Hayashi

"An Investigation of the Properties of an Epitaxial Si Layer on a Substrate with a Buried SiO2 Layer Formed by Oxygen-Ion Implantation"

Jpn. J. Appl. Phys. 21(6) (1982) 890.

(A.6) M. Oshima

"Quantitative Analysis of Compound Semiconductors with an Ion Microanalyzer"

Mass Sectroscopy 25(1) (1977) 99.

(A.7) M. Oshima and Y. Homma
"Impurity Analysis in Si and GaAs with SIMS"
Mass Spectroscopy 30(3) (1982) 227.

(A.8) M. Oshima, I. Kawashima and S. Yoshii
"Quantitative Analysis of Semiconductor Materials with Secondary Ion Mass Spectrometer"
Jpn. J. Appl. Phys. 19(Suupl.19-1) (1980) 501.

(A.9) M. Oshima, K. Watanabe and S. Miyazawa
"Chromium and Manganese Redistribution in Semi-insulating GaAs"
J. Electrochem. Soc. 131(1) (1984) 130.

(A.10) M. Oshima, B. B. Pate, Z. M. Lu, P. J. Jupiter, I. Lindau and W. E. Spicer
"Photoemission Studies of a Clean and Oxidized Niobium-Aluminum Alloy Using Synchrotron Radiation"
Solid State Commun. 46(11) (1983) 815.

Other Publications Which are not used in this Thesis

(B.1) M. Asakawa, S. Matsuo and M. Oshima
"Plasma Reactive Sputter Etching System"
Electrical Communication Laboratories Technical Journal
27(9) (1978) 225.

(B.2) M. Oshima
"Monitoring of Dry Etching Process of SiO2 on Si by Using Mass Spectra"
Jpn. J. Appl. Phys. 17(3) (1978) 579.

(B.3) M. Oshima
"Determination of Plasma Gas Temperature during Reactive Sputter Etching"
Jpn. J. Appl. Phys. 17(6) (1978) 1157.

(B.4) M. Oshima, M. Seki and I. Kawashima
"Quantitative Analysis of Na in Si with SIMS"
Jpn. J. Appl. Phys. 17(9) (1978) 1697.

(B.5) Y. Ozaki, K. Hirata, N. Yabumoto and M. Oshima
"Contamination and Damage by Reactive Sputter Etching"
Proc. of the 2nd Symposium on Dry Processes, (1980) I-8.

(B.6) N. Yabumoto, M. Oshima, O. Michikami and S. Yoshii
"Surface Damage on Si Substrates Caused by Reactive Sputter Etching"
Jpn. J. Appl. Phys. 20(5) (1981) 893.

(B.7) N. Yabumoto, M. Oshima and S. Maeyama
"Reactive Sputter Etching of GaAs"
Proc. on the 4th Symposium on Dry Processes, (1982) 3-2.

(B.8) Z. M. Lu, W. G. Petro, P. H. Mahowald, M. Oshima, I. Lindau and W. E. Spicer
"The Effect of Surface Oxygen on the Intermixing and Schottky Barrier at GaAs(110)-Au Interfaces"
J. Vac. Sci. and Technol. B1(3) (1983) 598.

(B.9) B. B. Pate, M. Oshima, J. A. Silberman, G. Rossi, I. Lindau and W. E. Spicer
"Carbon 1s Studies of Diamond (111)-Surface Shifts, Hydrogenation, and Electron Escape Lengths"
J. Vac. Sci. and Technol. to be published.